Biological Application of Magnetic Nanoparticles in Targeted Therapeutics and Diagnostics

By

Aruna Sigdel

B.S., University of Maine, 2009

M.A., Brown University, 2011

Submitted in partial fulfillment of the requirements for the degree of DOCTOR OF PHILOSOPHY in CHEMSITRY awarded by the Chemistry Department at Brown University

PROVIDENCE, RHODE ISLAND

May 2014

This thesis by Aruna Sigdel is accepted in its present form by the Chemistry Department as satisfying the thesis requirement for the degree of Doctor of Philosophy.

Date_____ _____

Shouheng Sun, Ph.D., Advisor

Professor

Chemistry Department

Date_____ _____

Amit Basu, Ph.D.

Associate Professor

Chemistry Department

Date_____ _____

Robert Hurt, Ph.D.

Professor

Engineering

Approved by the Graduate Council

Date_____ _____

Peter Weber

Dean of the Graduate School

Acknowledgements

I have to thank several people without whom this journey wouldn't have been possible. My advisor, Professor Shouheng Sun, I am extremely thankful for his continuous support and understanding during this time. I feel very lucky to have the opportunity to work under his guidance throughout the years whose knowledge in the nanoscience is tremendous. I appreciate the valuable critique and advice from my committee members, Professor Amit Basu and Professor Robert Hurt, for guiding me on approaching research, to question and to defend. I am also thankful for the Chemistry Professors from whom I have learnt directly through class or teaching. I would also like to thank all the administrative staffs for their help in several areas.

In research area, I thank Dr. Don Ho for teaching me about all the basics in biomedical field, and mentoring me in research and academics throughout the years. I am particularly grateful for the several discussions and brainstorming sessions leading to amazing ideas. I am thankful to Dr. Kai Cheng for teaching me about the exciting field of nanoparticles functionalization for the drug delivery of cancer treatment. Lab members, colleagues and friends Dr. Xiaolian Sun, Dr. Sally Ho, Jonghun Lee, Dr. Sen Zhang, Michael Zompa, Ronald Okoth, Adriana Mendoza Garcia and the class of 2014 for their support in passing all the major obstacles together. I would also like to thank Liheng Wu, for his collaboration on FeAu alloy NPs, Guangming Jiang, for the synthesis of bcc-Fe NPs, Huiyuan Zhu helping with the electrochemical detection of H_2O_2. And all the other past and present members of the Sun Lab making it a fun place to work, providing respite

with volleyball matches, and teaching me about other emerging fields in catalysis and energy storage.

I would like to thank the following collaborators in my field as well: Dr. Yana Reshetnyak, Dr.Oleg Andreev, Dr. Lan Yao and Ramona Adochite at University of Rhode Island for the iron oxide pHLIP studies; Dr. Maureen Chung,Dr. Yuan Zhenglong and Zara Faghiri at Rhode Island Hospital for the Au-Fe_3O_4 dumbbell studies in theranostic applications; Professor John Q. Xiao, Professor James Kolodzey, Jun Wu, Dr. Nupur Bhargava and Jay Gupta at University of Delaware for providing magnetic tunneling junction chips for bio-sensor applications. I have to thank reseachers at Brown Joseph Orchardo, Anthony Mccormick, Geoff Williams, and Tun-Li Shen for their help in the instrumentation to characterize nanoparticles. I also have to thank my former mentor, Dr. Michael D. Mason, from University of Maine who introduced me to nanoparticles use in drug delivery and involved me the research lab to learn about the exciting drug delivery field of gold nanoparticles.

The 5-year long pursuing for PhD wouldn't have been possible without the continuous support of my family through the years. My brother, Ajaya K. Sigdel, who paved my way, guided me to continue in this path, and helped me tremendously throughout my graduate career; my mother, Maiya Sigdel, who has given me love, warmth and support from faraway place in Nepal and has been extremely patient with me while I followed this careerpath. I can't thank enough my grandmother, uncles and aunts who raised me and always wanted the best for me. My highly educated and influential family: Sigdels, Sharmas, Parajulis, Barals, Adhikaris, Bastolas, Regmis, who have nurtured me and also been the positive source of support throughout the years of my life.

Life at Brown wouldn’t be the same without the social support of great friends. I have been very lucky to find good, supportive people who inspire and amaze me with their research work, and make me a better person. I am very thankful that I have friends from all over the world, making my time at Brown very fruitful who taught me many things in life besides lab and research. There are many people who have been there for me that I can’t list thank you Inku Subedi, Don Ho, Sarthak Khanal, Cindy Lung, Alberto Palmores, Jay Sheth, Maria Lugo-Bolanos, and Priyanka Joshi for being there for me when I needed the most.

I dedicate this thesis to my father, Late Surya Kanta Sigdel, who always wanted me to be a strong, independent person and to lead. He always treated me like a son in a culture where daughters are usually raised to follow and not lead. He has been the true inspiration for me, had shaped me into who I am today and what I want to be in the future.

Thank you Dad!

Table of Contents

Abstract of "Biological Application of Magnetic Nanoparticles in Targeted Therapeutics and Diagnostics" by Aruna Sigdel, Ph.D., Brown University, May 2014

Theranostics, the combination of diagnosis and therapy, holds great promise for successful cancer therapy. It allows simultaneous monitoring of distribution, localization/release of a chemotherapy drug, and therapeutic response.

Gold (Au) and iron oxide (Fe_3O_4) nanoparticles (NPs) have been extensively studied for the theranostic applications due to their distinguished optical/magnetic properties, their biocompatibility, and their modifiable surface chemistry. In one study, I synthesized dumbbell-like Au-Fe_3O_4 NPs, which are both magnetically and optically active, and functionalized them with doxorubicin (DOX, a powerful cancer therapeutic drug) on the Au side via a pH sensitive Schiff-base bond and MUC1 antibody on Fe_3O_4 side for breast cancer targeting (MUC1-antigen is over-expressed in 95% of breast cancer cells). The efficacies of these theranostic NPs for targeting and therapy were evaluated both *in vitro* and *in vivo.* Our data show that the theranostic NPs target breast cancer cells and release DOX in low pH lysosomes to inhibit tumor growth. They are superior to the pure therapeutic drug.

I studied iron oxide (Fe_3O_4) nanoparticles (NPs) which are FDA approved as contrast agents in Magnetic Resonance Imaging (MRI). I synthesized, functionalized the Fe_3O_4 NPs with pH low insertion peptide (pHLIP) and studied their targeting ability to the cancer cells utilizing extracellular low pH environment of tumor.

I also studied an alternative approach for cancer therapy without using any conventional drugs. In this study, I synthesized FeAu alloy NPs and tested their controlled Fe-release in low pH environment. FeAu alloy NPs possesses plasmonic property that can be combined with theraperutic to monitor the therapeutic response. I noticed that the release Fe(0) can catalyze H_2O_2 decomposition into hydroxyl radical, one of the known reactive oxygen species (ROS). The overproduction of ROS causes rapid oxidation of biomolecules, leading to cell apoptosis. My preliminary tests showed that FeAu NPs are cytotoxic to cancer cells and can be used as a new generation of therapeutic drug.

Chapter 1 Magnetic Nanoparticles for Biomedical Applications

Introduction:

The emerging field of nanotechnology combined with molecular biology has developed into research area: nanobiotechnology. Nanobiotechnology deals with biological applications of nanoparticles ranging from bio-separation, sensors, detection, drug delivery, therapeutics, and diagnostics. Nanoparticles are multi-functional and bio-applicable due to their size and chemical composition creating unique properties such as high aspect ratio, unique chemical reactivity, optical interactions and magnetic properties.

Magnetic nanoparticles (MNPs) are well-established nanomaterials with controlled size, superparamagnetic properties which allows can be magnetized in the presence of external magnetic field and biocompatibility. These multi-functional properties are explored in various applications ranging from sensor, separation, detection, drug delivery, therapeutics and medical imaging [1, 2]. These unique properties of magnetic nanoparticles that open several doors to biological applications and the optimal design for targeted therapeutic is described in 1.1.

Multi-functional MNPs are designed with various polymer coatings, drugs, targeting agents, to increase the sensitivity and specificity of drug delivery and medical imaging. Different types of MNPs are explored for creating a better contrast in non-invasive magnetic resonance imaging, MRI. The therapeutics and diagnosis are combined for dual purposes of simultaneously diagnose, target drug, and monitor therapeutic response. The

unique properties of NPs are optimally designed and engineered for improved detection and efficiency of intended use.

Potential advantages of therapeutic NPs include a) the enhancement of therapeutic efficacy, b) delivery of drugs across a range of biological barriers including blood brain barrier, c) the ability to preserve the pharmaceutical properties of hydrophobic/hydrophilic drugs and maximize their efficacy, d) combine therapy with diagnosis to monitor progression of therapy in real-time, also recently known as theranostics e) ability to deliver drugs to the intracellular sites of action. Nanomaterials with different shape and sizes with composition of core/shell, liposomes, PEGylated-liposomes, micelles, dendrimers are currently used to design therapeutic NPs [3-6].

Furthermore, NPs have shown great promise as diagnostic tools in the field of biomedicine. Various electrochemical, colorimetric and magnetoresistive (MR) sensor based detection have been shown superior to the traditional enzyme based detection system. Enzyme-based biosensors are plagued by complicated immobilization processes and limited stabilities due to enzyme denaturation, preventing them from being applied in a real sensor device. The current bio-sensor system is more complicated by problems such as photobleaching and fluorescence quenching. NPs are best alternatives to the enzyme based detection system with lower detection limits and can be used in different conditions other than the physiological pH.

In my thesis, I will explore several magnetic nanoparticles such as superparamagnetic iron oxide nanoparticles (SPIONs), bi-functional Au-Fe_3O_4 NPs, FeAu alloy NPs and MnAu NPs for their targeted therapeutics and diagnostics properties. Well synthesized,

characterized and designed NPs with targeting ligands have high potential of yielding effective therapeutic treatment and diagnosis.

1.1 Magnetic Nanoparticle Properties

The magnetic nanoparticles (MNPs) size can be tuned from 1nm-100nm. Due to the presence of large percentage of surface atoms, nanoparticles (NPs), with particles size <20nm, have unique chemical properties that are not observed in their bulk forms [7]. With controlled size and crystallinity it is possible to obtain good magnetic moment closer to bulk without compromising the quality of nanoparticles (NPs). Iron oxide possesses magnetic saturation (Ms) moments of 92 emu/g (127 emu/g Fe) and 78 emu/g (111 emu/g Fe) for bulk magnetite and maghemite, respectively [1].

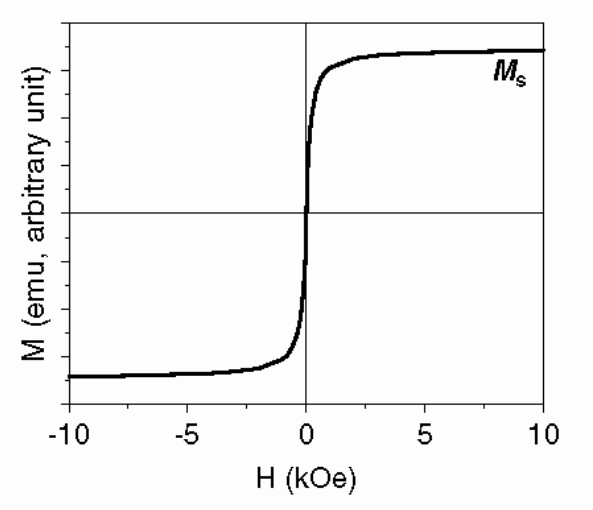

Figure 1: Hysteresis loop of magnetic nanoparticles showing superparamagnetic properties

Hysteresis loop of MNPs exhibits, zero coercivity in the absence of external magnetic field (Figure1). In the presence of external magnetic field, MNPs reach saturated magnetic moment (Ms) very quickly and once the external field is removed their magnetic moment returns to zero without retaining any magnetism. Such a feature known as superparamagnetism is very desirable, as the nanoparticles magnetism can be controlled when needed. It further ensures nanoparticles long-term stability and its use in bioapplications.

1.2 Factors to consider for biocompatibility and NP design

Several factors make the MNPs compatible with biological systems which create more opportunity to explore several biological applications. For a good therapeutic, diagnostic or detection all of these factors should be kept in mind while designing NPs.

1.2.1 Shape and size

Magnetic nanoparticles range from 5-100 nm which is within the size range of small biomolecules such as proteins and antibodies makes them ideal candidates to reach the cellular level. To avoid body's immune system or the reticuloendothelial system (RES) and clearance from liver and spleen for drug delivery, the ideal size <100nm enter cells. It has also been heavily studied that for the NPs to deliver to the nucleus < 40nm is ideal and <35nm to pass blood brain barrier [8, 9]. For MRI, a superparamagnetic nanoparticle with high magnetic moment is preferred, which is usually achieved with larger nanoparticle size greater than 30 nm. However, clustering of small magnetic nanoparticles to get hydrodynamic size has also shown better MRI contrast results [10].

1.2.2 Surface charge

Surface charge of NPs play very important role in determining the uptake and protein opsonization in the body. Our immune system easily recognizes the nanoparticles when they are injected intravenously into the body. Subsequently, the NPs are cleared out by phagocytes from the circulation within minutes of injection [11]. Positively charged NPs are taken up easily by all healthy and unhealthy cells whereas negatively charged NPs are less likely to be uptaken by healthy cells due to the surface charge of the cells. Ligands containing both positive and negative charge are also shown to be better (repulsion between proteins and ligands , less absorption to normal cells) also known as zwitterionic molecules [12]. However protein adsorption is still a problem that causes the NP aggregation or covers the targeting ligand. To increase the likelihood of in vivo targeting and uptake, it is necessary to minimize the binding of the proteins onto the surface of nanoparticles [13, 14]. Out of several types of polymers, ligands based on polyethylene glycol (PEG) has been known to reduced this adsorption and not cause aggregation of particles in the RES system[15, 16]. New generation MNPs are specific due to the various ligands mostly polymers with negative charge, hydrophilicity which give them better stability. Besides, peptides, antibodies are attached on the surface of the nanoparticles to make them further specific to the disease such as cancer, atherosclerosis, diabetes, or inflammation.

The magnetic nanoparticles range from (5nm-100nm) which is within the size range of small biomolecules such as protein, antibody which makes them ideal candidate to reach to the cellular level. For drug delivery, to avoid reticuloendothelial system (RES) and clearance from liver and spleen, it has been found that < 150nm, <100nm enter cells, <

40nm enter nucleus, <35nm pass blood brain barrier [8]. For MRI, superparamagnetic nanoparticles with high magnetic moment is preferred, which is usually larger nanoparticle size around >30nm. However, clustering of small magnetic nanoparticles to get hydrodynamic size has also shown better MRI contrast results [10, 17].

1.2.3 Non-Toxicity

For a drug delivery and diagnosis, NPs should not cause toxicity by themselves. Iron oxide is FDA approved as a T2 contrast agent for MRI. The iron oxide NPs itself aren't toxic to cells, a lot of toxicity arises from protein adsorption onto NP surface. Opsonization process is less for smaller nanoparticles and more hydrophilic particles. Polyethylene Glycol (PEG) and folic acid coating have less protein adsorption and makes nanoparticles invisible to RES. A good coating can decrease the toxicity tremendously.

Fewer toxicity research done *in vivo*, show there was no physiological damages to the tissues where nanoparticles were taken up. The study lasted 6 months after the iron oxide nanoparticle exposure [18]. It is believed that iron oxide is recycled by the body in the form of iron. These work as iron supplements in the body [19, 20]. However, further study needs to be done to confirm the fate of NPs in the body as the NP toxicity depends on the NPs material, shape, size, surface chare, and stability.

1.3 Surface Modification:

1.3.1 Ligand exchange

Magnetic nanoparticles that are synthesized in organic solution using organic surfactants and solvents such as oleic acid and oleylamine are not biocompatible. To make these nanoparticles water soluble and biocompatible ligand exchange can be used. Ligand

exchange is the change of ligands from organic phase to water phase. Sun et. al showed iron oxide had a good affinity to catechol unit. This catechol unit was further modified with polyethylene glycol (PEG) to further stabilize particles in water [21]. Similarly, others polymers such as PMIDA Nphosphonomethyl iminodiacetic acid, PEO polyethylene oxide, PVP polyvinyl pyrrolidinee, PEE polyethylenimine are also used to stabilize nanoparticles in water [22, 23]. The distribution depends on PEO chain length. Short ligands such as dimercaptosuccinic acid (DMSA), N-hydrosuccinic acid (NHS+ EDTA), citric acid also make NPs water soluble [22-24][6].

1.3.2 Ligand Addition

Phospholipids, with hydrophobic head and hydrophilic tails are often used to stabilize oleic acid coated SPIONs. Nanoparticles encapsulated within a phospholipid bilayer forms a vesicular structures called liposomes. These liposomes have considerable structural and pharmacokinetic advantages for drug delivery as they mimic the body's natural liposomes [24]. Another major advantage is these liposomes can incorporate both hydrophilic and hydrophobic therapeutic drugs. PEG incorporation into the phospholipids greatly reduces the opsonization process and thus increasing the circulation time.

1.4 Targeting

For high sensitivity of NPs in diagnostic, drug delivery or therapeutic applications it is important to get selective binding to the desired area. These can be achieved by conjugating or functionalizing bio-markers such as aptamers, antibodies, and peptides. Targeting is to deliver the cargo/drugs to the diseased area without dropping cargo/causing any side effects along the way. By targeting tumor it is possible to significantly reduce the amount of side toxicity caused by nanoparticles, therapeutics in

normal cells and vital organs such as lungs, liver and spleen. Targeting helps in cutting down therapeutic doses by concentrating the cargo in the diseased area.

Herceptin antibody is commonly used to target breast cancer overexpressing Her2/neu receptor. Cyclic (Arginylglycylaspartic) acid (cRGD) peptide is used to target $\alpha_V\beta_3$ integrin expressed on both tumor and tumor endothelial cells. In more general targeting, folic acid has been used as a ligand to target many human cancer cells including breast, ovarian, lung, renal and colon cancer which express receptor [25]. However, these extracellular phenotypic expressions, bio-markers and antibodies are subject to mutate thus the targeting capability can be changed. Besides, bio-markers another way to target cancer cells is to utilize extracellular tumor environment. Extracellular tumor environment is known to be hypoxic i.e. lack of oxygen and acidic (pH 5.5-6.5) because of poor clearance of lactic acid during anaerobic oxidation. Peptides such as pH low insertion peptide (pHLIP), cell penetrating peptides (CPPs) and smart polymers can be used to target tumors that take the advantage of this low pH environment of tumor. Permeation enhancer such as TAT peptides can enhance the degree of NP uptake [26].

Currently, extracellular pH targeting nanotechnology includes pH responsive micelles and pop-up micelles that expose drugs or receptors at the low pH environment. These systems have been able to accumulate drugs at tumor sites rather than normal tissues and organs [27]. pH targeting approach is regarded as more general strategy than conventional specific tumor cell surface targeting. Low pH microclimate of tumor holds true for small and large solid tumor in different stages [28]. In this thesis, low pH targeting is utilized in Chapter 2 and Chapter 3 for diagnosis.

Another interesting way for targeting is using intracellular low pH targeting. Intracellular liposomes and endosomes have pH 5-5.5 and pH 6 respectively. This property can be utilized to target these cellular compartments for release of therapeutics, and other desired molecule such as DNA, siRNA inside the cytoplasm which then can be carried into the nucleus. This kind of targeting is used in my thesis using smart polymer to release therapeutic drug, doxorubicin (DOX). In this thesis, we utilize intracellular low pH in Au-Fe_3O_4 dumbbell based theranostics system using pH sensitive polymer in Chapter 3.

Targeting tumor benefits in drug delivery by reducing toxicity and also in MRI by increasing contrast between healthy and tumor tissue. To engineer an effective diagnostic system all the factors incuding material, material chemical properties, magnetic properties, shape, size, coating, surface modification and targeting should be considered.

Chapter 2 Superparamagnetic Iron Oxide Nanoparticles for Targeting Tumor Using pHLIP Peptide

2.1 Introduction

2.1.1 SPIONs uses in MRI

Superparamagnetic iron oxide nanoparticles (SPIONs) hold great promise for realizing early tumor diagnosis and therapy [29]. SPIONs are FDA approved T_2 contrast agents for magnetic resonance imaging (MRI). MRI is a non-invasive medical imaging with high spatial resolution used in tumor diagnosis [24]. Currently, T_2 contrast agents Ferridex, Combidex and Endorem^{TM} are FDA approved and available commercially. But these commercialized magnetic NPs are in poor quality with the suboptimal crystallinity, large size distribution, and variable composition. The superparamagnetic iron oxide nanoparticles (SPIONs) properties can be chemically modified to achieve a better contrast agent. Monodisperse NPs with high crystallinity and higher magnetic moments with good stability and biocompatibility are desired for the dual purposes of diagnosis and therapy.

The dual functional properties of SPIONs are further explored in drug delivery and MRI. In one particular study, SPIONs are loaded with therapeutic drugs, Doxorubicin (DOX) and Paclitaxel (PTX). T_2 relaxivity values of drug loaded MNPs were comparable to that of Ferridex IV, 4.8s-1 ug-1 mL [23]. SPIONs not only work as a MRI contrast agent, but also as drug delivery vehicle. Nanoparticles via passive targeting can reach tumor due to the enhanced permeability and retention (EPR) effect, however the distribution is not uniform. SPIONs concentrate near the tumor vasculature as a result from the increased

interstitial fluid pressure and the dense extracellular matrix found in the in vivo tumor environment.[30, 31,32]. The drug delivery and imaging efficiency can be further increased by active tumor targeting.

Multimodality of MNPs are explored for high selectivity and specificity, combining targeting and imaging. The ultrasmall 4.5nm SPIONs are funtionalized with a cyclic arginine-glycine-aspartic acid (cRGD) peptide. The c(RGDyK) functions to target specifically to various tumor cells expressing cell adhesion molecule integrin $\alpha_v\beta_3$. The as-synthesized SPIONs were stabilized by 4-methylcatechol (4-MC). The 4-MC is further conjugated with a cyclic c(RGDyK) *via* the Mannich reaction, producing the stable ultrasmall c(RGDyK)-MC- Fe_3O_4 NPs (overall size at 8.4 ± 1.0 nm) (Figure 2). *In vivo* study in mice bearing U87MG human glioblastoma reveals the r_2 relaxavity of the c(RGDyK)-MC- Fe_3O_4 NPs to be 165 $mM^{-1}\cdot s^{-1}$ at a 3 T field, larger than that of the commercial Feridex (104 $mM^{-1}\cdot s^{-1}$) with similar core size. The tumor MR signal intensity decreases by 42 ± 5% after the injection of c(RGDyK)-MC-Fe_3O_4 NPs dispersion (Fig. 2b & c), while subsequent Prussian blue staining (Fig. 2d) visualizes the NPs in the tumor mostly populate on the integrin expressing tumor vasculature and tumor cells {Xie, 2008 #146}.

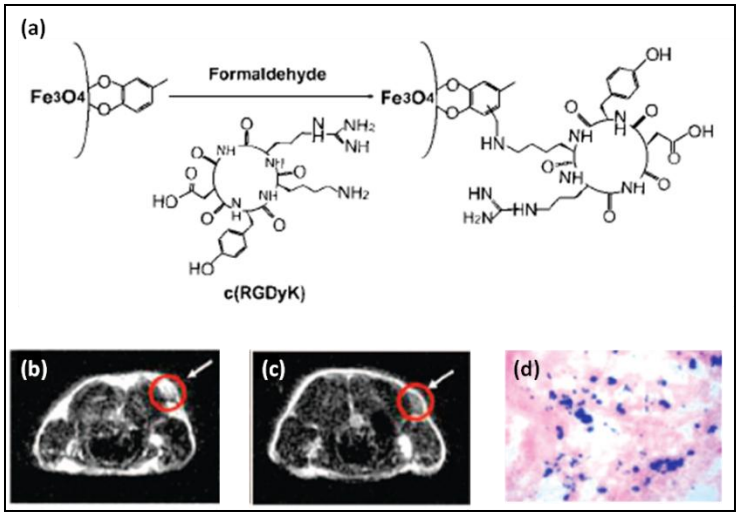

Figure 2: Schematic illustration of the fabrication of c(RGDyK)-MC- Fe_3O_4 NPs based on Mannich reaction; (b, c) MRI of the cross section of the U87MG tumors implanted in mice: (b) without NPs, (c) with the injection of 300 μg of c(RGDyK)-MC- Fe_3O_4 NPs; (d) Prussian blue staining of U87MG tumors in the presence of c(RGDyK)-MC- Fe_3O_4 NPs. Adapted from Ref. Xie et.al with permissions by American Chemical Society .

2.1.2 Targeting using pHLIP peptide

Targeted NPs increases the sensitivity by concentrating the cargo in the diseased area. However, biomarkers such as antigen are subject to mutation. Antigen cannot be relied upon for the initial diagnosis other hallmarks of tumor are explored for targeting. Microenvironment of a tumor is hypoxic and acidic due to the production of lactic acid and poor clearance of the released CO_2. Normal cells have extracellular pH of 7.4 whereas some tumor cells have significantly lower pH ranging from 5.5 -6.5. Therefore targeting of tumor acidity might represent novel approach in diagnosing and predicting tumor aggressiveness. Several pH-sensitive imaging and drug delivery systems have thus been introduced in which diagnostic or therapeutic agent release is specifically triggered by the acidic tumor microenvironment [33-37].

Figure : In (a) pHLIP peptide at pH 7.4 is outside the cell membrane (b) pHLIP at low pH forms α-helix and inserts into cell membrane C-terminus is inside the cell, taken from ref [38]

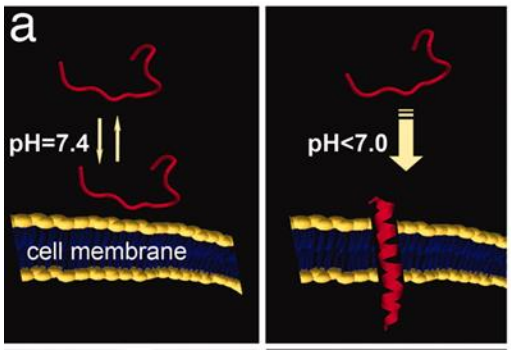

The pH (low) insertion peptide (pHLIP) represents a unique class of water-soluble membrane polypeptides capable to undergo a pH-dependent membrane-associated folding. At normal pH is globular however at low pH, this peptide forms a helix and inserts into the cell membrane. This α-helix formation is triggered by the increase of the peptide hydrophobicity due to the protonation of Asp (N) residues induced by low pH. The membrane insertion and pHLIP residue is shown in the figure 1. Andreev et.al, studied the well-characterized WT-pHLIP for translocation of toxins and peptide nucleic acids into the cytoplasm of cancer cells, delivery of various imaging agents and targeting of both liposomes and gold nanoparticles to tumors and other acidic diseased tissue [39-46].

2.1.3 Liposomal drugs

Phospholipids have been used in delivering several drugs since decades which mimics the liposomes in the body, are biocompatible. Furthermore, Polyethylene glycol (PEG)-phospholipid coating increases the retention time of drugs, reduces uptake in liver and spleen while enhancing uptake in tumors [47]. The coating and surface charge of a NP is equally important for the longevity and stability in the body. The negative surface charge has been proven to reduce the opsonization process as well as less uptake in normal cells

[48]. Recently, Doxil (Liposomal Doxorubicin) has been FDA approved as therapeutic agent. Current drug strategy includes liposomes conjugated with antibodies for targeting. These PEG-phospholipids can be used to design NP system with multifunctional purposes.

The term magnetoliposome is usually used to indicate a colloidal system in which a magnetic core, generally made up of iron oxide nanoparticles, is surrounded by a phospholipid bilayer. Several liposome are used for functionalization as they have longer circulation time and thus used in drug delivery, hyperthermia and imaging [49]. In some cases, solid lipid nanoparticles (SLNs) in the range of 50-100nm have been shown to be more efficient than liposomes due to their stability. Studies on SLNs demonstrated the advantages of the traditional liposomal systems whie avoiding toxicity and long-term stability [50].

Taking advantage of both liposomal and NPs benefits we designed SPIONs with Phospholipids and then further functionalized with pHLIP to target tumor. Up to date SPIONs remain the only magnetic nanoparticles that have been approved for clinical use and phospholipids are shown to have better retention time. Furthermore, we plan to target the extracellular environment by delivering NPs into the tumor for better diagnosis.

We studied the SPIONs with different PEGylated and non-PEGylated phospholipids, studied their stability in different medium, and compared their cellular uptake in the carcinoma cells. We also looked at the targeting ability of pHLIP peptide and studied *in vitro* and *in vivo* uptake. Liposomal pHLIP show some side-toxicity in the kidneys due

to the low pH of kidney. To overcome this barrier, as well to be able to diagnose cancer we incorporated the two systems.

2.2 Methods:

2.2.1 Characterization:

Transmission Electron Microscopy (TEM) images are collected on a Philips EM 420 (120 kV) or a Philips FEI CM 20 (200 kV). A drop of NPs in hexane is put in a carbon TEM grid and dried for 15 min under vacuum. The elemental analysis of NPs was performed on a JY2000 Ultrace ICP Atomic Emission Spectrometer (ICP-AES) equipped with a JY AS 421 autosampler and 2400 g/mm holographic grating. To prepare NPs sample for ICP, 20 µL NPs in hexane or NPs in water dispersion was digested by 10 drops of freshly prepared aqua regia in a medium heat. The clear solution was redispersed in 5 mL 2% nitric acid. UV/vis spectra for quantification of pHLIP peptide and Alexa dye was recorded on a Perkin Elmer Lambda 35 spectrometer. The hydrodynamic size and zeta potential of the NPs in DI water, PBS and DMEM was evaluated using a Malvern Zeta Sizer Nano S-90* dynamic light scattering (DLS) instrument.

2.2.2 Synthesis of 8nm Fe_3O_4 Nanoparticles:

Fe_3O_4 NPs were synthesized by following the pyrolysis method published previously [6]. Briefly, 0.700g $Fe(acac)_3$ was dissolved in a solution of benzyl ether and oleylamine. The solution was heated at 110 °C for 1 h under nitrogen flow. The stopcock was closed and the solution heated to 300°C at the rate of 15°C /min. The reaction was refluxed at 300°C for 2 h. After cooling down to RT, it is precipitated by 80ml ethanol, centrifuged twice at

8000rpm for 8min and washed. Finally, the product is redispersed in hexane. NPs size and shape was characterized by TEM.

2.2.3 Nanoparticle Functionalization/Modification:

All the phospholipids were obtained from Avanti lipids and used without further purification. Total phospholipid 3.5 times of weight of Fe_3O_4 NPs (freshly prepared without extra oleylamine as surfactant) were dissolved in chloroform (DSPE-PEG 2000-COOH 92% by weight, DSPE-PEG 2000-maleimide 5% for cys-pHLIP peptide conjugation and 3% DSPE-PEG 2000-NH_2 for $Alexa_{750}$ dye conjugation). Then, phospholipids and as synthesized oleylamine, oleic acid coated Fe_3O_4 NPs were shaken for 30 min in chloroform. Chloroform was evaporated using Rotovap for 2 hr. Then, PBS 1X pH 8.0 buffer was added that formed the micelle nanoparticles. Cys-pHLIP peptide was added first for maleimide conjugation for 6 hr then $alexa_{750}$ dye was added for amine-ester conjugation. The whole reaction was shaken at RT for 24 hr. Then, the nanoparticles were purified using Sephadex PD-10 size exclusion column, 10ml PBS to clean the column, then 2ml NPs were added, once the NPs embedded through the column, 4ml PBS was added. NPs were collected based on color. After NPs, columns were washed with 20ml buffer to be re-used. NPs were dialyze against PBS 1X buffer using 100K dialysis tubing (Spectrum Laboratories) and then filtered through 0.22um (PVDF) sterile filter for 3-4 ml NPs sample. If the NPs concentration was low for cell study, the NPs were concentrated using vivaspin concentrator (10,000 MWCO) at 1500 rpm for 8 min.

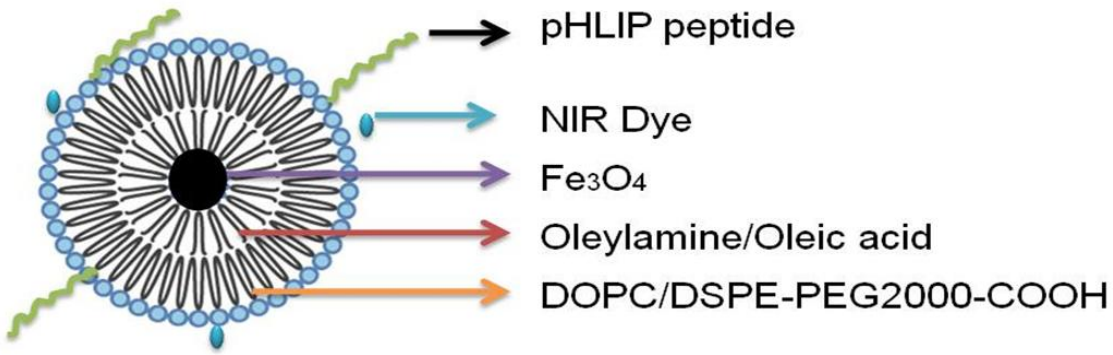

Figure 3: Schematic illustration of ligand addition using different phospholipids

DSPE-PEG 2000 COOH

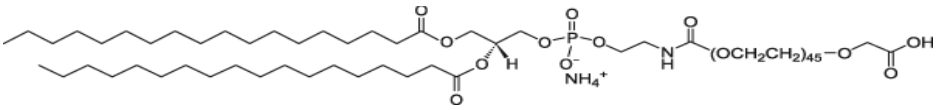

DOPC

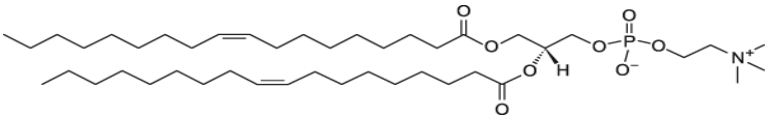

2.2.4 Ligand addition and pHLIP, Alexa750 dye conjugation :

Phospholipids were obtained from Avanti lipids. Total phospholipid 3.5 times of weight of Fe_3O_4 nanoparticles were dissolved in chloroform (DOPC 30% by weight, DSPE-PEG 2000-COOH 62% by weight), DSPE-PEG 2000-maleimide 5% for cys-pHLIP peptide conjugation and 3% DSPE-PEG 2000-NH2 for $Alexa_{750}$ dye conjugation). Then, Phospholipids and as synthesized oleylamine,oleic acid coated Fe_3O_4 nanoparticles were shaken for 30 min in chloroform. Chloroform was evaporated using Rotovap for 2 hr. Then, PBS 1X pH 8.0 buffer was added that formed the micelle nanoparticles. Cys-

pHLIP peptide was added first for maleimide conjugation for 6 hr then alexa$_{750}$ dye was added for amine-ester conjugation. The whole reaction was shaken at RT for 24 hr. Then, the nanoparticles were purified using PD-10 size exclusion column, 100K dialysis tubing and then filtered through 0.22um sterile filter. UV-vis was done for Alexa concentration (Absorbance at 750 was measured, E= 290,000cm^{-1}M^{-1}). ICP-AES was done to measure Fe concentration. MALDI-MS (alpha-cyano matrix) was performed to check pHLIP and amine-ester conjugation. Hydrodynamic sizes of particles were measured using DLS for stability.

2.2.5 Quantification of pHLIP peptide per nanoparticle using Ellman's reagent.

Figure 4: Reaction of thiol with DTNB for the quantification of peptide

Fe_3O_4 -pHLIP nanoparticles were filtered through 100k eppendorf tube, where bound Fe_3O_4-pHLIP remains on filter whereas unbound pHLIP passes through filter and collected as supernatant. Free sulfur in pHLIP reacts with DTNB (5,5-dithio-bis-(2nitrobenzoic acid) to form yellow color due to the release of TNB (2-nitro-5 thiobenzoic acid); TNB absorbs @ 410 nm. The number of unreacted sulfur was subtracted from original pHLIP to get the number of reacted pHLIP. Cysteine was used to generate a standard curve and extrapolated the data.

Number of Fe_3O_4 nanoparticles using elemental analysis = 2.13E+15

Number of pHLIP using avogrado's number = 1.09E+16

Number of pHLIP per Fe_3O_4 nanoparticles ~ 5

After purification, dialysis and PD-10, The UV-vis is also performed with the same concentration of control NPs and NP-pHLIP at 260, 280, 320 nm. The concentration of bound- pHLIP peptide is measured using A_{260}. Normalized using control NPs as lipids and NPs have absorbance as well.

2.2.6 In vitro cellular uptake study:

M4A4-GFP ductal (breast) carcinoma cells were plated at normal pH 7.4 and low pH 6.5 DMEM with 10% FBS, 1% Pen Strep. After 85% confluency, cells were washed 3X with PBS. Fresh DMEM was substituted and they were treated with NP control and NP-pHLIP at 50ug Fe/ml and incubated at 37C in 5% CO_2. After 24 hr, the cells were washed 2X with PBS to get rid of extra NPs, and trypsinized with 0.05% trypsin. The cell pellet was washed again to get rid of unbound NPs. After that, cells were digested in 2ml aqua-regia under gentle heat and 1ml H_2O_2 to dissolve any fat from cells. The clear solution was redispersed in 5 mL 2% nitric acid. ICP-AES was performed for Fe concentration. Control cells without treatment were used for natural Fe concentration. The graph shows pH dependent characteristics of pHLIP peptide. As more nanoparticles are uptaken by cells at low pH comparing to normal pH.

2.2.7 Prussian Blue staining for cells visualization to study distribution of SPIONs in cells

HeLa-GFP cells were seeded in an 8-chamber slide (Lab-Tek™, Thermo Scientific; Rochester, NY). 10^5 cells were treated at pH 6.5 with 0.05, 0.1 mg metal in 200 μL of serum-free DMEM at 37°C under 5% CO_2. After 1 h incubation, the treatment solution

was removed and cells were washed twice with serum-free DMEM (pH 7.4), and once with sterile PBS (pH7.4). Cells were fixed with cold methanol at -20°C for 15 min, and then washed twice with sterile PBS (pH7.4) and once with deionized water. After air drying, the chamber walls were removed and cells slides were developed with Prussian Blue for 10 min. NOTE, various time were tested with developing time 5, 10, 20 and 30 min to find out which worked best. Cells incubated with Prussian solution were rinsed twice with deionized water, and were ready to be viewed under a microscope.

2.2.8 Cellular uptake of SPIONs to quantify the uptake of SPIONs in cells

Incubation of SPIONs with cell were done in suspension. Typically, a cell suspension was prepared by dissociating 80-90% confluent Hela-GFP cells grown in 75cm^2 flask with trypsin, EDTA. Trypsinized cells were counted using a hemacytometer and diluted to 10^6 cells/ml in serum-free media. 0.1 mg SPIONS were incubated with 10^5 cells in 1mL of the desired solution (DMEM (pH6.5) or DMEM (pH7.4)) for 1 hr at 37°C (in triplicate for each pH). After incubation, the cells were pelleted by centrifugation (2000 rpm, 4min). Then the cells were resuspended in 500uL fresh serum-free media and centrifuged for the second time.

The second pellet were resuspended in 1M HCl and treated with Prussian blue solution to determine amount of metal spectrophotmetrically (by absorbance). Absorbance measurements were carried out at 750 nm using a Genesys 10S UV-Vis Spectrophotometer (Thermo Scientific).

For calibration we used: i) non-treated cells, ii) 200 ul of 10^5 cells treated with 0.02, 0.04, 0.06, 0.08, 0.1 mg of SPIONS, but no centrifugation (no separation of cells from

SPIONs), thus we know the metal concentration in each sample. In both cases, 1M HCL and Prussian blue solution was added. All the calibration points were graphed and analyzed using a linear fit. The quantification of SPIONs was calculated, according to the equation:

$$Absorbance\ of\ the\ sample = Intercept\ of the\ plot + Slope of\ the\ plot\ x\ Concerntration\ of\ SPIONs$$

2.2.9 In vivo experiment:

M4A4 ductal carcinoma cells were subcutaneously injected into the right flank of immune-compromised nude mice and let the tumor grow for 2-3 weeks. Mice were grouped into five categories for control, Intravenous (IV) NP control and (IV) NP-pHLIP and Intratumoral (IT) NP control and IT NP-pHLIP. NP-pHLIP and NP-control were injected at 50ug/ml of Fe concentration or based on Alexa concentration for NIR imaging. After 24 hr, mice were sacrificed for biodistribution. ICP-AES was used to do elemental analysis. Previous method of aqua-regia, H_2O_2 were used under heat and re-dispersed in 5% HNO_3 solution.

2.3 RESULTS:

Ligand addition was performed on as-synthesized Fe_3O_4 NPs with oleate coating using DSPE-PEG-COOH and DSPE-PEG-maleimide. After the formation of magnetoliposome or the SPIONs-PEG-COOH in PBS 8.0 the nanoparticles were treated with SH-pHLIP for the maleimide-thiol reaction to occur at RT (Figure 5). SPIONs-PEG-pHLIP was

formed which was then further purified using dialysis tube (30,000 MWCO) for 24 hr then run through PD-10 desalting column and finally 0.22um sterile filter.

Pure pHLIP peptide has 36 amino acids and MW of 4144g/mol showing peak at 4144 (m/z) and also a peak at 8279 (m/z) caused by the dimerization of pHLIP via sulfide bonds present in cysteine residue. The conjugation between DSPE-PEG2000-maleimide and pHLIP peptide is accounted by the peak around 7100 (m/z) from MALDI-MS. MW of DSPE-PEG2000-maleimide 2941.64 g/mol + MW 4144.67 g/mol = 7086.31 (m/z)

SPIONs-lipid-PEG-pHLIP (100% DSPE-PEG-pHLIP)

SPIONs-lipid-PEG (100% DSPE-PEG-COOH)

pHLIP – WT-pHLIP with Cys residues at the N-terminus M.W. about 4.15kDa

2.3.1 *Scheme of SPIONs coating*

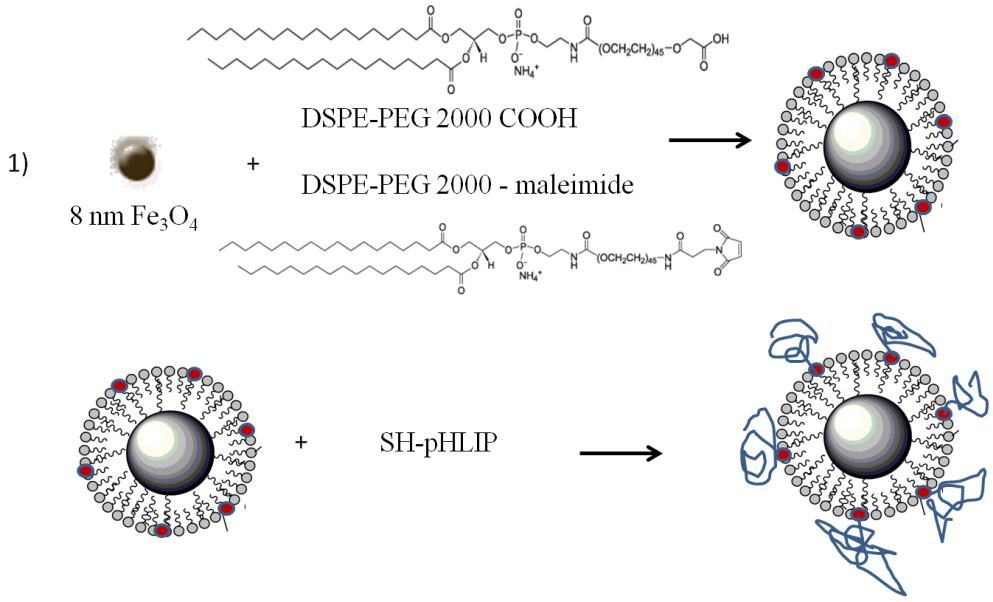

Figure 5 Schematic presentation of Fe_3O_4 NPs coating with DSPE-PEG-COOH and pHLIP peptide

2.3.2 *Synthesis and Characterization of NPs*

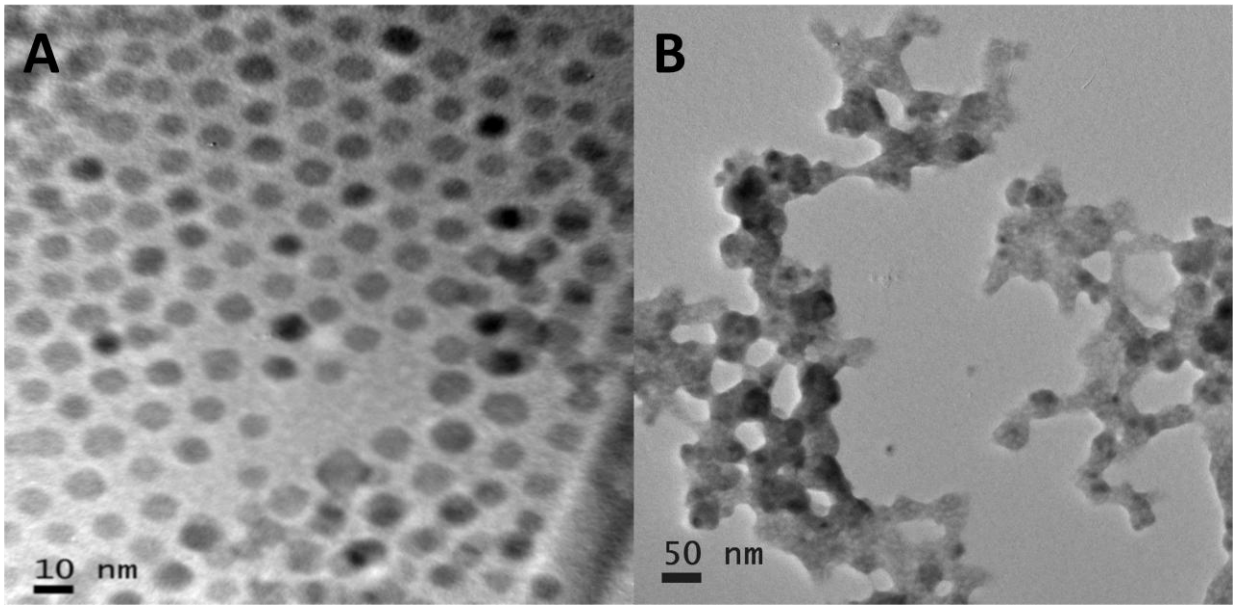

Figure 6: TEM images of A) 8nm as synthesized Fe_3O_4 NPs in hexane B) Fe_3O_4 - PEG-COOH in water

The synthesis of 8nm Fe_3O_4 NPs was very consistent from batch to batch. TEM and DLS were first used to characterize nanoparticles before the ligand addition and functionalization with pHLIP. Figure 6 shows the monodisperse 8 nm Fe_3O_4 NPs (A) and ligand addition (B).

Table 1: DLS of Nanoparticles showing increase in hydrodynamic size after pHLIP functionalization and the repeatablitly of the ligand addition protocol

Batch 1: 4/25/12	Fe_3O_4 -DSPE-PEG-COOH	32.7±4 nm
Batch 2: 5/07/12	Fe_3O_4 -DSPE-PEG-pHLIP	43.82 ±7nm
Batch 3: 6/18/12	Fe_3O_4 -DSPE-	32.7 ±7nm

	PEG-COOH	
Batch 4: 7/24/12	Fe_3O_4 -DSPE- PEG- pHLIP	43.8± 5 nm

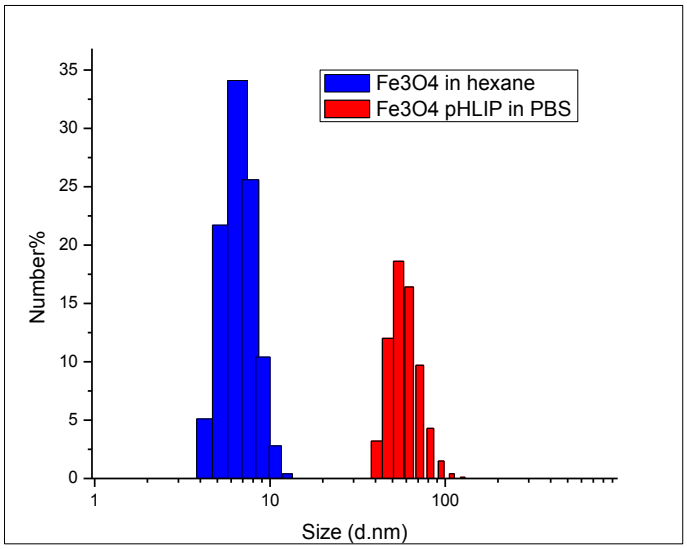

Figure 7 : Hydrodynamic size of as synthesized Fe_3O_4 NPs dispersed in hexane and Fe_3O_4 NPs with pHLIP functionalization dispersed in PBS.

The hydrodynamic size of as-synthesized Fe_3O_4 NPs in hexane is 8±2 nm. The hydrodynamic size of Fe_3O_4 -DSPE-PEG2000-pHLIP NPs is 50±5 nm. The increase in size accounts for Fe_3O_4-DSPE-PEG2000-pHLIP NPs accounts for the hydrodynamic size of PEG_{2000} of about 16nm and 3nm of Oleic acid and Oleylamine surfactants. Hydrodynamic size is increased as expected after ligand exchange with phospholipids and pHLIP peptide.

2.4 Colloidal Stability of NPs

Two formulations of SPIONs with pHLIP and without pHLIP were prepared. Fe_3O_4-PEG-pHLIP and Fe_3O_4 -PEG-COOH dissolved in DI water was kept in a cuvette in a water bath at 37°C. At different time points the DLS and Zeta potential was measured. The initial hydrodynamic size within an hour is observed to be reduced due to the high temperature Figure 8 (top). Newtonian motion increased as phospholipids are viscous. However after 1 day, NPs are stable with hydrodynamic size 40±7nm.

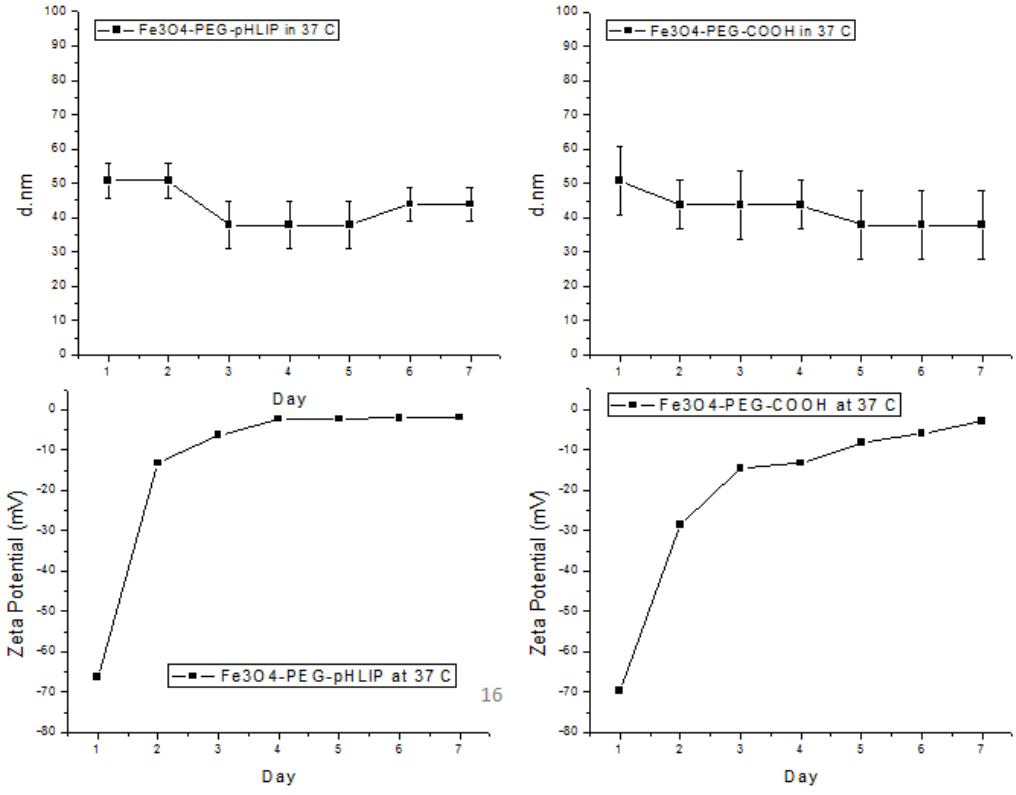

Figure 8: Hydrodynamic size and zeta potential of as synthesized Fe_3O_4 –PEG-pHLIP and Fe_3O_4-PEG-COOH in DI water for 7 days

Figure 8 illustrates the decrease in zeta potential in water incubated at 37C. In the first day, the value of zeta potential for Fe_3O_4-PEG-pHLIP nanoparticles is – 65 mV, showing an excellent stability in water. Within one day, the value of zeta potential drops significantly, reaching a value of – 15 mV, and therefore a region of incipient instability. The high zeta potential could be easily maintained by dispersing the nanoparticle in the slightly basic PBS 8.0 buffer.

2.4.1 MALDI-MS characterization

To introduce pHLIP in a liposome coat, we conjugated DSPE-PEG2000- maleimide lipid with Cys residue in the N-terminal region of pHLIP. The conjugation product was characterized by MALDI- mass spectrometry. The narrow peak at 4154 Da corresponds to pHLIP, and the broad peak centered at ~7000 Da corresponds to the conjugation product DSPE-PEG2000-pHLIP.

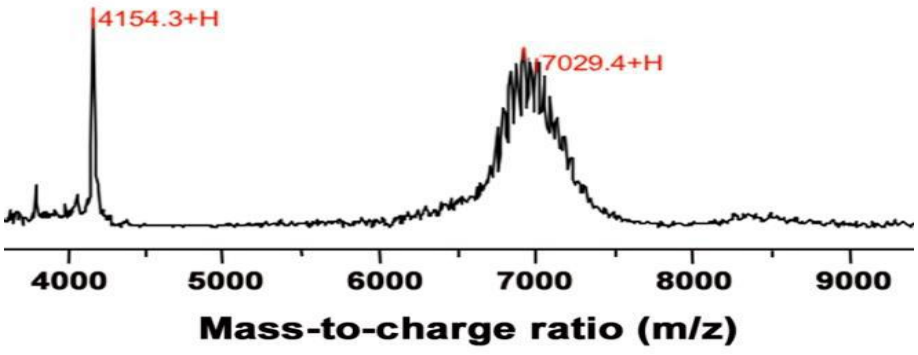

Figure 9: MALDI-mass spectrum of DSPE-PEG2000-pHLIP

The narrow peak at 4154 corresponds to the pHLIP peptide. The broad peak centered at ~7000 Da corresponds to the conjugated product DSPE-PEG2000-pHLIP as shown in figure 10. The individual spikes on the broad peak differ from each other by the repeating unit(s) of PEG (mass: 44 Da).

2.4.2 In vitro Experiment

2.4.3 Cellular Uptake in 30min and 60 min

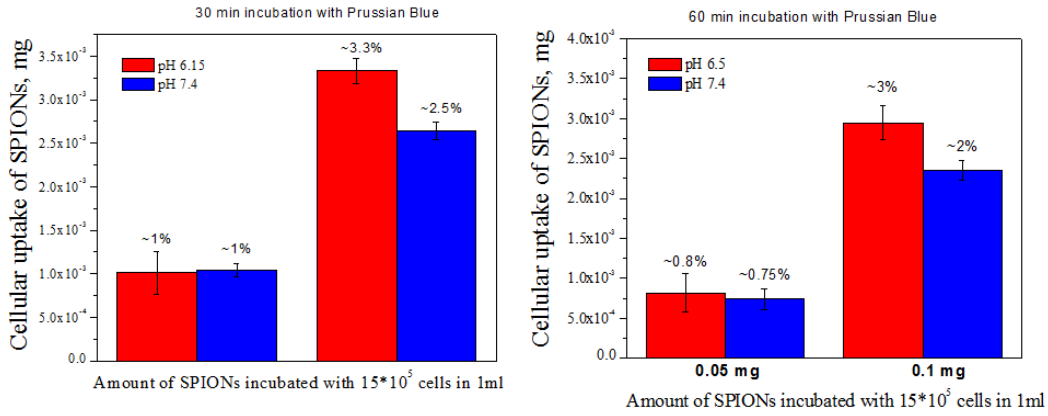

Figure 10: Cellular uptake of NP and NP-pHLIP at low pH and normal pH at 30 min and 60 min incubated with 0.05mg and 0.1 mg of nanoparticles based on Fe concentration.

M4A4 cells were plated at $1.5*10^5$ cells and treated with 0.05, 0.1 mg of SPIONs at different pH. As a control we used cells non-treated with SPIONs, but treated with Prussian Blue and cells treated with SPIONS but non-treated with Prussian blue. At 0.05mg of SPIONs we do not see much difference between the uptake at both 30 min and 60 min. However, at 0.1mg of SPIONs the difference between cellular uptake is clearly visible pH 6.15 (red) and pH 7.4 (blue) as shown in figure 11. At lower concentration of

nanoparticles, the pHLIP peptide did not show any targeting ability. However, at the higher concentration, the difference of 1.0E+4mg is significant in diagnosing the tumor from non-tumorous cells or delivering that much more drugs to tumor region than the cancerous cells. We modified the surface functionalization to get better cell uptake.

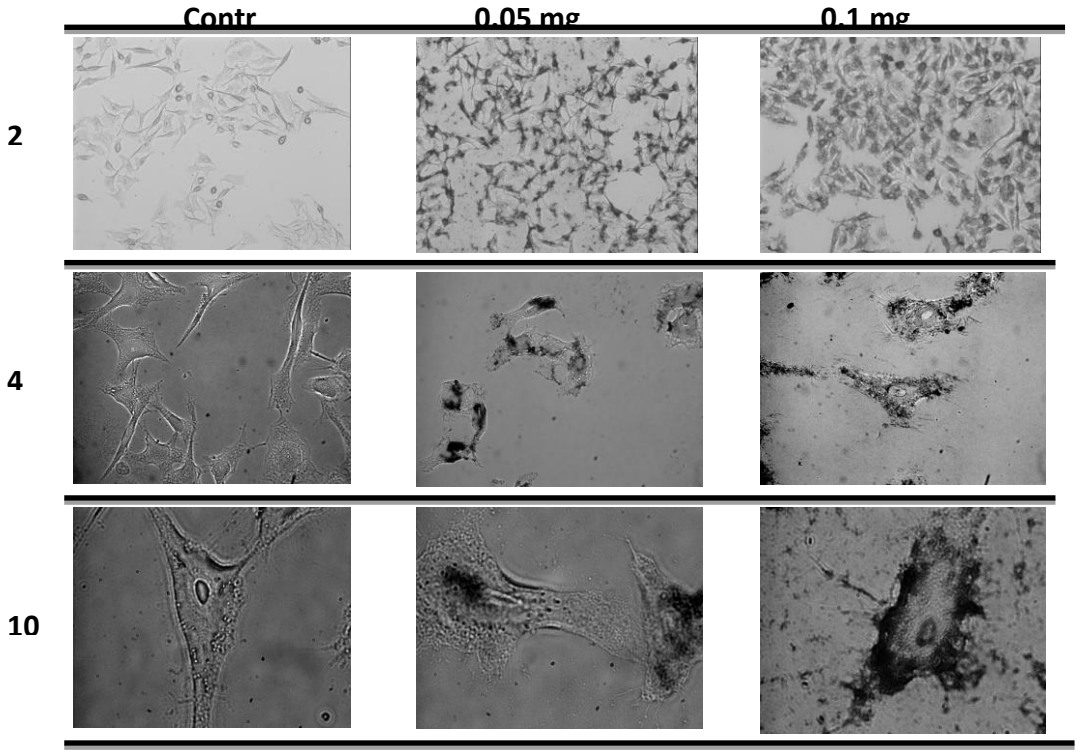

Figure 11: Distribution of SPIONs in cells at pH 5.9, Control cells, 0.05mg SPIONs and 0.1 mg SPIONs, 105 cells at pH 6.5 with 0.05, 0.1 mg metal in 200 µL of serum-free DMEM at 37°C under 5% CO2, Prussian Blue staining was used for cell visualization

2.5 SPIONs-PEG-pHLIP Cellular Uptake and Viability

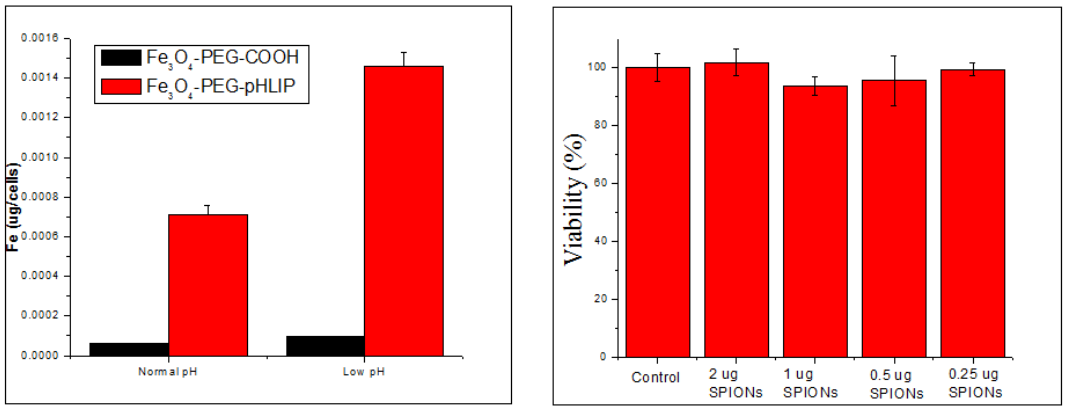

Figure 12: Cellular uptake of NP and NP-pHLIP at low pH and normal pH at 50ug/ml Fe concentration (left) and Viability of Cells using MTS assay of M4A4 carcinoma cells (right)

M4A4 cancer cell lines were plated in T25 in DMEM with 10% FBS medium. 50ug/ml Fe concentration was incubated for 24 hr after washing. The cells were washed again with PBS 3X and trypsinized. Higher uptake of NPs was observed in cells with low pH environment. The pH medium was only regulated in the beginning. As the cells are cancerous, within 24 hours they start to acidify the medium, in which case normal pH also becomes acidic over few hours of incubation. This was tested by the pH meter to test the pH of medium after 24 h. The cells were washed three times and ICP-AES was performed to measure the Fe concentration.

In the low pH, the cellular uptake is drastically higher about 15 times for Fe_3O_4 -PEG-pHLIP Figure 12 (left). This demonstrates the targeting ability of the pHLIP peptide in low pH. The 50ug/ml Fe concentration was used for the test.

2.5.1 Cell viability using MTS assay

The cells were incubated at 20,000 per cell well and different concentrations of SPIONs were treated in triplicates. The cells were viable for all SPION concentration 2ug, 1ug, 0.5ug and 0.25ug of Fe incubated in the M4A4 carcinoma cells (Figure 12: Cellular uptake of NP and NP-pHLIP at low pH and normal pH at 50ug/ml Fe concentration (left) and Viability of Cells using MTS assay of M4A4 carcinoma cells (right). This suggests that our SPION construct is non-toxic to cancer cells.

In vitro cellular experiments demonstrated our SPION-PEG-pHLIP are stable, repeatable and non-toxic to the cells with targeting ability in low pH cells thus we moved forward to test these NPs *in vivo*.

2.6 *In vivo* Experiment

After successful *in vitro* experiments showing good targeting, cell uptake and non-toxicity, we tested our NP construct *in vivo*. Our ultimate goal of the experiment is to see the targeting capability of pHLIP peptide, and to obtain good amount of NPs in the targeted area for diagnosis.

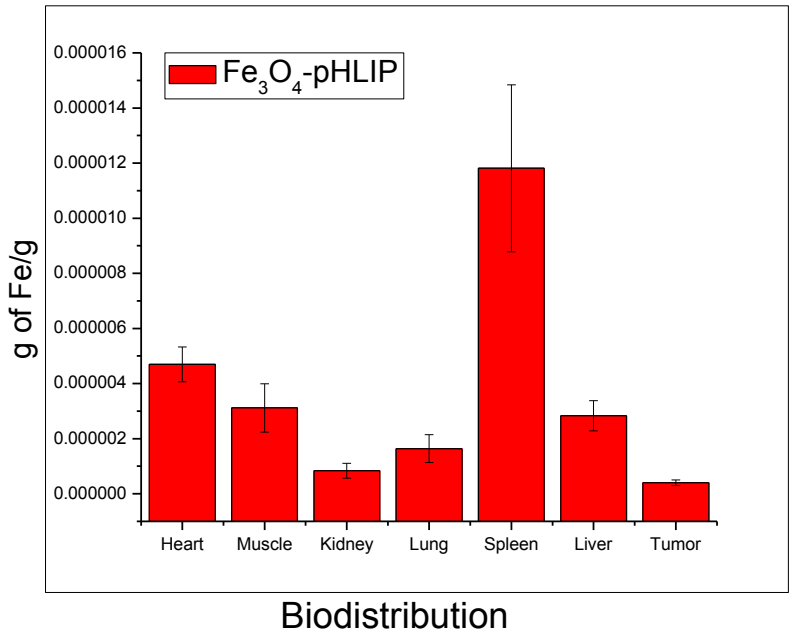

Figure 13: Biodistribution of Intra-veinous injection of 50ug of Fe/ml of Fe_3O_4 NPs with pHLIP treated for 24 hr

M4A4 cancer cells were subcutaneously injected into the right flank of mouse. After three weeks, IV injection of 50ug Fe/ml Fe_3O_4-pHLIP was performed. ICP-AES was used to do the elemental analysis. From the biodistribution, we observe that the lung, liver and kidney uptake are significantly reduced than compared to other studies. We have significant amount of nanoparticles present in tumor, which is significant enough to create contrast with the neighboring normal tissues.

2.7 Fe_3O_4 NPs with Alexa NPs as model drug for NIR imaging

The drug delivery ability of SPIONs was modeled by using $Alexa_{750}$ dye. The DOPC 30% by weight, DSPE-PEG_{2000}-COOH 62% by weight, DSPE-PEG_{2000}-maleimide 5% for cys-pHLIP peptide conjugation and 3% DSPE-PEG_{2000}-NH_2 for $Alexa_{750}$ dye conjugation. Cys-pHLIP peptide was added first for maleimide conjugation for 6 hr then

Alexa$_{750}$ dye was added for amine-ester conjugation. After purification, UV-vis was used to get the concentration of Alexa$_{750}$ dye. In this particular experiment, the concentration of pHLIP was quite low.

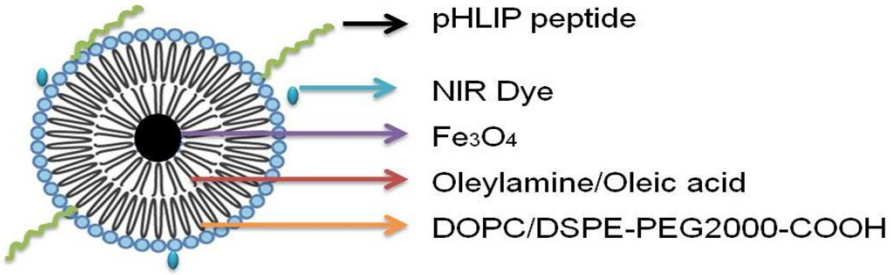

Figure 14: Schematic illustration of formation of SPIONs-NIR dye for in vivo NIR imaging

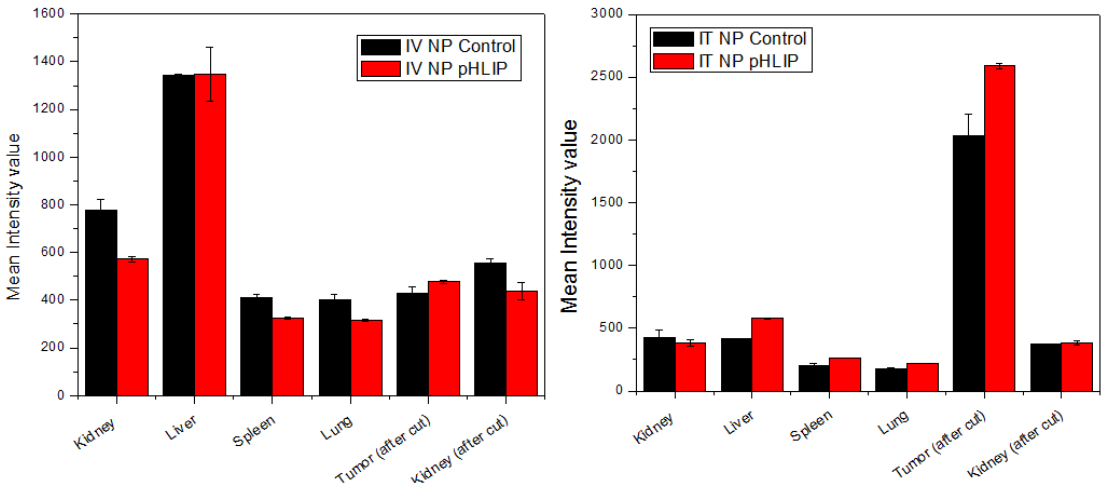

Figure 15: Biodistribution of Intra-veinous (IV) and Intra-tumoral (IT) injection of Fe_3O_4 NPs with and without pHLIP treated with 20uM Alexa$_{750}$

In these set of experiments, NP was injected based on Alexa concentration i.e. 20 uM Alexa$_{750}$ per mice. The pHLIP concentration is very low, so there is a little difference between NP control and NP pHLIP. Another reason was speculated that the pHLIP

peptide inserted into the PEG layer and not on the surface of the micelle like structure. The formation of protein corona is likely to hinder the effectiveness of the peptide.

IT injected mice have higher uptake in tumor than compared to the IV injected mice after 24 hr. Another important aspect to note is that, PEG-phospholipid coating caused fewer uptakes of NPs in liver and spleen.

Fe_3O_4 NPs were functionalized with ALexa 750 dye which can be used in near infrared imaging (NIR). The Fe_3O_4NPs were injected based on the Alexa 750 concentration, 20uM. After 24 hr, NIR imaging were taken of individual organs. As observed from the two graphs in Figure 15: Biodistribution of Intra-veinous (IV) and Intra-tumoral (IT) injection of Fe_3O_4 NPs with and without pHLIP treated with 20uM $Alexa_{750}$ tumor intensity is five times more in the mice with IT injection. This is expected as we don't see the nanoparticles were injected directly to the tumor. This means, a lot of nanoparticles were not washed away from the tumor, even after 24 hr time period.

Even with IV injection, significant amount of NPs retained in tumor after 24 hr. This is significant for the contrast generation using MRI or for drug delivery. While, there is some unwanted uptake in kidney and liver it is significantly lower than the systemic toxicity and better than a lot of other formulations. There is a small difference in uptake between control and pHLIP NPs. With improvement in number of pHLIP the targeting can be increased significantly.

2.8 Discussion:

Colloidal stability of SPIONs is controlled by three principal forces: magnetic, Van der Walls and hydrophobic-hydrophilic. In general, nanometer size particles aggregate in

suspension due to the attractive van der Waals forces in order to minimise the total surface or interfacial energy [51]. Furthermore, due to magnetic dipole-dipole interactions, nanoparticles magnetize neighboring nanoparticles. The external magnetic field further increases the aggregation. This aggregation can change the efficacy of SPIONs in drug delivery and diagnostics purposes. It is very important to stabilize SPIONs in suspension of not only water but biological medium as well.

Hydrodyamic sizes of NPs using Dynamic Light Scattering showed the higher stability and repeatability of the nanoparticle formulations tested from different batches. According to the table 1, the hydrodynamic sizes were similar from batch to batch, even with slight changes in the NP, lipid concentration and pHLIP concentration.

Coating of liposomes, as well as other nanocarriers with PEG polymer is a key for nanocarrier's stability in vivo. The configuration of PEG polymer on the surface of nanocarriers depends on the amount of polymer on the surface [52]. During the experiments it was observed that the smaller percentage of DSPE-PEG-COOH would not be sufficient enough to stabilize nanoparticles for a long term. In further experiments, 95% DSPE-PEG-COOH was used in 3.5X by weight of oleylamine/oleic acid coated Fe_3O_4 nanoparticles.

There are some controversial reports SPIONs showing toxicity [51, 53]. However, our SPIONs-PEG-COOH treated M4A4 carcinoma cells incubated for 24 hr in various concentration did not show toxicity to the cells. The good coating with PEG-phospolipid is expected to be non-toxic to the cells.

The IT injection of NPs show significant amount of NPs in tumor which can be used for drug delivery purposes. These NPs have high retention time and could be used to monitor the therapeutic progress. The intravenous injection (IV) injection (Figure 15), we see significantly less uptake in spleen and liver. The retention time of NPs is still higher, which can be significant for diagnosis. The uptake of NPs between control and pHLIP NPs is very less. This is speculated to have been due to the protein opsonization and covering the surface with natural proteins. The concentration of pHLIP with 2-3 peptides per NP is also low and might not be the optimum level to get the desired targeting. Due to this, we re-designed the NP with higher number of peptides. This will be discussed in non-PEGylated NPs.

The *in vitro* experiments showed that our NP constructs are non-toxic. The NPs are stable in different medium and can be repeatable. The in vivo experiments showed low toxicity in vital organs and significant NPs to the tumor. Thus, our SPIONs-PEG-pHLIP serve as potential candiadate for early diagnosis of tumor using MRI.

2.9 Comparison of PEG and non-PEGylated NPs

As the less number of peptides in the previous formulation did not show effective targeting in vivo experiment, we increased number of peptides and modified the formulations with different phospholipid. The phospholipids without PEG are known to be uptaken into the cells via fusion type lipid [40]. This fusion has faster cell uptake and the cargo loaded is easily release into cytoplasm as shown in Figure 17 .

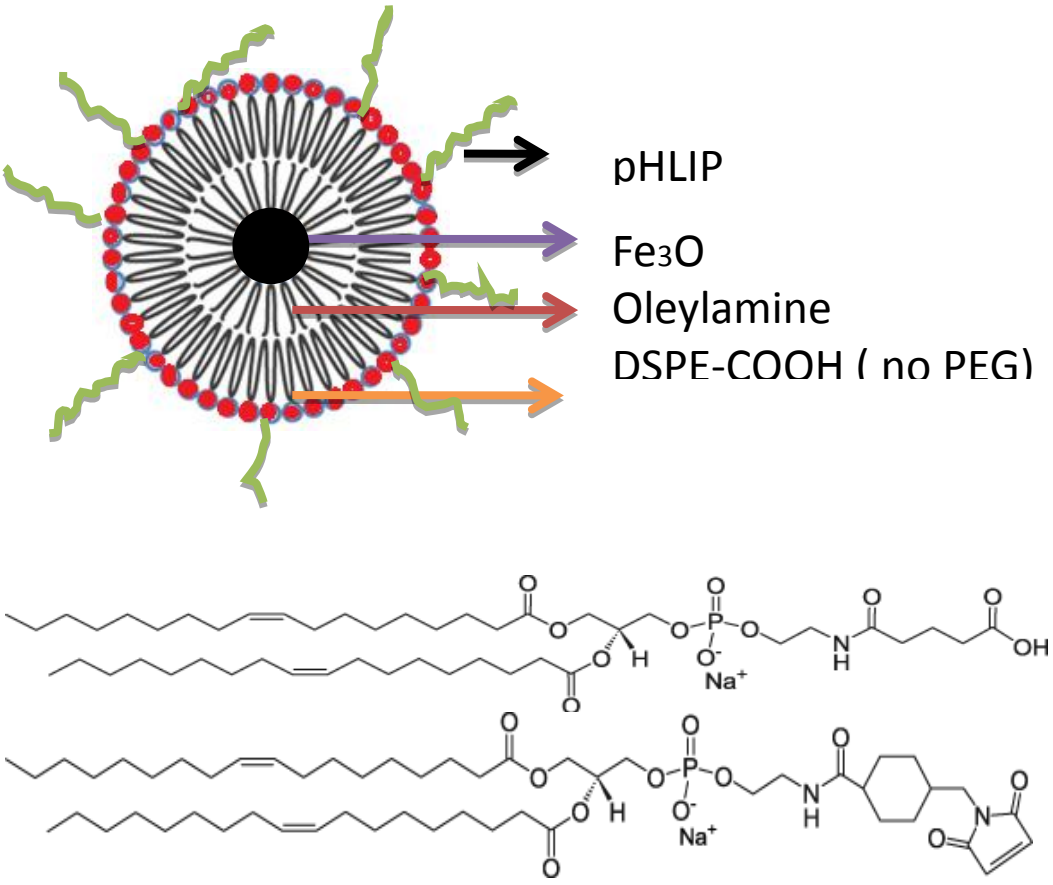

Figure 16: Schematic presentation of Fe_3O_4 NPs coating with non-PEGylated lipid and pHLIP peptide

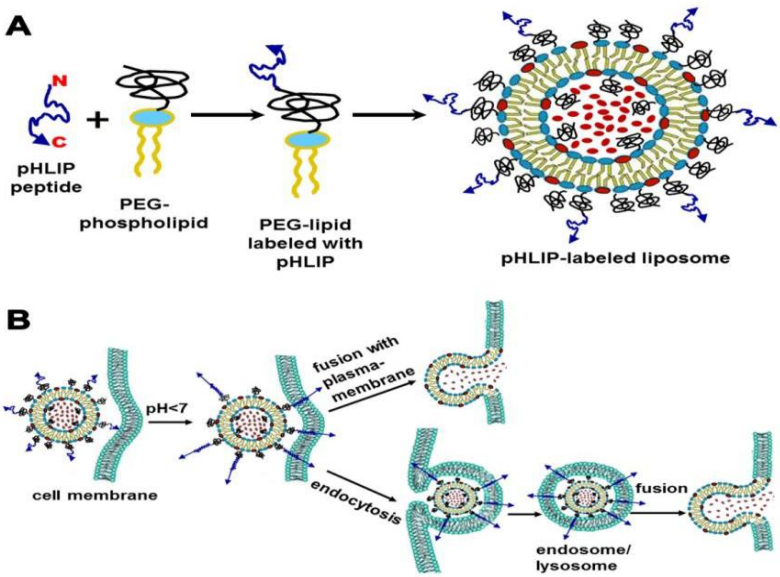

Figure 17: Schematic presentation of pHLIP/PEG coated liposomes (A) and their interaction with cellular membranes (B). The encapsulated model payload molecules and the head-groups of fluorescent lipids are shown in red. Adapted with permission from ref [40]

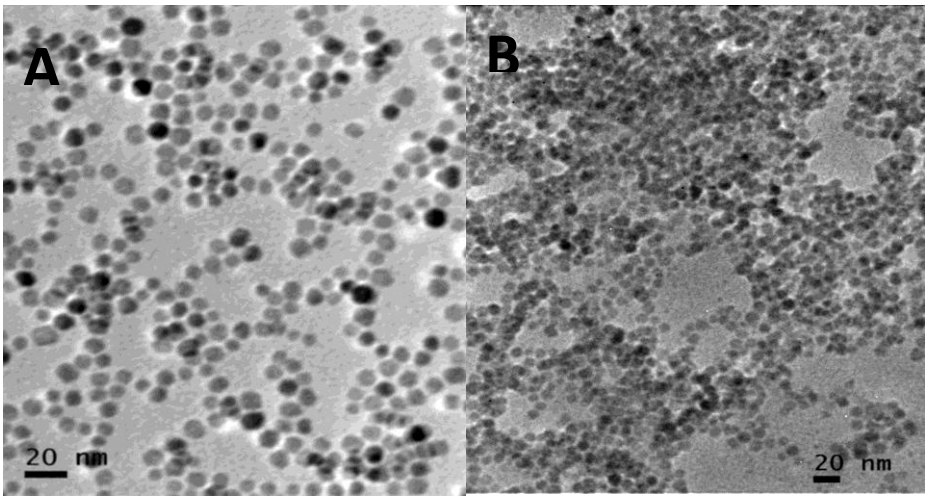

Figure 18: TEM images of A) 8nm as synthesized Fe_3O_4 NPs in hexane B) Fe_3O_4 - DSPE-COOH in water without PEG

The 8nm Fe_3O_4 NPs are stabilized in water and are monodispersed as visualized by TEM. The hydrodynamic size further showed the ligand addition and dispersion of SPIONs-pHLIP in water.

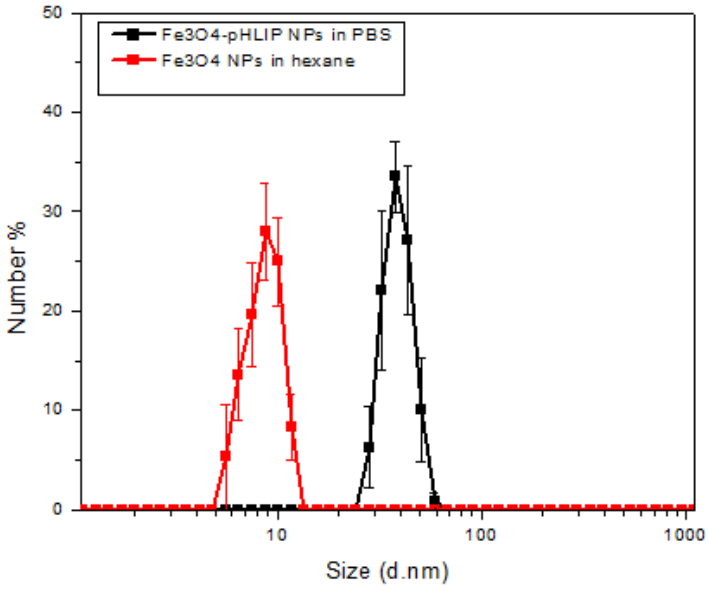

Figure 19: Hydrodynamic size of as synthesized Fe_3O_4 NPs dispersed in hexane and Fe_3O_4 NPs with pHLIP functionalization dispersed in PBS. The graph shows increase of hydrodynamic size as ligand exchange from 10nm to 30nm.

Batch	Size	Zeta Potential
1/4/13	68.06±5nm	-55mV
1/22/13	68.06±9nm	-50mV

2/4/13	68.06±10nm	-66.2mV

Table 2: Hydrodynamic size and zeta potential of as synthesized Fe_3O_4 -COOH in DI water. The size and zeta potential are consistently similar in different batches showing the repeatability of the functionalization. All the data were taken in triplicates.

The table lists the repeatablitity of the NP constructs size (68.06±5nm) and very negative zeta potential of (-50mV).

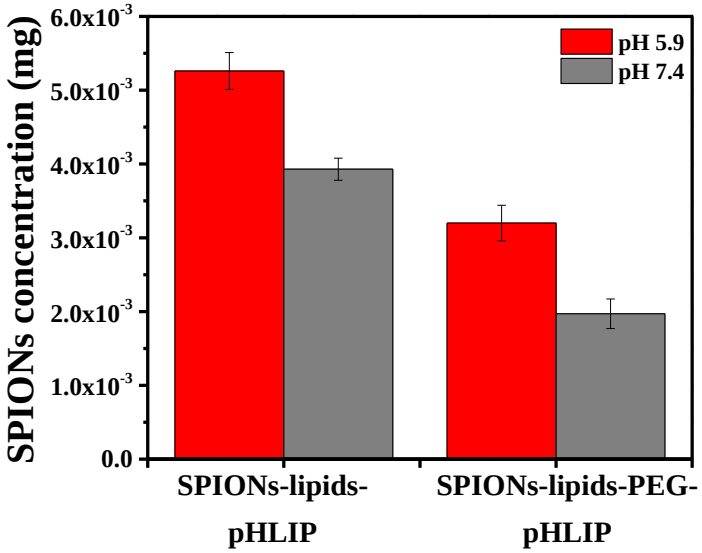

Figure 20: Cellular uptake of SPIONs-PEG-pHLIP and SPIONs-pHLIP at low and normal pH.

The optimal cellular uptake at pH 5.9, was achieved by SPIONs-pHLIP with a value of 5.26 x 10^{-3} mg of SPIONs uptaken by the cells. In contrast, SPION -PEG-pHLIP was less potent at low pH, having an uptake of 3.2 x 10^{-3} mg of SPIONs. The higher cellular

uptake can be due to the absence of PEG, which decreases the overall size of the nanoparticles and facilitates the diffusion of the nanoparticles into the cells. Both SPIONs-lipids-PEG-pHLIP and SPIONs-lipids-pHLIP revealed pH-dependence targeting.

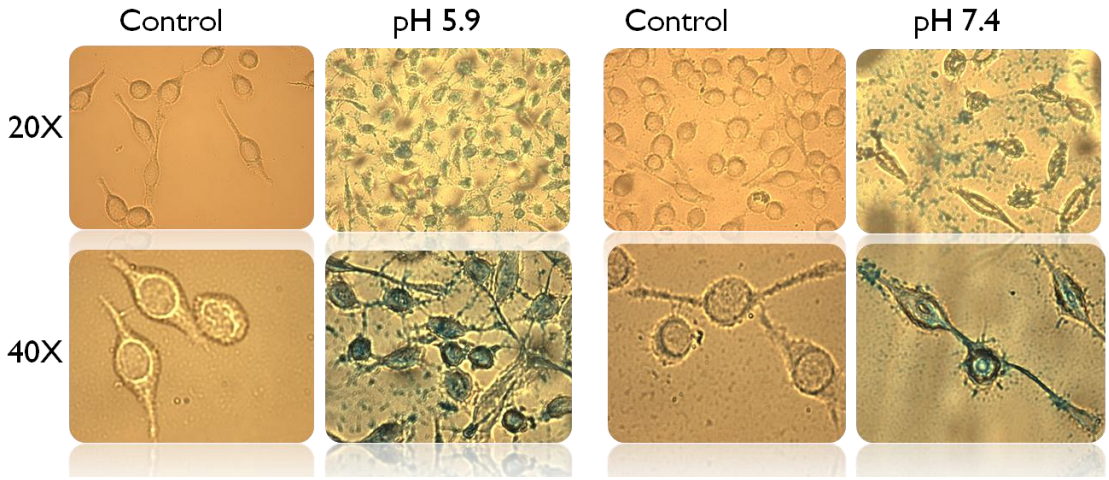

Figure 20: Distribution of SPIONs-PEG-pHLIP in cells at pH 5.9 and pH 7.4 using Prussian Blue staining. 0.05mg SPIONs treated in 105 cells in 200 µL DMEM at 37°C under 5% CO2

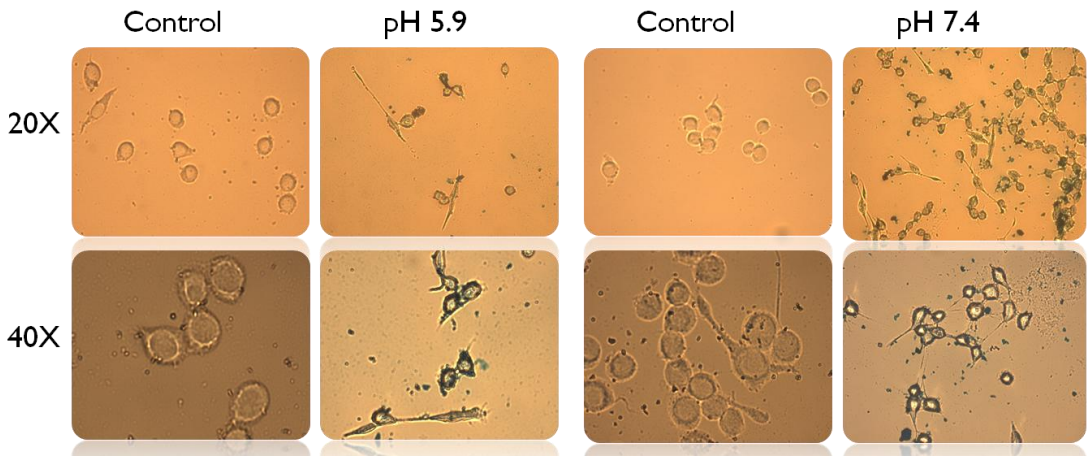

Figure 21: Distribution of SPIONs -pHLIP in cells at pH 5.9 and pH 7.4 using Prussian Blue staining. 0.05mg SPIONs treated in 105 cells in 200 µL DMEM at 37°C under 5% CO2

The blue color indicates the presence of Iron. From figure 20 and 21, SPIONs-PEG-pHLIP look more healthy than comparing to the SPIONs –pHLIP between nanoparticle treated cells and the control cells. Both the formulation were treated for 24hr. The nanoparticle uptake is definitely higher in the SPIONs –pHLIP as observed from Figure 21. The higher amount of nanoparticle is probably responsible for the visible difference in the NP treated cells. We suspected some toxicity involved in that certain batch due to instability as well. We repeated the toxicity or cell viability experiment thrice using different batches.

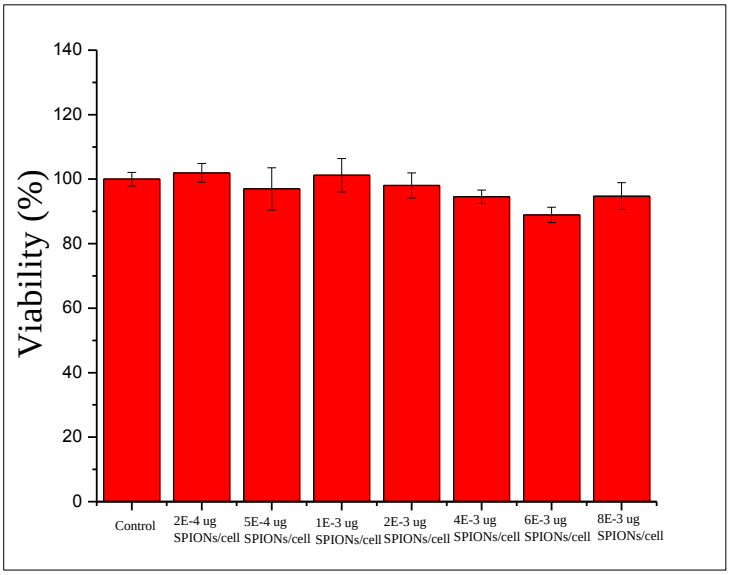

Figure 22: Viability of Cells using MTS assay treated with SPIONs -pHLIP. M4A4 carcinoma cells were plated at 40,000 cell/well different Fe concentration incubated for 72 hr

To evaluate the cytotoxicity of SPIONs-pHLIP, cell viability assay was employed in HeLa cells at different experimental concentrations. Figure 22 shows that after 72 hours of incubation with SPIONs, none of the concentrations used in the experiment exhibited significant toxicity. For higher concentration (6E-3 ug SPIONs/cell) the construct showed 5% toxicity.

Cells are 95% viable from the lowest to the highest concentration of 8E-3 ug Fe/cell. 24h and 48h incubation time also do not show any toxicity (data in supplementary figure S1).

2.10 Conclusion:

SPIONs with different phospholipids were tested for the maximum efficiency of cellular uptake and stability in biological medium. SPIONs-PEG-pHLIP and SPIONs-pHLIP were compared for the cellular uptake. While comparing the hydrodynamic sizes, SPIONs-pHLIP is around 68±5nm around 10 nm bigger than SPIONs-PEG-pHLIP in average. However, the uptake is higher in the nanoparticle formulation without PEG. The number of pHLIP peptide per nanoparticle is higher in SPIONs-pHLIP formulation thus the cellular uptake is higher as we expected at lower pH. However at normal pH, it is most likely due to the fusion type uptake which is likely due to the mechanism of cellular uptake, fusion type versus the endocytosis. Both SPIONs-COOH NPs and SPIONs-PEG-COOH NPs were nontoxic to the cells studied as measured by the MTS viability assay under different concentrations of Fe/cell.

We have used superparamagnetic iron oxide nanoparticles (SPIOs) as a delivery and a contrast agent and have coupled these SPIOs with pHLIP to demonstrate tumor targeting *in vitro* and *in vivo* while reducing kidney toxicity caused by peptide alone. These constructs are stable, reproducible and are non-toxic to cancer cells. This combination of SPIOs, pHLIP and NIR dye is superior to other constructs as they can localize in tumor and create better contrast for disease detection using Magnetic Resonance Imaging (MRI) and Near-Infrared (NIR) Flourescence Imaging.

2.11 Supplementary data:

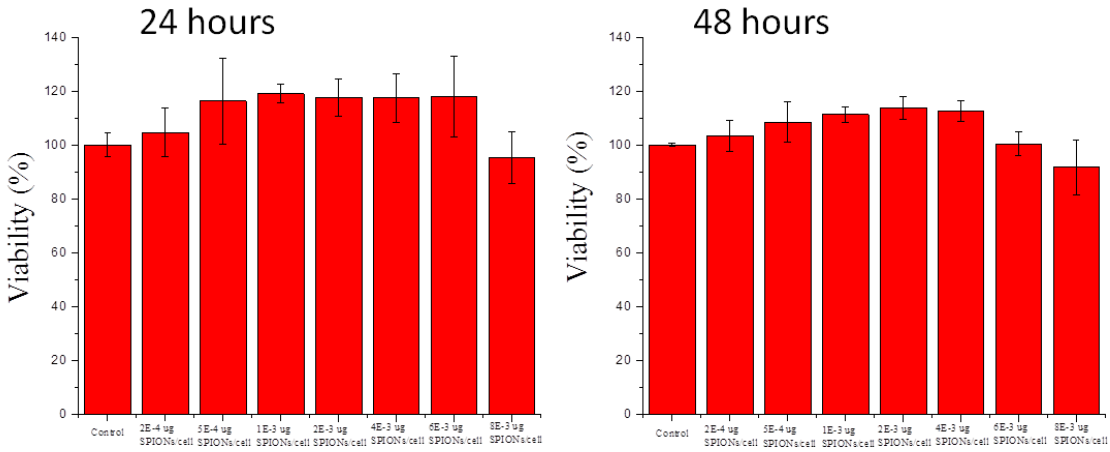

Figure 23: Viability of Cells using MTS assay treated with SPIONs -pHLIP. M4A4 carcinoma cells were plated for 24 hr,40,000 cell/well, different Fe concentration incubated for 24 and 48 hr

2.12 Non-toxicity and Ligand stability in the medium

SPIONs are used for various drug delivery and diagnosis agents. These SPIONs have been FDA approved for MRI agent due to their non-toxicity and the ability to generate contrast between normal and tumor tissues. However recently some concern has been raised on SPIONs toxicity [54]. This review paper shows some iron oxide nanoparticles synthesized via different methods and coated with dextran, polyvinyl alcohol, amine have some toxicity. But, our nanoparticles we functionalize with PEG-phospholipids, which have been used in drugs and are completely non-toxic, viability assays also confirmed that. The only reason for toxicity to be arise would be from any organic residue leftover inside the magnetoliposome formation.

Hwang et. al. used superparamagnetic iron oxide nanoparticles synthesized according to our method and functionalized with pH-sensitive amphiphilic copolymer, poly(ethylene glycol)-*b*-poly(2-(2-diisopropylamino) ethyl methacrylate (PEG_{114}-*b*-$PDPA_{120}$) forming a SPION loaded-micelle structure. At pH 5.0 and 6.2, SPION-micelles released 60 ± 2% and 11 ± 1% of total iron ions after 72 h, respectively. The released Fe amplified the ROS stress and improved the drug efficacy of β-lapachone (β-lap). β-lap, a novel anticancer drug, has shown considerable cancer specificity by selectively increasing reactive oxygen species (ROS) stress in cancer cells[53].

In our study, we want nanoparticles to be non-toxic, so I tested the Fe –release in similar conditions to the ones used by Hwang et. al however, our phospholipid coating is different.

Briefly, SPION-COOH (1mg/ml of Fe) was dialyzed in 10K MWCO dialysis tubing so that the released iron can be dialyzed. Sample were analyzed with ICP-AES for % Fe release at various time points. Even at the high temperature 45C and low pH 4.8, our SPION-Phospholipid-COOH nanoparticles did not release any iron upto 48h.

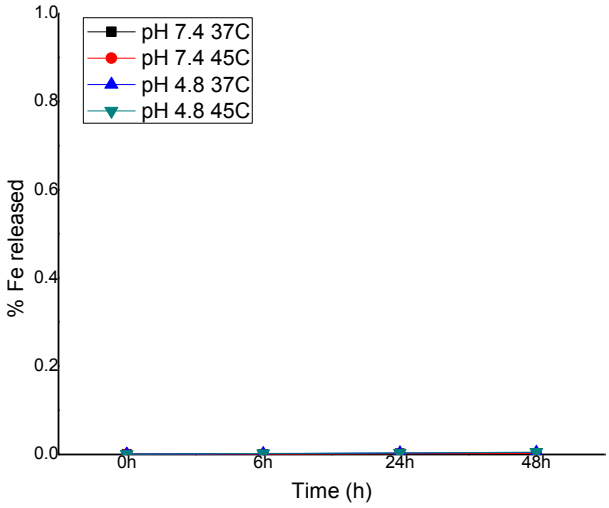

It is concluded that, our SPION- Phospholipid-COOH are robust and do not possess toxicity due to Fe release at low pH.

2.12.1 Ligand stability in the medium

During ligand addition, for SPIONs-COOH and SPIONs-pHLIP experiments some inconsistency during ligand addition would cause drastic change in SPIONs-COOH and SPIONs-pHLIP constructs size and stability. The procedure for ligand addition needs to followed exactly, slight change in the reaction time, nanoparticle concentration, volume of solvent would change in hydrodynamic size measured by DLS. We observed that during the purification step of dialysis, nanoparticles aggregate and sometimes unstable. We studied what causes such aggregation or instability.

Since, the ligand addition is based on London Dispersion forces, which is not very robust compared to the covalent bonding on ligand addition. It might be possible that the ligand easily associate and dissociate from the NP surface. As shown in Figure 24 below, nanoparticles are not individually wrapped with phospholipids but embedded in the matrix. This might be of concern, as the Fe_3O_4 NPs are coated with hydrophobic oleic acid and oleylamine and might cause some toxicity. To test the stability of phospholipid ligand in the medium during experiments.

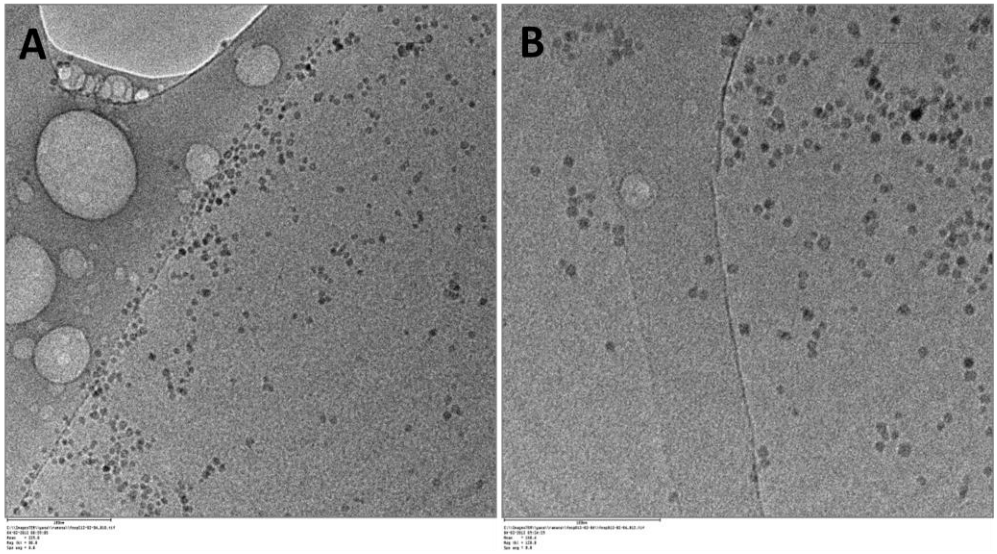

Figure 24: Cryo-TEM of Fe_3O_4 NPs in PBS. Nanoparticles are not individually wrapped with phospholipids but embedded in the matrix.

2.12.2 Experimental Design:

Optimization of ligand addition process: The amount of surfactant in the SPIONs before ligand addition needs to be consistent. More OAm/Oacid left in the solvent would cause the formation of empty liposomes. So, I modified the procedure to find the concentration of Fe on as-synthesized NPs and calculated the estimated number of Fe_3O_4 NPs based on

volume (radius) from TEM, density of Fe3O4 and weight from ICP-AES. Then, the 3.5 times, 3.7 times and 4.0 times by nanoparticle weight of phospholipids were used to study their stability. For 10 mg of NPs, total of 37 mg of mixture of phospholipids were used. It was observed that 3.7 times worked based from several experiments. Fluorescent 18:1 Liss Rhod PE was added which can be detected by fluorescence Ex/Em 557nm/571nm. SPION-Rhod-B was formed using method described below. 5% 18:1 Liss Rhod PE and 95% DSPE-PEG_{2000}-COOH were used during ligand addition.

Experiment was designed with dialysis tubing 12,000 MWCO which permits 18:1 Liss Rhod PE (MW= 1301.715) to pass through but retains the solid liposomal nanoparticles.

As shown below in Figure 26A, 1 ml of SPION-Rhod-B were put inside dialysis tube. Three different dialysis containing NPs was put in three beaker containing 100 ml PBS buffer at 37ºC and stirred for 24h, 48h and 72 h respectively. 1ml aliquots were taken from each 24h, 48h, and 72h samples for 18:1 Liss Rhod PE outside the PBS solution. The aliquots were tested for the fluorescence intensity. The SPION-Rhod-B sample inside the dialysis tubing was also tested for fluorescence intensity for comparison. The loss of fluorescence intensity inside the tubing should be equal to fluorescence gained outside.

For a positive control, as with all the fluorescent dyes it is necessary to reckon the Rhod-B naturally quenching. Samples were stored at 4 ºC for various time points as above and was used without dialysis tubing and stirring. The loss of fluorescence intensity from 0h to 24h, 48h, 72h would correspond to the natural quenching of Rhod-B schematic shown below in Figure 26B.

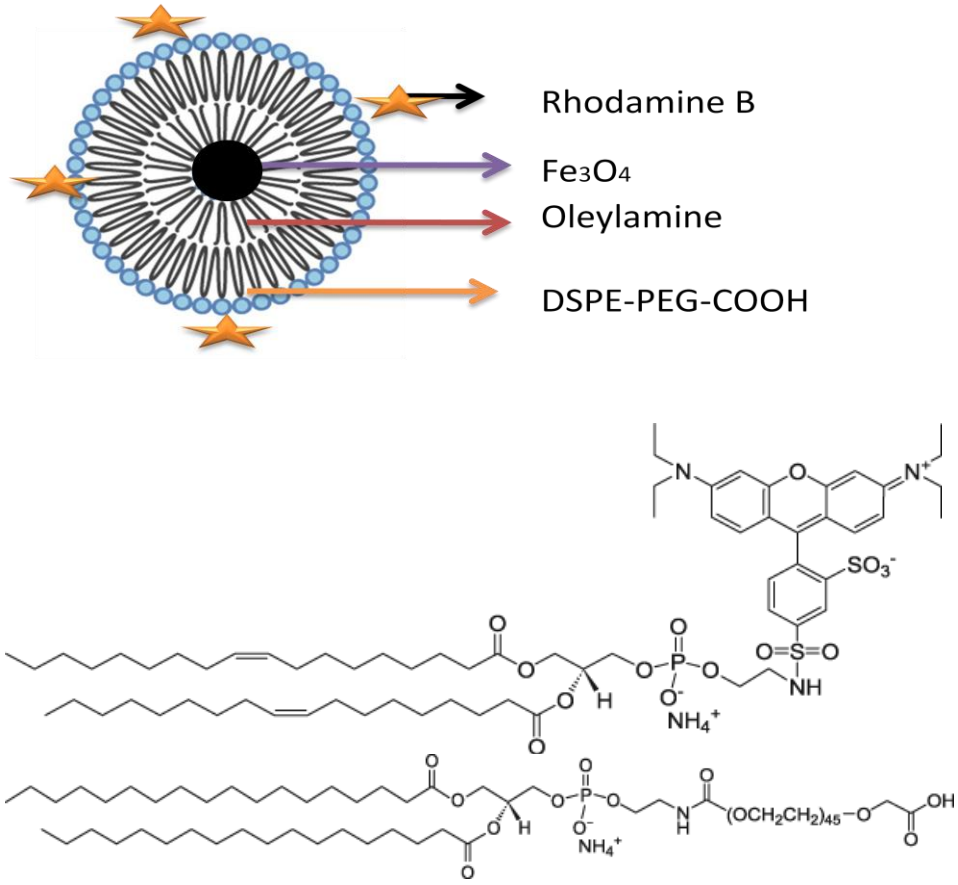

Figure 25: Schematic illustration of SPIONs-Rhod-B for ligand stability study: Structure of 18:1 Liss Rhod PE and DSPE-PEG$_{2000}$-COOH shown above

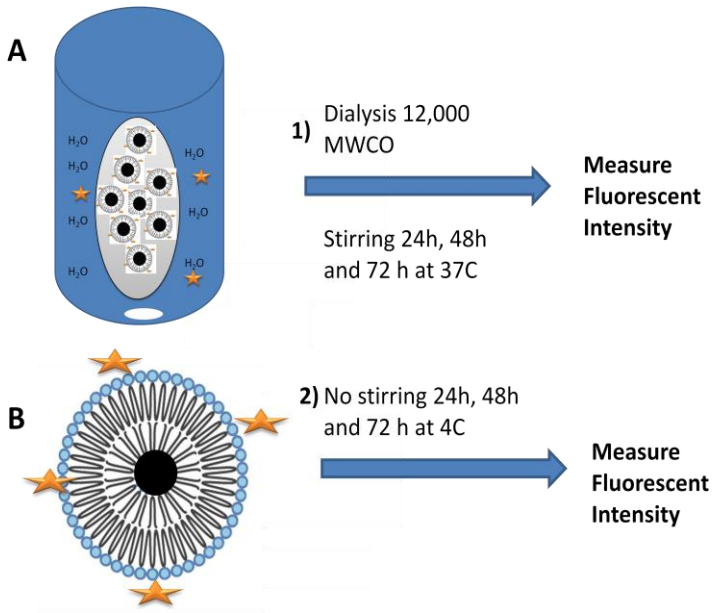

Figure 26: Schematic of experimental design to test the stability of phospholipids

2.13 Methods:

Materials:

Iron pentacarbonyl ($Fe(CO)_5$), oleylamine (70%), oleic acid (90%), 1-octadecene (ODE, 90%), 1,2,3,4-tetrahydronaphthalene (tetralin, $97%), hexane, hexadecylamine (HDA, 90%) and hydrogen chloride solution (HCl, 1 M in diethyl ether) were purchased from Sigma Aldrich and used without any further purication. Hexadecylammonium chloride (HDA.HCl) was synthesized following a published work [55].

2.13.1.1 Synthesis of bcc-Fe NPs and oxidation to Fe_3O_4 NPs:

The bcc-Fe was synthesized using slight modification from our previously published data [55],[56]. HDA.HCl (1 mmol: 280.0mg) was solubilized in 20ml of tetralin and 1 mL of

oleylamine (OAm) under a gentle flow of Nitrogen gas. The mixture was heated to 120 ºC and kept at this temperature for 30 min to generate a colorless solution. Under Nitrogen blanket, the solution was heated to 180 ºC and 0.5 mL of iron pentacarbonyl ($Fe(CO)_5$, 3.5 mmol) was injected into the solution. The color of the solution changed to yellow–brown–dark brown–black in 8 min. The temperature was kept at 180 C for 30 min then cooled down to room temperature. NPs were precipitated by 50 ml isopropanol, followed by centrifugation (8500 rpm, 8 min). The NPs were further purified by dispersing into hexane (20 mL) and precipitating on 50 ml ethanol for the second time followed by centrifugation (8500 rpm, 8 min). The as-synthesized Fe NPs were dispersed in hexane. NPs were characterized by TEM. For Fe_3O_4 NPs, bcc-Fe were further oxidized in air for 1h at 300 C. XRD pattern were confirmed for Fe_3O_4 peaks.

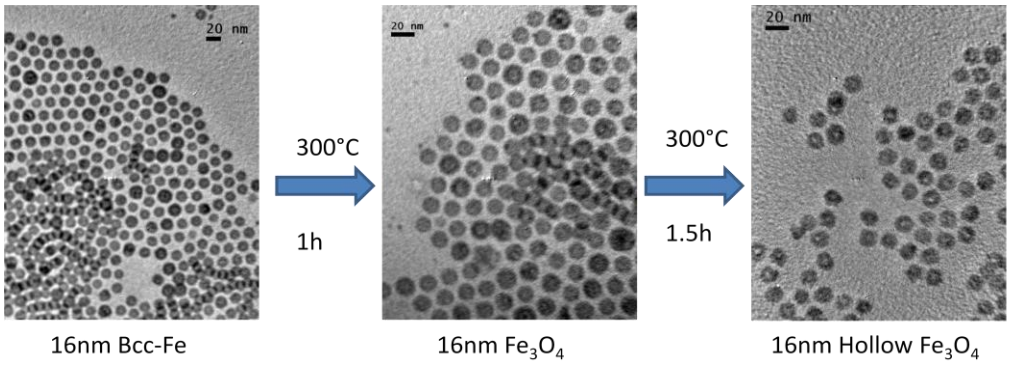

Figure 27: Controlled oxidation of bcc-Fe to receive 16nm Fe_3O_4 nanoparticles. If oxidized for longer time the nanoparticles become hollow iron oxide nanoparticles.

2.13.1.2 Formation of SPION-Rhod-B

All the lipids were purchased from Avanti Polar lipids and stored at -20 C. Briefly, 10mg of Fe_3O_4 NPs oxidized from bcc-Fe NPs and characterized with TEM was dried and weighed in a vial. 2 ml of chloroform was added to dissolve the NPs. Phospholipid with

Rhodamine B, 0.5ml of (1mg/ml) of 18:1 Liss Rhod PE (Avanti Polar Lipids) was added to the NP-choroform solution. After mixing for 15 min, 1.5 ml of 880125 (25mg/ml) DSPE-PEG-COOH (Avanti Polar Lipids) was added to the above mixture. The vial was wrapped in aluminum foil to avoid light exposure. Mixture stirred at RT for 30 min. Rotovap was performed for 2 hr to get rid of organic solvent and then dissolved in DI water. The NP-Rhod-B solution was dialyzed for 24 hours in DI water with change in water 2X. NP-Rhod-B was further purified using PD-10 desalting column. The column wash was collected to measure the fluorescence content of unbound Rhod-B ligand. Finally, NPs were filtered with 0.22um, PVDF membrane. Elemental analysis using ICP-AES (JY2000 Ultrace ICP Atomic Emission Spectrometer) and UV-vis and Fluorescent Spectroscopy were used for concentration.

2.13.2 Characterization:

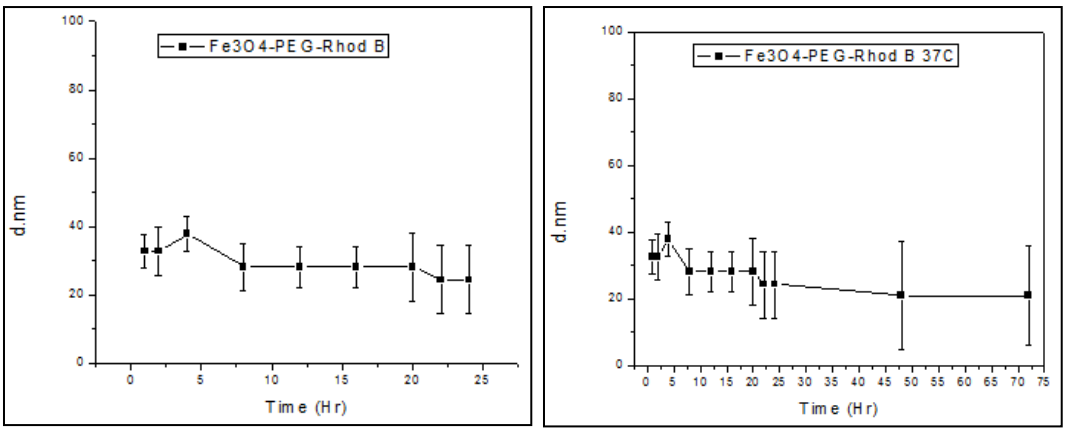

Figure 28: Hydrodynamic size of Fe_3O_4 NPs in water, incubated at 37 ºC at 0.116 mg/ml of Fe from ICP-AES. After 15 hours, hydrodynamic size fluctuates with larger std. dev.

To test the stability at the biological conditions, hydrodynamic size of Fe_3O_4 NPs in water (0.116 mg/ml of Fe from ICP-AES) NPs incubated at 37C and data taken at various time point. As shown in Figure 28, Fe_3O_4 nanoparticles are stable upto 24 hours with <5 std. dev. after which the std. dev. is increased and the particles are polydisperse ranging from 10nm- 50nm.

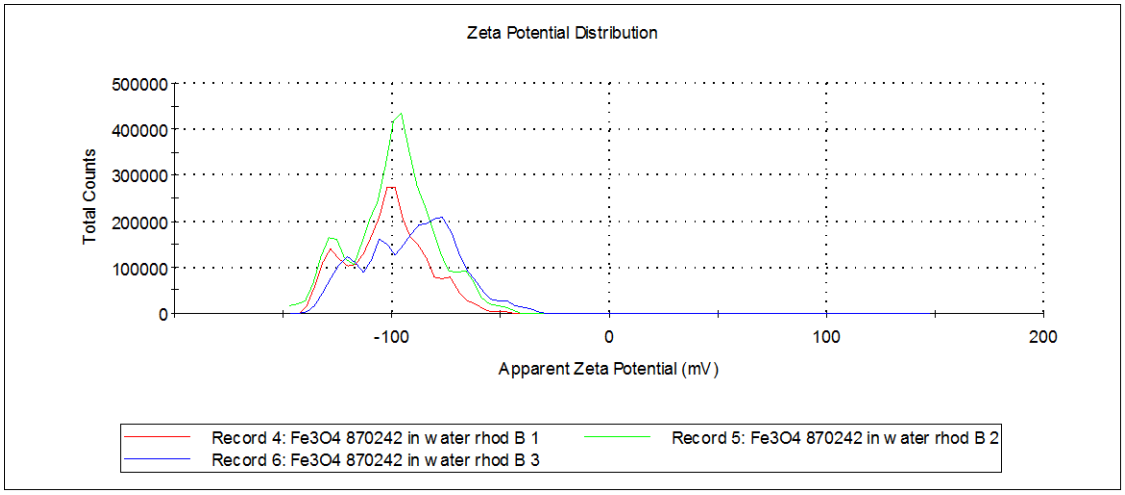

Figure 29: Zeta Potential of Fe_3O_4 NPs functionalized with Rhodamine-B phospholipid -99.2±2 mV

Initially, SPIONs-Rhod B in water showed 30nm hydrodynamic size and zeta potential of -99.2±2 mV, the more negative the value the more stable is the compound, suggesting a very stable system stored at 4C.

2.14 Result and Discussion:

After preparation, purification and characterization SPIONs-Rhod B were tested for the ligand stability during dialysis at 37ºC, 1 ml of (0.58mg/ml Fe conc.) SPION-Rhod-B were put inside dialysis tube. Dialysis tube was put in three beakers each containing 100 ml PBS buffer at 37ºC and stirred for 24h, 48h and 72 h respectively. 1ml aliquots were

taken from each 24h, 48h, and 72h samples for 18:1 Liss Rhod PE outside the PBS solution. The aliquots were tested for the fluorescence intensity. The SPION-Rhod-B sample inside the dialysis tubing was also tested for fluorescence intensity for comparison. The loss of fluorescence intensity inside the tubing should be equal to fluorescence gained outside. On day 4, 42% of Rhod-B loss was recorded on the inside and 31% loss on the outside of beaker.

For a positive control, as Rhod-B quenches naturally at 37 ºC, similar formation as above was used without dialysis tubing and stirring. The loss of fluorescence intensity in this formulation would correspond to the natural quenching of Rhod-B. 26% release is due to natural quenching of Rhodamine B over 4 days calculated from control NPs kept at 37 ºC and fluorescence intensity read at each 24h, 48h, and 72h samples.

Standard curve of Rhod-B was generated by dissolving Rhod-B peptide in water solution for the base line and concentration of Rhod-B calculation. After considering the natural quenching, in total 16% of Rhod B is released into the PBS buffer at 72 hr. At 24hr, negligible amount of Rhod-B was released into the beaker after normalizing the data. However, after 24 hr SPION-Rhod-B constructs show 12% of Rhod B release. The exchange of ligand is probably responsible for the instability of NPs during dialysis and at 37ºC. This is kind of expected as the nanoparticles themselves aggregate during such harsh conditions due to the high magnetic moment of Fe_3O_4 NPs. However, without the dialysis and stirring, these constructs are stable for a long time.

2.15 Conclusion:

Zeta-potential and chemical properties of the nanoparticle surface determine the interactions in biological media with proteins, enzymes, cell receptors and cellular protrusions. It is very important to have stable nanoparticles to receive good interaction, better delivery and longer retention time. The volume of solvent, concentration of NP, amount of surfactant in the NP changes the formation of magnetoliposomes. One must be careful in each step of the ligand addition. Our SPION-Phospholipids construct are non-toxic and are robust with good stability.

Chapter 3 Au- Fe_3O_4 NPs for Targeted Therapeutic and Diagnostics

3.1 Introduction:

Theranostic nanotechnology, the combination of diagnosis and therapy into one entity, holds great promise for simultaneous cancer diagnosis, targeted drug delivery, and monitoring of therapeutic response [57]. The combination of diagnosis with therapy facilitates monitoring of distribution, localization, release of a chemotherapy drug and therapeutic response. Theranostic NPs usually consist of a NP core with optical or magnetic properties for imaging, and modifiable surfaces for linking targeting ligands and therapeutic drug loading. Gold (Au) and iron oxide (Fe_3O_4) are frequently used as surface materials because they are biocompatible, easily modified and visible using non-invasive techniques [58, 59].

Au- Fe_3O_4 dumbbell like NPs provides a multifunctional platform for therapeutic and diagnostics. Au-Fe_3O_4 NPs are very unique as they have both optical as well as magnetic properties arising from gold and iron oxide respectively. Gold NPs is very well known for its unique optical property, biocompatibility, stability, and thiol chemistry. Gold NPs can be used in optical imaging such as X-ray computed tomography (X-ray CT), and Positron emission tomography (PET) diagnostics [60]. As 3-14 nm Au- Fe_3O_4 has magnetization of 80 emu g^{-1} in comparison with Fe_3O_4 has ~75 emu g^{-1} these can be used in MRI as well [61]. These Au- Fe_3O_4 dumbbell nanoparticles when loaded with drugs and functionalized with targeting agent on the surface can be a very unique targeted therapeutic and diagnostic agent, termed recently known as theranostic agents. However, targeting is very important to get the effective doses in the diseased area to get an early diagnosis.

(i) 20 nm Fe_3O_4

(ii) 3-20nm Au-Fe_3O_4

(iii) 8-20nm Au-Fe_3O_4

(iv) A431 cells 8-20nm Au-Fe_3O_4

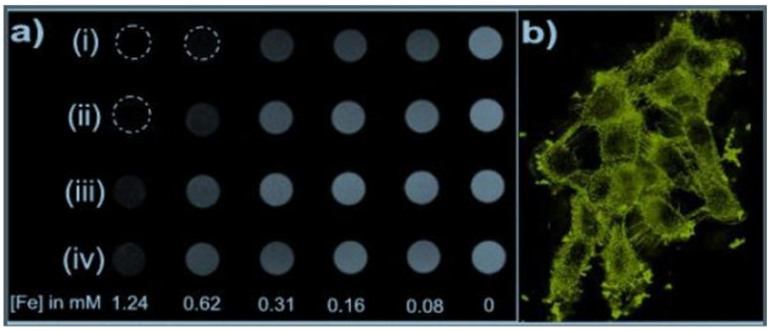

Figure 30: T2-weighted MRI of (i) 20 nm Fe_3O_4, (ii) 3 nm - 20 nm Au- Fe_3O_4 , (iii) 8 nm - 20 nm Au- Fe_3O_4NPs, and (iv) A431 cells labeled with 8 nm - 20 nm Au- Fe_3O_4 NPs. (C) Reflection image of the 8 nm - 20 nm Au- Fe_3O_4 labeled A431 cells. Adapted with permission from reference[21].

This study demonstrated the magnetic and optical property of Au- Fe_3O_4 NPs to diagnose cancer cells. Au- Fe_3O_4 NPs were functionalized with epidermal growth factor receptor antibody (EGFRA), which targets the epidermal growth factor receptor overexressed in A431 human epithelial carcinoma. The T_2 relaxation property of 8–20-nm Au– Fe_3O_4 NPs with r_2 = 80.4 mM-1•s^{-1} is very comparable to the benchmark 20nm Fe_3O_4 NPs with r_2= 121.13 mM-1•s^{-1} (Figure 30). A431 cells labeled with 8–20nm Au– Fe_3O_4 -EGFRA NPs can also be visualized with a scanning confocal microscope at 594 nm. The signal detected is from the Au NPs in the Au- Fe_3O_4 structure and reflects the typical morphology of the epithelial cells [21]. The study further showed the combination of diagnosis and targeting.

Targeted drug delivery helps in cutting down therapeutic doses by concentrating the cargo in the diseased area, tackling MDR and reducing side toxicity. As previously

discussed on chapter 2, tumor has a low extracellular pH environment which can be used to target using pH low insertion peptide (pHLIP). We planned to take advantage of this biomarker of tumor for targeting using pHLIP peptide unique properties of Au and Fe_3O_4 to make a nanoparticle based targeted therapeutic agent. In this study, we focused on studying the targeting ability of Au- Fe_3O_4 -pHLIP NPs to tumor so it can be used for diagnosis.

3.2 Methods:

1) Synthesis of 6 nm Gold Nanoparticles (AuNPs):

In a typical synthesis of 6 nm Au NPs, 0.1 g of $HAuCl_4.3H_2O$ precursor was dissolved in a solution of tetralin (10 mL), and Oleylamine (10mL) at room temperature and stirred under N_2 flow for 10 min. A reducing solution containing 0.5 mmol of tertbutyl amineborane , tetralin (1 mL), and Oleymanine (1 mL) was mixed by sonication and injected into the precursor solution. The color changed to dark instantaneously. The mixture was allowed to react for 2hour at RT. Then, the solution was precipitated using 60ml acetone. The Au NPs were collected by centrifugation (5500 rpm, 5 min), washed with ethanol and redispersed in hexane.

2) Synthesis of 6-20nm Au- Fe_3O_4 Dumbbell Nanoparticles:

In a typical synthesis, 10mg of AuNPs were mixed in a three-neck flask containing 1ml of Oleylamine and 20 ml of Octadecene solvent. Then, under N_2 flow the solution was stirred to 120°C for 30 min. Then, under blanket of N_2, 0.1ml of $Fe(CO)_5$ was injected at 120°C. The mixture was quickly heated to 300°C at the heating rate of 15°C/min and kept at that temperature for 30 min. The reaction was allowed to cool to RT and then,

precipitated using 80ml isopropanol. The Au-Fe_3O_4 NPs were collected by centrifugation (8500 rpm, 8 min), washed with ethanol and redispersed in 5ml hexane. A drop of NPs diluted in hexane was dried on a formbar crabon TEM grid for TEM characterization.

3) Ligand Exchange: *Modification of NPs with Dopamine-PEG $_{2000}$-COOH*:

40mg or 60mg of *O,O'*-Bis[2-(succinylamino)ethyl]polyethylene glycol (PEG_{2000} diacid or PEG_{3000}diacid) (Sigma-Aldrich) was dissolved in 2 ml chloroform. 4 mg of 1-ethyl-3-(3-dimethylaminopropyl) carbodiimide hydrochloride (EDC) and 2 mg of N-Hydroxysuccinimide (NHS) were added into the solution and stirred for 30 min. Then, 4 mg of dopamine was added and the mixture was stirred for 2 h. Finally, 10 mg NPs in 1 ml chloroform was added into the mixture. After shaking 24 h, the product was precipitated by 10 ml hexane and dispersed in DI water. Particles were dialysed in 100K dialysis tubing for 24 hr with change in DI water twice. The nanoparticles were passed through Sephadex PD-10 desalting column to change the medium to PBS as well as to get rid of salts. Finally, they were filtered through 0.22um sterile filter.

4) Cell lines and Cell culture

Human cervical cancer cells (HeLa), Panc-1 human pancreatic carcinoma and MCF-7 breast cancer cells were used for NP experiments. All the cell lines were obtained from the ATCC. Cells were grown at 37°C in 5% CO_2 in DMEM medium supplemented with 10% fetal bovine serum and 1% penicillin/streptomycin. Cells were passed every 3 to 4 days depending on their growth rate.

5) Cell uptake experiment

Cell uptake experiment was done using Panc-1 human pancreatic carcinoma and MCF-7 breast cancer cells. Cells were grown in sterile T_{25} plates until 80% confluency. Then, cells were treated with sterile Au-Fe_3O_4-pHLIP NP concentration of 50ug Fe/ml for 24 hr. After, 24 hr cells were washed 3X with PBS 1X. Then, trypsinized and cells were centrifuged to get rid of supernatant and extra NPs. After that, cells were digested using 2ml nitric acid under getle heat and 1ml hydrogen peroxide. Then, Fe particles were dissolved in aqua regia for the ICP-AES to measure Fe uptake into cells.

6) Sample preparation for TEM

NP uptake and intra-cellular localization was determined using trans-emission microscopy (TEM). Breast cancer cells were grown to ~80% confluence and Au-Fe3O4-pHLIP (50ug/ml) added to the media. After 4h incubation, cells were washed with PBS and fixed with 2.5% glutaraldehyde in 100mM sodium cacodylate buffer (SCB), pH 7.4 (Sigma-Aldrich, St. Louis, MO). The fixative solution was then replaced with 1%BSA/SCB buffer. Cells were harvested and fixed with 1% osmium tetroxide/ SCB for 1h at room temperature followed by alcohol dehydration. Cell pellets were embedded in fresh resin and placed in an oven at 70 ºC for 11h. Semi thin sections were cut and analyzed with a Philips EM 420 (120kV) microscope.

7) *In vivo* experiment:

Primary tumors were established by subcutaneous injection of Hela cancer cells (10^6 cells/flank/0.1 mL) of adult athymic nude mice (from Harlan, Inc). Tumor was allowed to grow until 2-3 weeks, tumor size ~5-8mm. Tail vein injection of NPs at the conc. of 7mg

of Fe/ kg of mouse (or 1 mg/kg fluorescent pHLIP) (100ul) is done. Then, imaging whether NIR or MRI can be performed at 6hr, 12hr, 24hr time points. After that, mouse was sacrificed to collect tumors and organs for bio-distribution and TEM of Fe present in the organs. Control mice with tumor but no nanoparticle, were sacrificed for natural Fe concentration in tumor and organs. Organs are digested using nitric acid, hydrogen peroxide, followed by aqua regia. Then sample is analyzed via inductively coupled plasma atomic emission spectrometry (ICP-AES). For TEM, fresh samples can be fixed using 2.5% glutaraldehyde and further processed.

3.3 Results:

3.3.1 Nanoparticles Synthesis and Functionalization

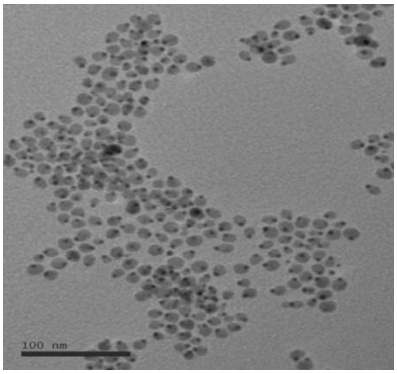

Figure 31: TEM image of Au-Fe_3O_4-Dop-PEG2000-COOH in water

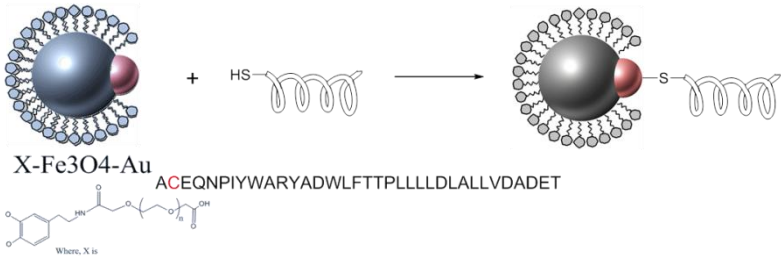

Figure 32: Schematic illustration of the surface functionalization of the Au-Fe_3O_4 NPs. Ligand exchange was performed using Dopamine-PEG_{2000}-COOH polymer on the Au-Fe_3O_4 surface and then pHLIP was conjugated to Au surface using Au-thiol chemistry

Au-Fe_3O_4 NPs were synthesized using previously published method [19]. pHLIP peptide was covalently attached to Au surface of Au- Fe_3O_4 NPs coated with Dop-PEG_{2000}-diacid. These particles were stable in 1X PBS buffer for 48h, DLS measurement shown in figure below.

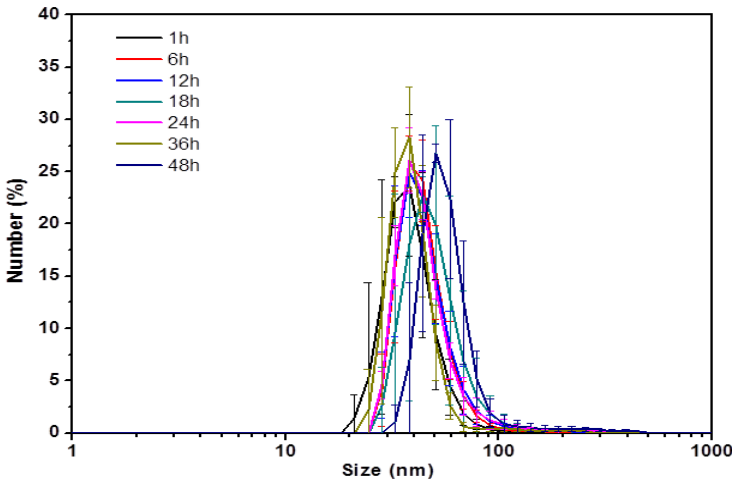

Figure 33: Stability from 1 h to of Au-Fe_3O_4–pHLIP constructs in PBS 1X 48 h

The as-synthesized Au-Fe_3O_4 NPs modified with Dop-PEG_{2000}-COOH are stable in PBS at 37C. Hydrodynamic size for upto 48h show the NPs are stable and did not cause aggregation.

3.3.2 In vitro experiment:

To test the pHLIP peptides targeting ability to tumor cells cellular uptake experiment was carried out using Mcf 7 breast cancer cell line and Panc 1 human pancreatic carcinoma. The Au-Fe_3O_4 -pHLIP particles were treated for 4h at low pH and normal pH at particle concentration of 50ug Fe/ml. As shown in the figure below, higher uptake of particles were seen in low pH compared to normal pH. TEM images of NPs show the intact cell with Au-Fe_3O_4 localized in endosomes and in the cell membrane.

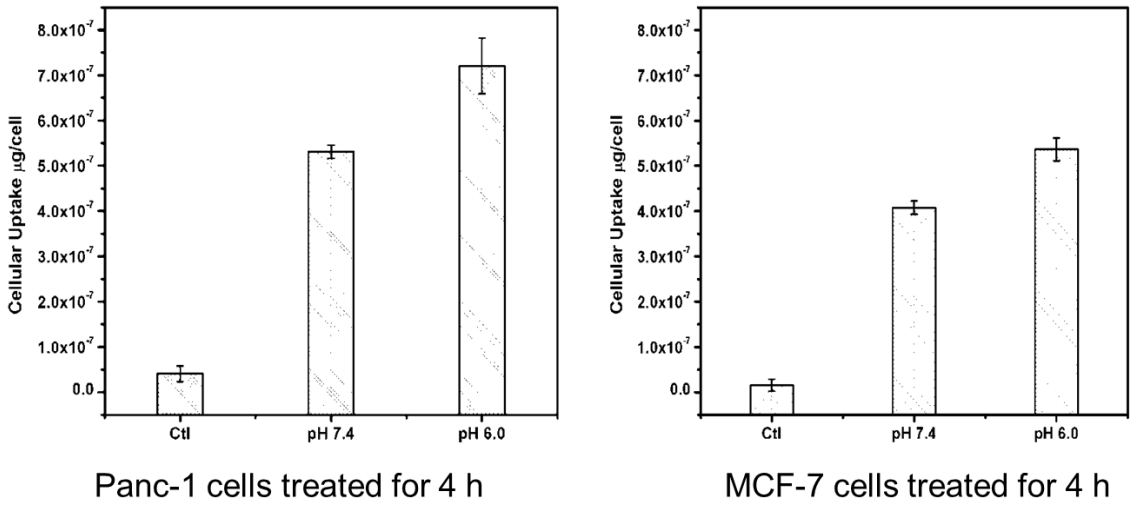

Figure 34: Cellular uptake of Au-Fe_3O_4 -pHLIP particles treated for 4h at low pH and normal pH in Panc-1 and MCF-7 cell lines. Higher uptake of nanoparticles at low pH showing the pHLIP targeting

3.3.3 In vivo experiment:

After, the successful uptake *in vitro* experiment, we carried out *in vitro* experiment. HeLa cancer cells were subcutaneously injected into the right flank of immune-compromised nude mouse and let the tumor grow for 2-3 weeks. Mice were tail vein injected with Au-Fe_3O_4-pHLIP nanoparticles at the concentration of 7mg of Fe/ kg of mouse. After 24 hr, ICP-AES was performed to see the biodistribution of Au nanoparticles, details in supplementary information. From the figure 10, we observed many NPs in liver and spleen. The uptake was similar between control Au- Fe_3O_4 NPs and with Au- Fe_3O_4-pHLIP NPs. The uptake of Au- Fe_3O_4-pHLIP were similar in tumor uptake, however a slight decrease in liver uptake was shown, which could reduce the liver toxicity. TEM image shows nanoparticle uptake in liver and spleen. Interestingly, nanoparticles were intact in liver whereas degraded in spleen. Spleen recycles RBC's and iron in the body, and one can reason this is the reason for degradation. However spleen's pH is of 7.2 and intrasplenic pH is of 6.8 which is not enough to digest particles [62]. Understanding degradation in spleen could be an interesting project in itself.

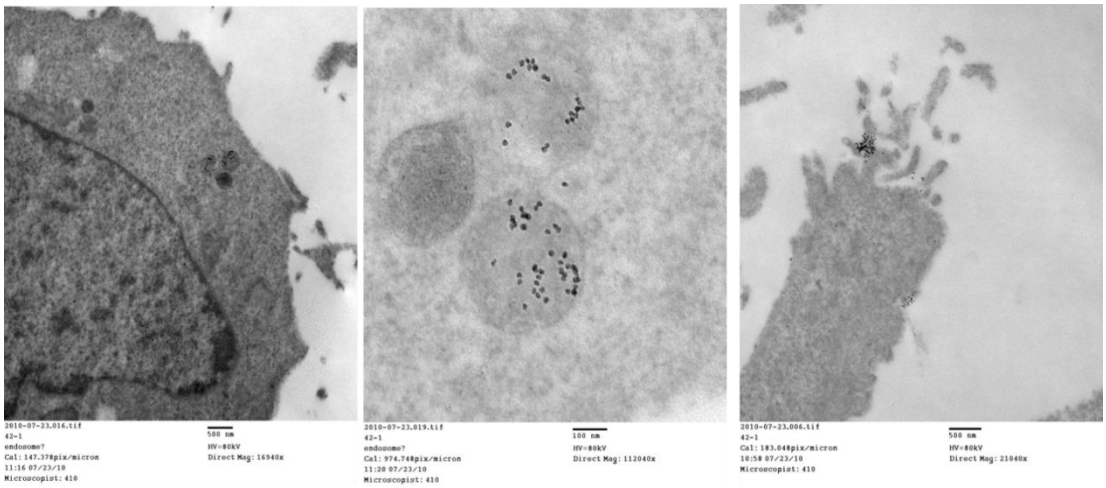

Figure 35: Hela cells treated with Au-Fe_3O_4 -pHLIP for 42 h treated at 50ug/ml. Nanoparticles are observed inside the endosomes (dark spots)

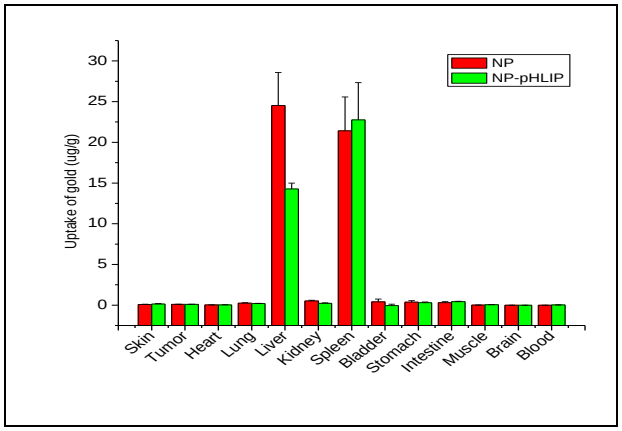

Figure 36: Biodistribution of Au- Fe_3O_4 nanoparticles in red and Au- Fe_3O_4-pHLIP nanoparticles in green after 24hr of NP treatment.

After, the successful uptake *in vitro* experiment, we carried out *in vivo* experiment. HeLa cancer cells were subcutaneously injected into the right flank of immune-compromised nude mouse and let the tumor grow for 2-3 weeks. Mice were tail vein injected with Au-

Fe_3O_4-pHLIP nanoparticles at the concentration of 7mg of Fe/ kg of mouse. After 24 hr, ICP-AES was performed to see the biodistribution of Au nanoparticles, Figure 36. Au is foreign to the body so it makes a good control for biodistribution. We see very little uptake of NPs in tumor compared to other liver and spleen, however, TEM shows the NPs are uptaken into the vasculature of tumor.

We observed many NPs in liver and spleen as a result of NP clearance and side-uptake, Figure 38. The uptake was similar between control Au-Fe_3O_4 NPs and with Au-Fe_3O_4 - pHLIP NPs. pHLIP peptide showed slightly higher tumor uptake, but slight decrease in liver uptake which is a plus. TEM image showed high amount of nanoparticle uptake in liver and spleen. Interestingly, nanoparticles were intact in liver whereas degraded in spleen. Spleen recycles RBC's and iron in the body, and one can reason this is the reason for degradation. However spleen's pH is of 7.2 and intrasplenic pH is of 6.8 which is not enough to digest particles [62]. Understanding degradation of NPs in spleen could be an interesting project in itself. This means the NPs are biodegradable and bioeliminable and the iron can be re-used by the cells.

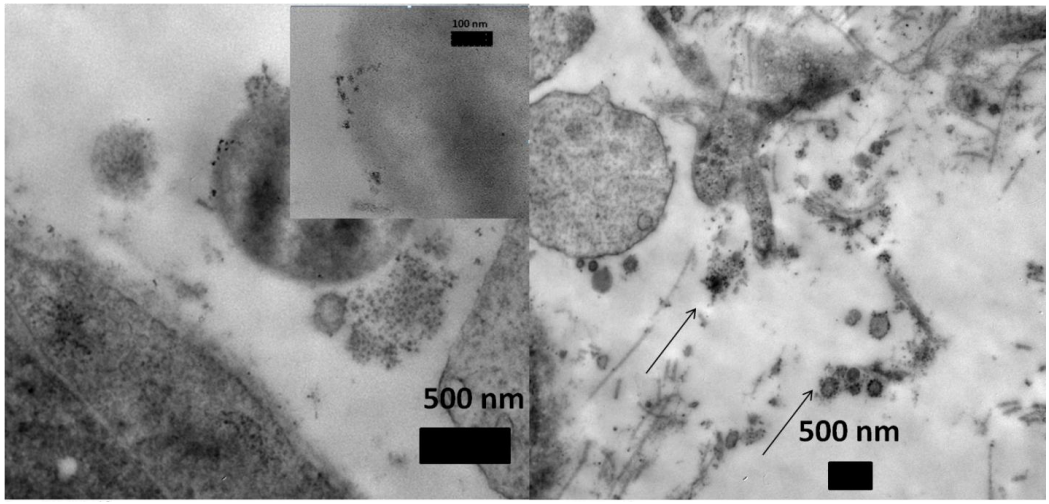

Figure 37: TEM image of tumor treated with NP-pHLIP treated. Dark areas show the NP uptake.

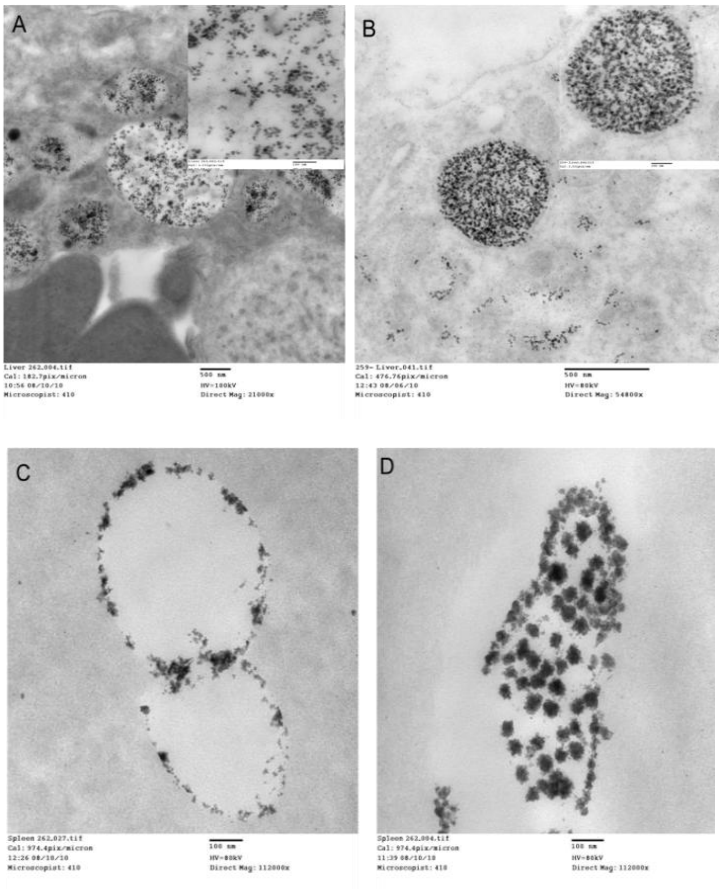

Figure 38: TEM image of liver Kupffer cells, A) NP-pHLIP treated B) NP control C and D) Spleen, Degradation of NPs seen in spleen

3.4 Discussion:

Au- Fe_3O_4 dumbbell like NPs provides a multifunctional platform for therapeutic and diagnostics. Au- Fe_3O_4NPs are very unique as they have both optical as well as magnetic properties arising from gold and iron oxide respectively. Gold NPs is very well known for its unique optical property, biocompatibility, stability, and thiol chemistry. Gold NPs can be used in X-ray computed tomography (X-ray CT) ACS and Positron emission tomography (PET) diagnostics due to the Surface Plasmon Resonance (SPR) [60]. As 3-14 nm Au- Fe_3O_4 has magnetization of 80 emu g^{-1} in comparison with Fe_3O_4 has ~75 emu g^{-1} these can be used in non-invasive MRI as well [61]. These Au- Fe_3O_4 dumbbell nanoparticles when loaded with drugs and functionalized with targeting agent on the surface can be a very unique targeted therapeutic and diagnostic agent, termed recently known as theranostic agents.

Our dumbbell Au-Fe_3O_4 NP core has two chemical surfaces at opposite ends such that each end can be separately functionalized. In this study, the Fe_3O_4 surface of the Au-Fe_3O_4 core was first modified by dopamine then coated with carboxylic acid-terminated PEG polymer. This method helped to stabilize the NP in an aqueous environment and provided a functional surface for antibody conjugation. The gold component of the Au-Fe_3O_4 nanoparticle provided a convenient functional surface for gold-thiol bond based conjugation and pH low insertion peptide (pHLIP) was conjugated to the gold surface. Thus, in our study, ligand loading to the Au-Fe_3O_4 NP was independent to the

interference. The polymer can be further modified to introduce drug or a therapeutic agent.

Hydrophobic MIONs can be loaded with an anticancer drug doxorubicin hydrochloride (DOX) coated with amphiphilic polymer with or without targeting agent. Interestingly, the drug was released much slower in pH 7.4 than in pH 5 [63]. Similarly, anti-cancer drug methotrexate (MTX) was coupled to aminated surface of MNIOs; the drug was released at low pH of lysosomes and the enzyme proteases [60]. Au-thiol chemistry has been extensively used to load drugs and attach targeting agents [60]. Besides that, covalent attachment of DOX onto the hydrophobic shell of polymer was obtained in 17 wt % loading. The drug released in the low pH environment which used acid-cleavable hydrazine linkage.

In addition to increased tumor accumulation and reduced side effects, conjugation of pHLIP can help diagnosing small tumor at the early stage. These NPs then can be further modified with the antibody for drug delivery after the initial diagnosis and antigen overexpression profiling.

Despite, the drug delivery and therapeutic uses of NPs, there is a lot of concern about the fate of Au and Fe_3O_4 NPs remain in the body which might affect the organs in the long term. However, in our experiment, we see that Fe_3O_4 is already started to get degraded. Au- Fe_3O_4 NPs are degraded in splenocyte of spleen within 24hr of the incubation time. We studied the long term, biodistribution in the next sub-chapter which also shows the similar result of clearance of nanoparticles from the mice within 45 days of treatment. The spleen, like the liver and kidneys, acts as a filter. When blood passes through the spleen, it recycles old red blood cells that are nearing the end of their lifespan. The spleen

can scavenge iron and other useful materials for reuse. Splenocytes can also work to identify foreign antibodies and rogue cells in the blood, and will destroy them. The splenocyte is one of the body's lines of defense against infection [64].

Thus, we present a novel diagnostic Au- Fe_3O_4-pHLIP NPs which can target tumor cells and accumulate enough in vivo for distinguishing tumor region or the early diagnosis. The NPs potentially can be further modified to with antibody, and therapeutic agents to administer and observe the progress of therapeutic.

3.2 Targeted therapeutic using DOX-Au- Fe_3O_4 -MUC1 Constructs

3.3 Introduction

Several different formulations of core/shell, dumbbell nanoparticles, bi-metallic and multi-metallic nanoparticles have been used for therapeutics. Surface characteristics, size, targeting ligands play important role in drug delivery applications. To get the maximum efficiency the theranostics agents should be engineered smartly so that the drugs can be delivered only to the diseased area so that the side effect to normal tissues and organs can be minimized and the retention time of nanoparticle increases.

1) Magnetic property of nanoparticles can be used to guide and concentrate nanoparticles to the diseased area using an external magnet.

2) Modify the surface with antigens, bio-markers, key- lock mechanism for further

targeting tumor cells.

3) Attach drugs using pH sensitive bonds so the drugs will release at the targeted area

We combined both Au and Fe_3O_4 into one bi-functional dumbbell nanoparticle. Au-Fe_3O_4 NP has two different chemical surfaces that can be modified independently and are bi-directional or bi-functional. Previously we reported that Au- Fe_3O_4 NPs could be conjugated to trastuzumab, a Her2/neu specific monoclonal antibody, and to cisplatinum. Her2-Au- Fe_3O_4-cisplatin NPs enhanced *in vivo* magnetic resonance imaging [21] and were toxic to Her2/neu positive breast cancer cells [65]. Although this pioneering work demonstrated potential application of Au- Fe_3O_4 as a theranostic platform, only ~25%

breast cancers are Her-2/neu positive [66], limiting the application of Her2-Au- Fe_3O_4-cisplatin. Thus a universal targeting system for most types of breast cancers is highly desired.

MUC1 is overexpressed in 95% of breast cancer cells. MUC1 has multiple immunogenic repeats within its extra-cellular domain with each domain providing a potential binding site for anti-MUC1 antibody, making MUC1 an ideal target for NP-targeted drug delivery. pH-sensitive linkers ensure NP stability in the serum; drug release is confined to acidic milieu such as the endosome. Since the Fe_3O_4 moiety can function as a contrast agent for non-invasive magnetic resonance imaging [21], Au- Fe_3O_4 are ideal theranostic agents.

Controlled release of a chemotherapy drug from a NP delivery system reduces its side effect and and the dose for effective DNA damage. The tumor microenvironment is more acidic than normal tissues, and the principal components of the endocytosis pathway, endosomes and lysosomes are acidic as well.

We will examine the use of the nanoparticles with *in vitro* and *in vivo* studies. The initial Schiff Base polymer linker work was accomplished by Dr. Kai Cheng. Cellular uptake and *in vivo* experiment was accomplished by Dr. Zhenglong Yuan and Dr. Maureen Chung at the Rhode Island Hospital.

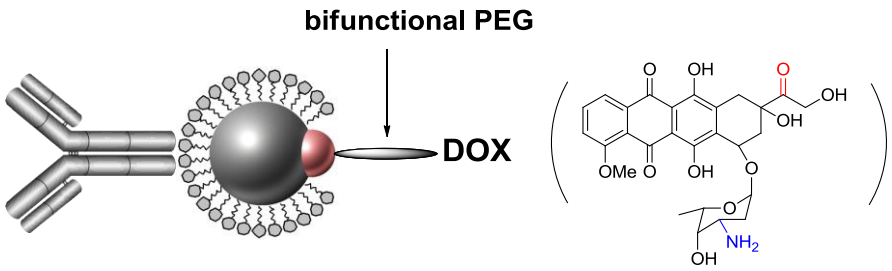

Figure 39: Schematic illustration of the surface functionalization of the Au- Fe_3O_4 NPs. Doxorubicin is attached using Schiff base PEG linker on the Au side and Muc1 is attached using Dopamine-PEG-COOH linker on the Fe_3O_4 side.

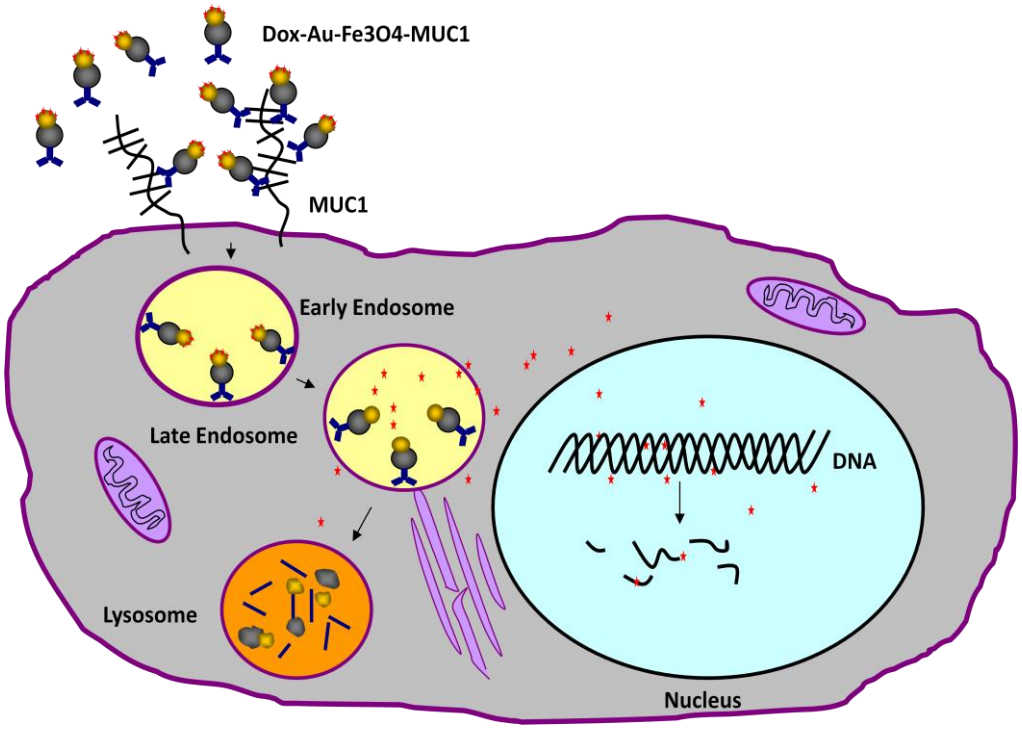

Figure 40: Schematic illustration of uptake of Dox-Au- Fe_3O_4 _MUC1 costructs into the cell and its pathway to the nucleus. Dox-Au-Fe_3O_4-MUC1 is a novel bi-functional nanoparticle that selectively targets MUC1 positive breast cancer cells. DOX-Au Fe_3O_4-MUC1 is internalized through endosomes and the DOX is released in low pH of lysosome which then travels to the nucleus.

3.4 Methods

Materials

All chemicals including α,ω-bis {2-[(3-carboxy-1-oxopropyl) amino] ethyl} polyethylene glycol (PEG 3000 diacid, M_t = 3000), poly(ethylene glycol) bis (carboxymethyl) ether (PEG 600 diacid, M_t = 600), poly(ethylene glycol) bis(amine) (PEG 500 diamine, M_t = 500), doxorubicin hydrochloride, fluorescein 5(6) isothiocyanate (FITC), iron pentacarbonyl were purchased from Sigma-Aldrich, St. Louis, MO. Hydrogen tetrachloroaurate (III) hydrate was ordered from Strem Chemicals, Inc., Newburyport, MA. *N*-hydroxysuccinimide (NHS) and 1-ethyl-3-(3-dimethylaminopropyl) carbodiimide, hydrochloride (EDC) were purchased from Pierce Biotechnology, Rockford, IL. Triethylamine and dichloromethane (DCM) were distilled prior to use, and *N, N'*-dimethylformamide (DMF) was stored over molecular sieves. Other solvents and chemicals were used as received. All buffers and media were purchased from Invitrogen, Carlsbad, CA. Deionized water was obtained from a Millipore Milli-DI Water Purification system. The dialysis membrane tubing (MWCO: 12,000 ~ 14,000, and 300,000) were purchased from Spectrum Laboratories, Rancho Dominguez, CA.

3.4.1 Retrosynthesis of LA-PEG-500-SB-DOX:

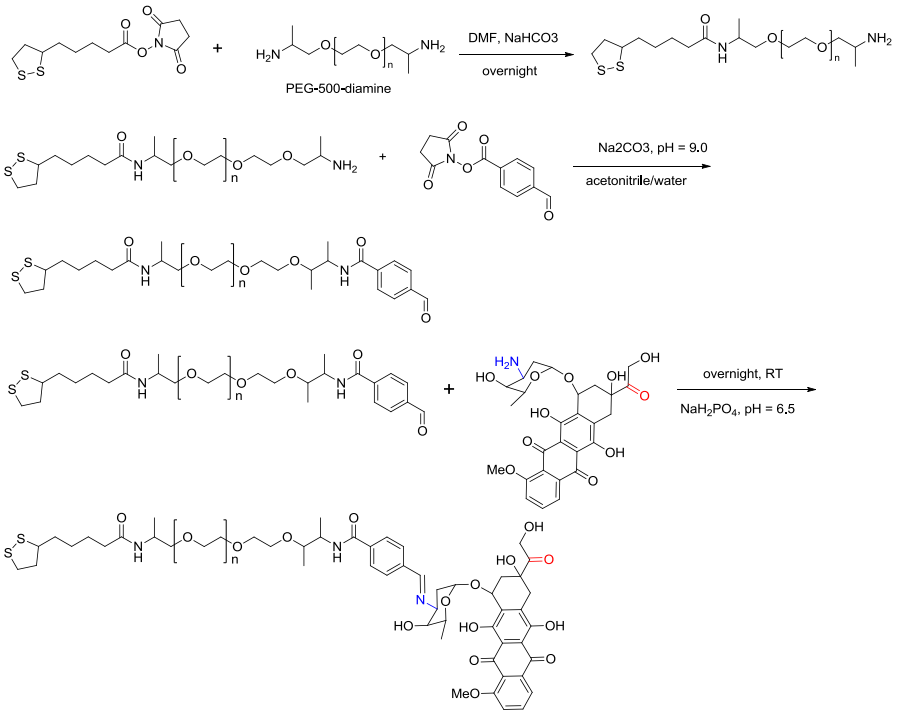

3.4.2 Synthesis of LA-PEG-500-SB-DOX

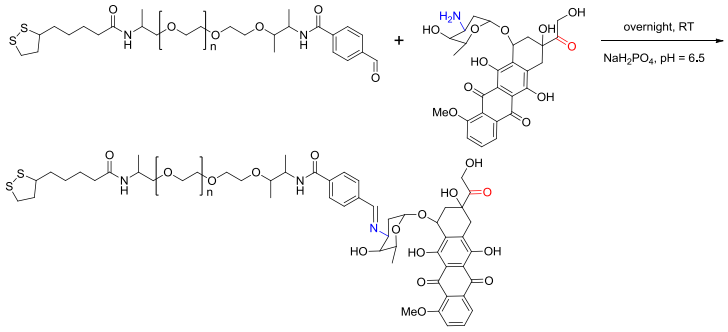

First, LA-PEG-500-CHO is synthesized from 4-formyl-benzoic acid 2,5-dioxo-pyrrolidin-1-yl ester (succinimidyl 4-formylbenzoate, SFB from the literature [67]. To 1 mL of LA-PEG-500-CHO (4 mM in acetonitrile) was mixed 100 mM NaH_2PO_4 (pH 6.8) in a vial. The mixture was added 0.5 ml of DOX in methanol (5 mg/mL) in 100 μL portions every 30 min. After 8 hours of agitation at room temperature in the dark, the

sample was centrifuged to remove insoluble materials. The supernatant was then purified by Sephadex LH20 in methanol to separate the conjugate from free DOX. The high molecular-weight fractions were evaporated and dissolved in water, and purified further by Sephadex G25 in water. The high-molecular-weight fraction was lyophilized to provide the product as a red powder. The amount of DOX conjugate to the linker was determined by measuring the absorbance at 488 nm of a solution of DOX conjugate in water, using an extinction coefficient for DOX of 11,500 L/mol cm.

3.4.3 Conjugation of MUC1 antibody and Au-Fe_3O_4 NPs (Au-Fe_3O_4-MUC1)

To couple MUC1 antibody to NP, Au-Fe_3O_4 (1 mg of Fe in 2 ml of water, 0.2 nmol of NP) in water was mixed with 1-ethyl-3-(3-dimethylaminopropyl) carbodiimide (EDC, 1.0 mg, 5 μmol) and sulfo-NHS (2.2 mg, 10 μmol) for 30 min at room temperature. The conjugate was filtered through a PD-10 column pre-washed with PBS to remove excessive EDC and sulfo-NHS. MUC1 antibody (100 μg, 0.6 nmol) was added into the PBS solution of activated Au-Fe_3O_4 and the resultant solution stirred for 2 hours at room temperature or overnight at 4°C. The final conjugate was separated from unbound MUC1 antibody by dialysis (MWCO = 300 KDa) against PBS. The final iron or gold concentration of Au-Fe_3O_4-MUC1 was measured by ICP-AES analysis.

3.4.4 Conjugation of DOX-PEG linkers and Au- Fe_3O_4-MUC1 (DOX-Au- Fe_3O_4-MUC1)

As-prepared Au-Fe_3O_4-MUC1 (1 mg of Fe in 2 ml of PBS, 0.2 nmol of nanoparticles) was directly mixed with DOX-PEG linkers (LA-PEG-500-AM-DOX, LA-PEG-600-HZ-DOX, or LA-PEG-500-SB-DOX, 1 mM in 0.5 mL of PBS, 500 nmol) at RT overnight. The uncoupled ligand was removed using a PD-10 column. Dialysis against 10 mM PBS buffer by tubing (MWCO = 30 K) for 12 hours at 4°C was performed. The final iron or gold concentration of DOX-Au- Fe_3O_4-MUC1 was measured by ICP-AES analysis.

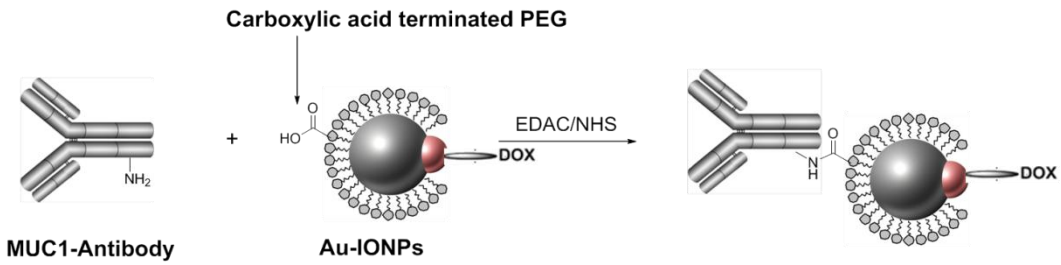

3.4.5 Doxorubicin release from DOX -Au- Fe_3O_4- MUC1 construct

The kinetics of doxorubicin release from DOX-Au- Fe_3O_4-MUC1 conjugated using Schiff-base linkage was determined. Doxorubicin is quantified using fluorescence absorption (excitation/emission=470/592 nm). 1 mg/ml of purified DOX-Au- Fe_3O_4-MUC1 in PBS was transferred into a dialysis membrane (MWCO=12,000 kDa) that permitted passive diffusion of free doxorubicin but not DOX-Au-Fe3O4 -MUC1. Dialysis was performed in buffers with pH 5.0 or 7.4 at 37 ºC. 1 ml aliquot of buffer solution was taken at pre-determined time intervals over 24 hours and doxorubicin concentration determined using fluorescence absorption. 1 ml fresh PBS was added to maintain the starting volume after each aliquot was removed.

3.4.6 Histological analysis: Cell uptake, Doxorubicin localization

Confocal microscopy was used to visualize DOX-Au- Fe_3O_4 -MUC1 using reflectance (gold excitation 555 nm /emission 586 nm) and red fluorescence (Doxorubicin excitation 488 nm/emission 592 nm)), respectively. Breast cancer cells were treated with DOX-Au-Fe_3O_4-MUC1 at 50 ug/ml concentration for 4h, washed and fixed with 4% paraformaldehyde, permeabilized with 0.1% Triton-X followed by DAPI (blue) counter-staining for nucleus. Presence of Doxorubicin was determined using fluorescence overlay

on blue DAPI and red Doxorubicin. Fluorescent images were obtained on a Zeiss LSM 710 Confocal Laser Scanning Microscope.

The relative nuclear Doxorubicin concentration was quantified using the red fluorescence signal intensity, which was analyzed by Image J software. All pictures were taken under same conditions with three images for each treatment condition. The red signal intensity for each condition was compared using a student t test.

3.4.7 DOX-Au- Fe_3O_4-MUC1 in vitro cytotoxicity assay

Cell cytotoxicity in MCF-7 cells was determined using a MTT (3-(4,5-dimethylthiazol-2-yl)-2,5-diphenyl tetrazolium bromide (Sigma-Aldrich, St. Louis, MO) assay. MCF-7 cells were plated at a concentration of 6×10^3 cells/well and incubated for 24 h. After washing, varying concentrations of DOX-Au- Fe_3O_4-MUC1, Au- Fe_3O_4-DOX, Au- Fe_3O_4 NP core and unbound doxorubicin were added to the cell media. After 24h of nanoparticle incubation, MTT compound was added for 3h, followed by DMSO. Cell viability was determined using absorbance at 570 nm with a reference wavelength of 650 nm. All samples were done in triplicate and the experiment was replicated three times. Results were compared using a student t test.

3.4.8 Xenograft studies

Severe combined immunodeficient (SCID) mice were xenografted with ZR75-1 human breast cancer cells (17). Ten million ZR75-1 cells were injected subcutaneously in the right flank of female scid/scid mice 4-6 weeks old (Charles River Laboratories). There were 3 groups of animals with 10 animals per group. All animals received a single tail-vein injection approximately 4 weeks after tumor engraftment. Group 1 received

DOX-AuFe$_3$0$_4$-MUC1 containing a dose of doxorubicin equivalent to 3 mg/kg. Group 2 received unbound doxorubicin (3 mg/kg) and Group 3 received a saline placebo injection. Tumor growth and animal weight was assessed semi-weekly for 4 weeks. Tissue was obtained at necropsy. Duncan multiple comparison test was used for tumor size analysis. Differences in body weight were analyzed using a linear mixed model. Animal experiments were performed in accordance with IACUC guidelines.

3.5 Results and Discussion:

The conjugation of MUC1 antibody increased the hydrodynamic size by 20nm as it is expected of a large antibody. Zeta potential, which measures the surface potential of NPs decreased by 12mV. However, the net potential is still in the negative so the NP construct is still stable in the solution.

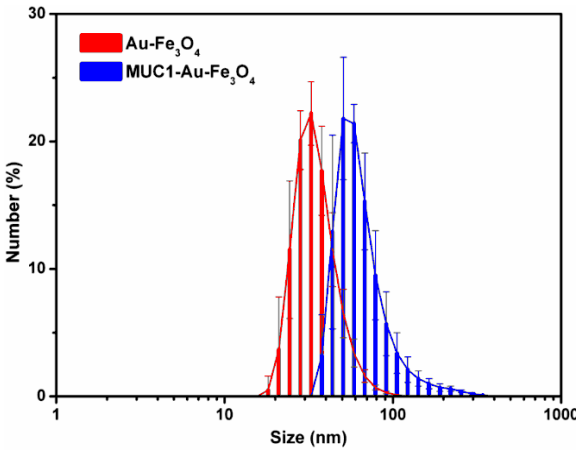

	Au-IONPs	MUC1-Au-IONPs
Zeta Potential (mV)	-33.2	-21.7

Figure 41: Au-Fe_3O_4-MUC1 nanoparticle size increased from ~30 nm to ~50 nm with the addition of MUC1 antibody. The zeta potential of Au-Fe_3O_4-MUC1 was -21.7 mV compared to the Au- Fe_3O_4 nanoparticle core that was -33.2 mV.

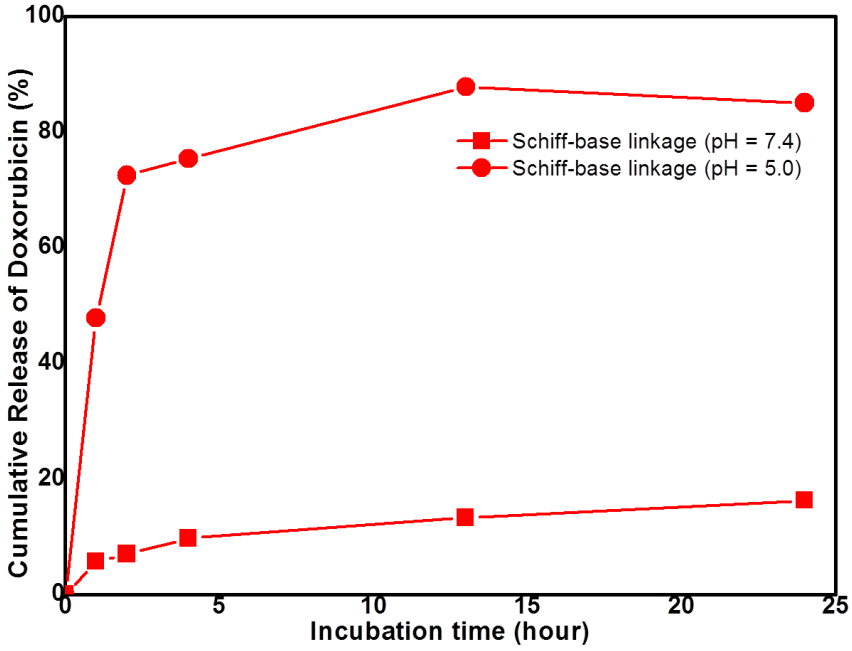

Figure 42: Release of doxurubicin from DOX-Au- Fe_3O_4-MUC1 was evaluated at neutral (pH=7.4) and acidic pH (pH=5.0). Schiff-base linker is relatively stable at a neutral pH (depicted by squares) with minimal free doxorubicin detected after 24 hours. 85% of DOX is released in 14 hr incubation time at 37 degree celsius.

Different types of pH sensitive linkages are used to attach drugs most common being amine and hydrazine bonds. However, these bonds are easily broken by the enzymes even at neutral pH thus unfavorable for the pH sensitive targeting. Ideally, to achieve tumor specific drug release, DOX-Au-Fe3O4 - MUC1 should be stable at a neutral pH

with release of Doxorubicin only under acidic conditions. The Figure 42 shows the release of Doxorubicin only at the low pH 5.0 under biological condition.

Quantitative Measurement of MUC1-antibody binding to Au-Fe_3O_4

	Fe concentration (ug/ml) by ICP	MUC1 loading (ug/ml)	MUC1 per mg of Fe (ug/mg)
MUC1-Au-IONPs	587.34	300.59	511.78

Quantitative measurement of MUC1-Ab binding to Au-Fe_3O_4 is based on the method of Bradford.

Assumptions:

Au-Fe_3O_4 are composed of avg. 16 nm of iron oxide and 4 nm of Au.

Weight of Single $Fe_3O_4 = 1.1152 \times 10^{-17}$ g

Mol of bound MUC1 = 3.435×10^{-9}

Ratio of MUC1 Ab to Au-Fe_3O_4 = 1.67 : 1

Ratio of DOX to Au-Fe_3O_4 =137: 1

For each NP, we found the loading to be about 137 DOX and 1.67 antibody. These loadings are similar to the reported values on Au NPs.

3.5.1 Endocytosis of DOX-Au-Fe3O4 -MUC1 traffics leads to doxorubicin localizing to the nucleus

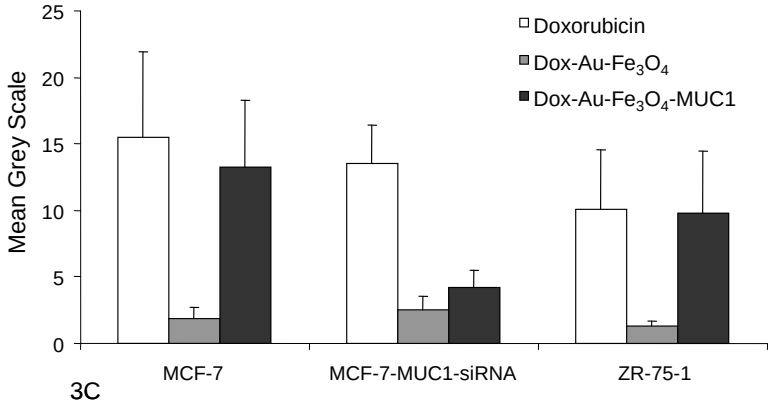

Figure 43: DOX intensity inside nuclei was analyzed by ImageJ software. In MCF-7 cells, increased nuclear DOX intensity was observed in cells with unbound DOX and DOX-Au-Fe3O4 -MUC1 treatment, whereas in MCF7-MUC1-siRNA cells, increased DOX signal was only seen with cells treated with unbound DOX.

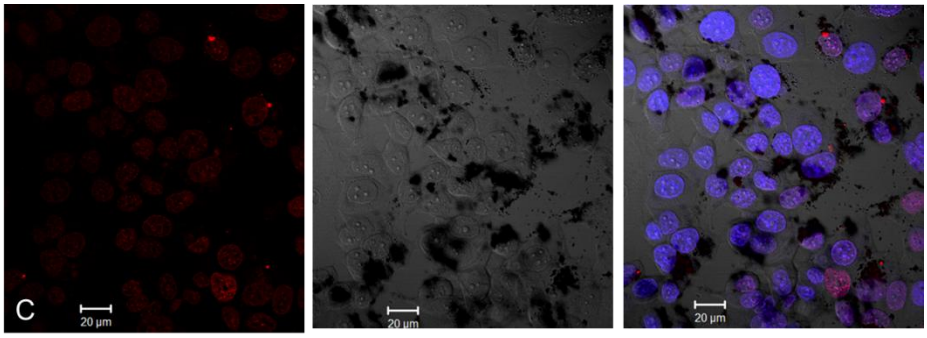

Figure 44: MCF-7 and MCF7-MUC1-siRNA cells were treated with free DOX, Au-Fe_3O_4 -DOX, and DOX-Au-Fe_3O_4 -MUC1 for 4h, washed and fixed for confocal microscopy. DOX stained red and was clearly visible in the nucleus (stained blue). The black $AuFe_3O_4$ NP core was visible outside of the nucleus.

After 4 hour of treatment, DOX-Au-Fe_3O_4-MUC1 was observed in the cytoplasm and doxorubicin was detected within the nucleus (Figure 44). The detection of doxorubicin in the nucleus suggested that doxorubicin was able to dissociate from DOX-Au- Fe_3O_4-MUC1 after cellular internalization and translocate to the nucleus. DOX-Au-Fe_3O_4-MUC1 treatment resulted in comparatively more doxorubicin within the nucleus of breast cancer cells than that observed using doxorubicin, and more than that observed with DOX-Au- Fe_3O_4. These results are further supported by the mean grey scale of red DOX signal inside the nuclei (Figure 43). The Muc1 antibody is effective in targeting Muc1 positive cells, as the mean intensity is much different in MCF-7 and MCF7-MUC1-siRNA cells (Muc1 negative). These constructs were also able to be internalized in ZR-75-1 (breast cancer carcinoma, highly metastatic) cells which express MUC1.

This current study identified Au-Fe_3O_4-MUC1 within the peri-nuclear region 4 hours after incubation. The observed time frame is consistent with Au- Fe_3O_4-MUC1 translocation to the nucleus via endosomes or lysosomes through ligand-dependent endocytosis. Doxorubicin release at an acidic pH and accumulation of NP-released doxorubicin within the nucleus further supports intracellular trafficking of DOX-Au-Fe_3O_4-MUC1 through endosomes.

3.5.2 DOX-Au-Fe3O4 -MUC1 cytotoxicity in MCF-7 cells

Unbound doxorubicin at 1.5 µM concentration killed 80% of MCF7 cells. DOX-Au- Fe_3O_4-MUC1 construct containing 1.5 µM DOX had comparable toxicity for MCF7 cells Figure 45. The Fe concentration in 1.5 µM DOX-Au- Fe_3O_4-MUC1 is equivalent 100 µM. 100% cell viability was observed after treatment with Au- Fe_3O_4 NPs (100 µM). DOX-Au- Fe_3O_4-MUC1 was more toxic to MCF-7 cells than non-targeted DOX-

Au- Fe_3O_4. MUC1 effectively targeted MUC1 positive cells and it has cytotoxicity similar to free DOX at equivalent concentrations.

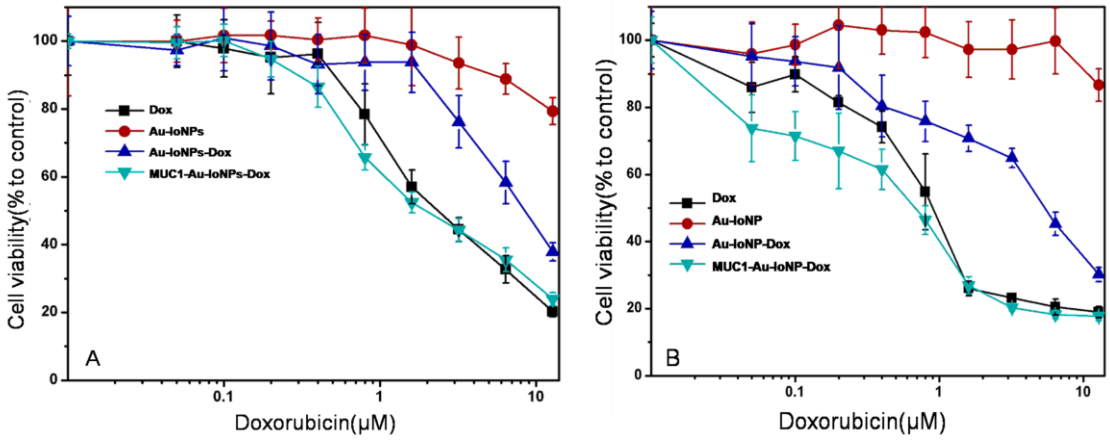

Figure 45: DOX-Au- Fe_3O_4 -MUC1 inhibits breast cancer growth. MCF-7 cells (left) and ZR75-1 (right) were treated with free doxorubicin, Au- Fe_3O_4 as NP control, DOX-Au- Fe_3O_4 as MUC1 control and DOX-Au- Fe_3O_4 -MUC1 for 24 hr. Cell viability was determined by MTT assay. DOX-Au- Fe_3O_4-MUC1 showed similar cytoxicity as doxorubicin, but higher than that for DOX-Au- Fe_3O_4 NPs demonstrating effective MUC1 targeting on both MUC1 posotive breast cancer cells.

3.5.3 DOX-Au- Fe_3O_4 -MUC1 selectively inhibits tumors in vivo

MCF-7 tumor cells inoculated on the right flank of a immune-compromised mouse model and tumor was allowed to grow for three weeks. Free Dox, NP control and NP-DOX-MUC1 were tail-vain injected into mice 3 times in 3 weeks period based on equivalent DOX concentration of 23.7 ug/ml.

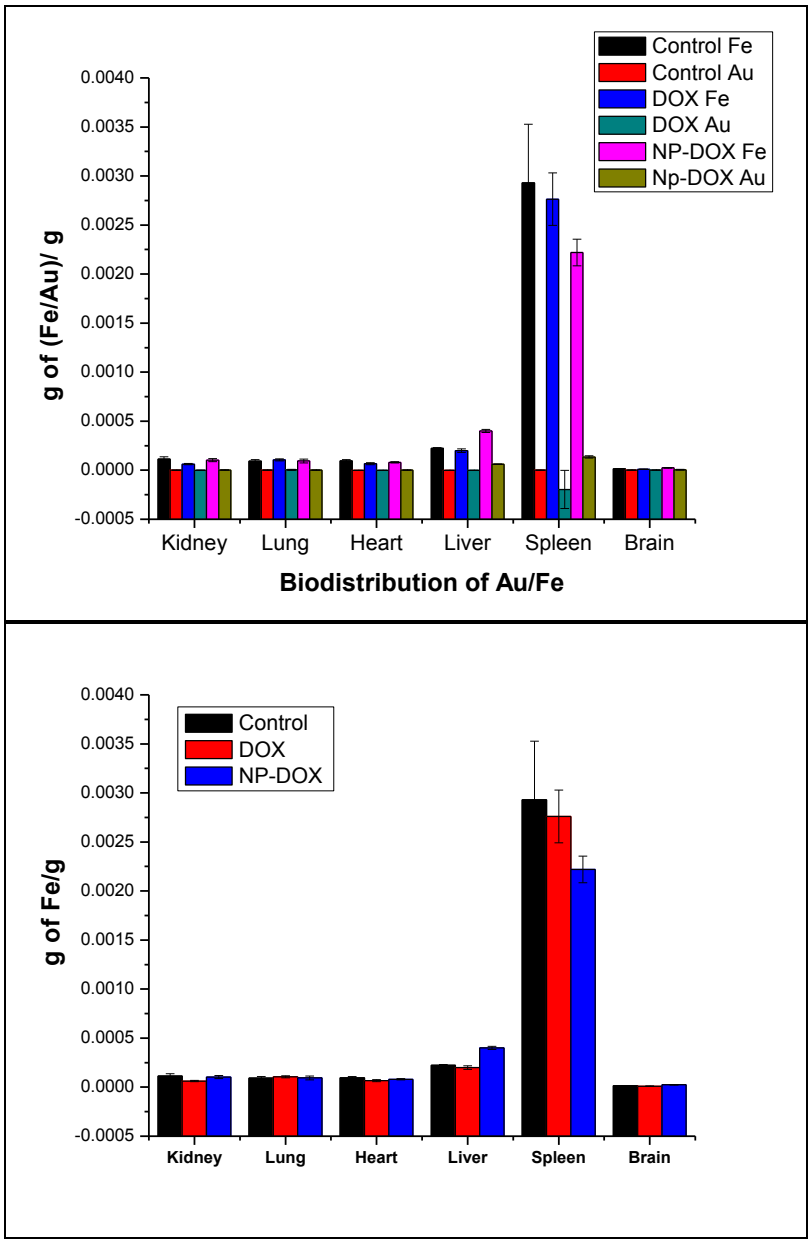

Figure 46: Biodistribution of DOX-Au Fe_3O_4-MUC1 NPs based on DOX concentration showing no retention of elements after 45 days. Injection of NPs into mice 3 times in 3 weeks period based on 23.7 ug/ml DOX concentration. Top graph showing both Au and Fe, bottom showing just the Fe element.

After 45 days of treatment, mice were sacrificed to do the elemental analysis. The organs were

heated in 1-2 ml of nitric acid until they dissolved. Then, 1 ml of HCl was added. Afterwards, Hydrogen peroxide was added to dissolve the fat. DI water was added to adjust the volume to 2% nitric acid. Samples were analyzed by ICP-AES. The Au weight is very negligible in mice treated with NP-DOX in most of the organs compared to the control. The Fe and Au are seen in negligible amount in liver of NP-DOX treated mice. However, the significant amount of NPs have seen to be cleared out by the body.

3.5.4 DOX-Au-Fe_3O_4-MUC1 inhibits in vivo human breast cancer growth with less myocardial toxicity

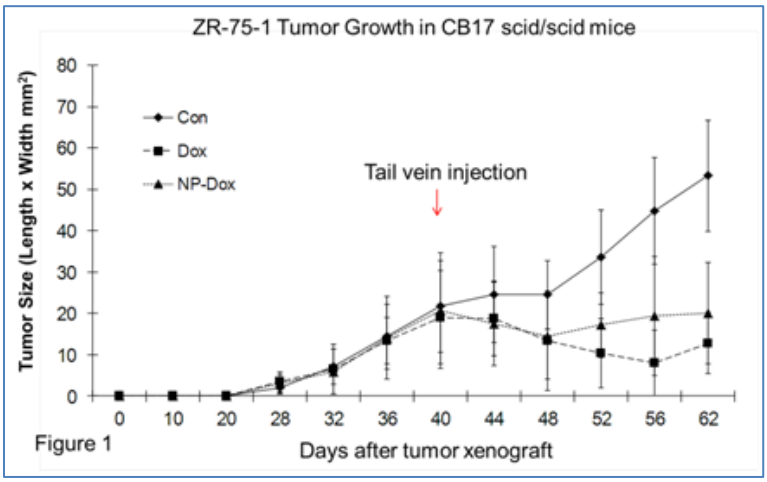

Figure 47: DOX-Au- Fe_3O_4 -MUC1 and unbound doxorubicin inhibited human breast cancer growth in scid mice xenografted with human breast cancer cells. The rate of tumor growth was similar in the three groups prior to the tail vein injection. After the tail vein injection, tumor growth was inhibited in DOX-Au-Fe_30_4-MUC1 (NP-Dox) and Doxorubicin (Dox) compared to the placebo (CON) group (Dox vs control, $p<0.001$, NP-

Dox vs CON, $p<0.05$) with the most tumor inhibition observed in the unbound Doxorubicin group (Dox vs NP-Dox, $p<0.05$). Arrow depicts day of tail vein injection.

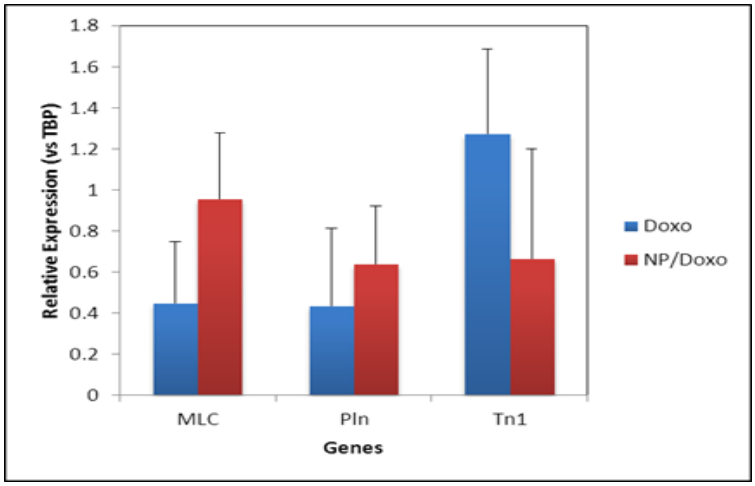

Figure 48: RT-PCR for myocardial specific genes demonstrated relatively more troponin in Doxorubicin treated animals compared to those treated with DOX-Au-Fe_3O_4-MUC1. Conversely, there was more MLC and Pln mRNA showing more rate of releaxation, thereby decreasing stroke volume and heart rate.

In vivo experiments demonstrated that DOX-Au-Fe_3O_4-MUC1 inhibited human breast cancer growth. The rate of tumor growth was similar in the three groups prior to treatment (Fig. 47). After the tail vein injection, tumor growth was inhibited in mice that received DOX-Au- Fe_3O_4 -MUC1 or unbound DOX as compared with mice that received saline placebo (DOX vs placebo, $p<0.001$, DOX-Au-Fe_3O_4-MUC1 vs placebo $p<0.05$). The average tumor size at necropsy was 0.62 g for the placebo group, 0.16 g for the group receiving unbound DOX and 0.295 g for the group treated with DOX-AuFe_3O_4-MUC1. The mean tumor size was largest in the placebo group ($p=-0.0012$). The

difference between the means for the DOX and DOX-$AuFe_3O_4$-MUC1 groups was not statistically significant.

However, we demonstrated that our NP construct is not as toxic to myocardial cells as free Doxorubicin. RT-PCR demonstrated that troponin 1 gene expression was increased in the hearts of mice treated with unbound DOX when compared to mice treated with DOX-$AuFe_3O_4$-MUC1 (Figure 48). Conversely, there was less myosin light chain (MLC) RNA expressed in the hearts of mice treated with unbound DOX.

DOX is toxic to the heart and limits its administration. Our study showed that one month after treatment, mRNA levels for troponin and myosin light chain differed between mice treated with unbound DOX and those receiving DOX-Au-Fe_3O_4-MUC1. Troponin I mRNA levels were greater in DOX treated mice suggesting that these animals had suffered myocardial damage since troponin concentrations in the blood is an indication of irreversible myocardial cell injury and predates ultra-structural changes.

3.6 Discussion:

Chemotherapeutic drugs are challenged by non-specificity and thus causing high toxicity to normal cells and organs. Besides, tumors also develop multidrug resistance (MDR) against anticancer drugs after few chemotherapy sessions. It is hypothesized that focal high dose strategy works for MDR tumor at cellular level [28].

In addition to increased tumor accumulation and reduced side effects shown by free DOX in heart, conjugation of chemotherapy to NP may help overcome multiple drug resistance (MDR), a major obstacle often encountered in clinical practice. Ligand based nanoparticle constructs internalize in cells via different pathway, endocytosis, and are not

affected by the MDR than free dox which is directly diffused to nucleus [68]. This study demonstrated that DOX-Au- Fe_3O_4 -MUC1 was similar to unbound doxorubicin in inhibiting breast cancer growth in equal concentration. In addition to targeted drug delivery, the intrinsic properties of Au and Fe_3O_4, DOX-Au- Fe_3O_4 -MUC1 can be used for non-invasive imaging.

This study described the construction and characterization of theranostic DOX-Au-Fe_3O_4-MUC1 NPs. Doxorubicin was released only in low pH 5.0 from DOX-Au- Fe_3O_4-MUC1 construct. Target specificity of DOX-Au- Fe_3O_4-MUC1 was confirmed using MCF-7 (weakly metastatic) breast cancer cells which express MUC1. Confocal microscopy confirmed the intracellular localization of DOX-Au- Fe_3O_4 -MUC1 and the presence of doxorubicin in the nucleus. These constructs were able to be internalize in ZR-75-1 (breast cancer carcinoma) cells which express MUC1 and are highly metastatic [69].

Furthermore, DOX-Au- Fe_3O_4 -MUC1 inhibited *in vitro* growth of MUC1 positive human breast cancer cells as shown by the cytotoxicity assay (Figure 47**:**). DOX-Au-Fe_3O_4-MUC1 were slightly more effective in killing cancer cells as free DOX in equal concentration. This effectiveness combined with the targeting and controlled pH release makes our theranostic construct highly noble and desirable.

Most importantly, DOX-Au- Fe_3O_4-MUC1 NP construct showed tumor inhibition within 3 weeks of treatment in mice. Furthermore, the fate of Au- Fe_3O_4NPs in the body was checked by elemental analysis. Biodistribution (Figure 46: Biodistribution of DOX-Au Fe_3O_4-MUC1 NPs based on DOX concentration showing no retention of elements after

45 days. Injection of NPs into mice 3 times in 3 weeks period based on 23.7 ug/ml DOX concentration. Top graph showing both Au and Fe, bottom showing just the Fe element.) did not reveal extra Fe or Au present in the vital organs after 45 days of NP treatment. These constructs are better than free Doxorubicin by overcoming MDR, targeting tumor causing less cytotoxicity to the vital organs. Thus, we were able to demonstrate dumbbell Au- Fe_3O_4 NPs which may be a novel mode of combining non-invasive imaging and targeted drug delivery.

Chapter 4 FeAu Alloy Nanoparticles as Therapeutics for Tumor Inhibition

4.1 Introduction:

Recent development of nanoparticles as drug delivery agents has been very progressive and has high potential in effective treatment. Despite the best efforts of drug design using targeting ligands, polymers very few have reached the clinical trial [70, 71]. This is due to the multi-steps involved in conjugating targeting ligand and therapeutic drug. The yield is very low and the stability and repeatability of such drug loading is hard to achieve. Furthermore, targeting ligands, surface coating and drugs interfere decreasing the effectiveness of therapeutics. To avoid such problems new class of therapeutic NPs are searched which can act as drug itself as they are toxic to the cancer cells, in the presence of external stimulus (hyperthermia) or internal stimulus (low pH: Fe release) [72]. Hyperthermia, where the magnetic particles are heated selectively by application of an high frequency magnetic field. Cancer cells cannot withstand the high heat caused by the MNPs and undergo apoptosis. The side toxicity to the normal cells can be significantly reduced if targeted to the specific area, where it can be activated using external/internal stimulus. Similar to the hyperthermia, FePt NPs have been shown to be therapeutic.

In a recent study, FePt NPs have been shown to release Fe in the intracellular low pH environment. These FePt particles have shown promising results in being cytotoxic towards cancer cells [73]. Figure 49 shows the schematic illustration of Fe release and the production of Reactive Oxygen Species (ROS) inside the cells which in turn caused the cells to undergo apoptosis. The FePt nanoparticles functionalized with PEG-Phospholipid ligand exhibit dose-dependent cytotoxicity as shown in variable cancer cell lines in

Figure 50 A. The Fe_3O_4 NPs functionalized with PEG- Phospholipid was used as a control which did not cause any toxicity to the cancer cells. Furthermore, the cells were incubated with FePt and FePt+ 2-2bipyridine. The Fe released from FePt nanoparticles were chelated using 2-2bipyridine. The cell viability increased by 50% in cultures including 2-2bipyridine than ones without (Figure 50 B). This further proves that the toxicity arised from the Fe released from the nanoparticle and not FePt funcationalization or NPs by itself.

The Fe (II) reacts with the H_2O_2 present in the cell to form reactive oxygen species (ROS). ROS in high concentration causes the cells to undergo apoptosis due to rapid lipid oxidation, DNA and protein damage [74].

Fenton Reaction $Fe(II) + H_2O_2 \rightarrow {}^{\bullet}OH + OH^- + Fe(III)$

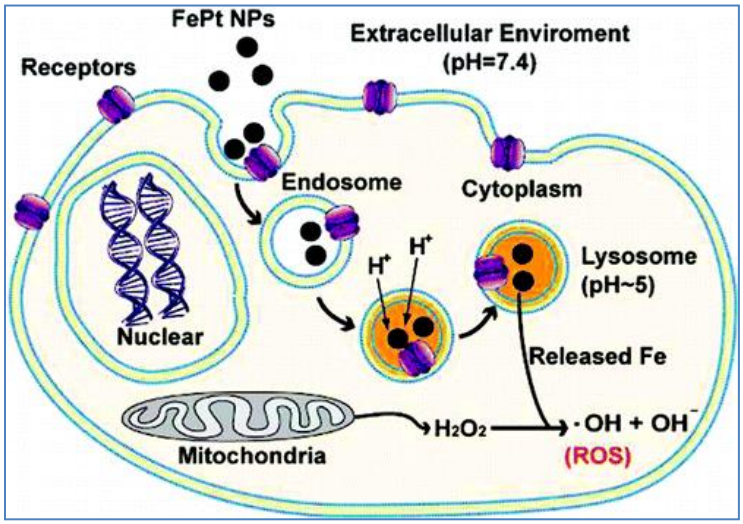

Figure 49: Schematic illustration of Fcc-FePt showing Fe release in intracellular compartments which undergoes Fenton reaction with H_2O_2 producing Reactive Oxygen Species (ROS)

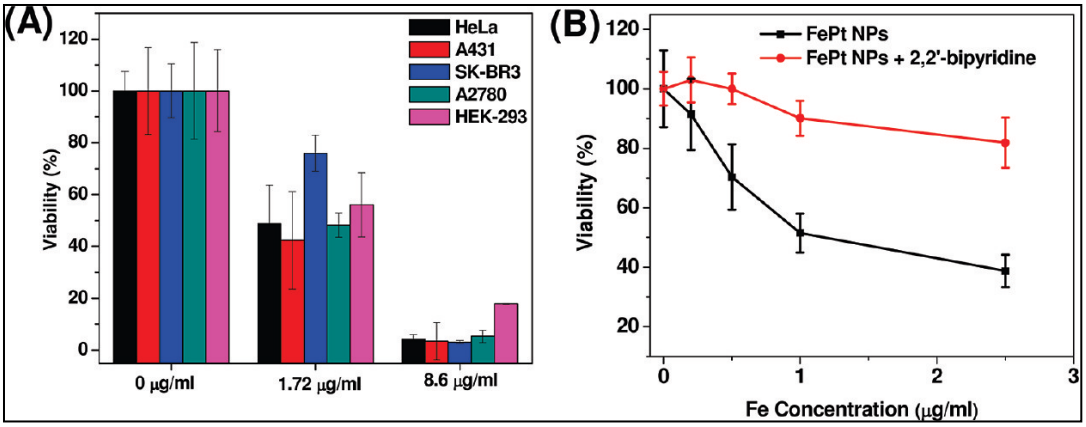

Figure 50: A) MTT cellular viability of several tumor cell lines incubated with fcc-$Fe_{40}Pt_{60}$ NPs at different iron concentrations at 37 ºC for 24 h. FePt shows toxicity in all cancer cell lines. (B)Viability of A2780 cells incubated with fcc-Fe40Pt60 NPs or with fcc-$Fe_{40}Pt_{60}$ NPs plus 200 μM 2,2-bipyridine at 37 ºC for 24 h. Reprinted with permission from reference 68.

Recently, we synthesized FeAu NPs with tunable magnetic and optical properties [75]. The FeAu alloy NPs are characteristically similar to that of fcc-FePt so we believed these NPs would also be therapeutic. Induced ROS production can cause cellular aging and apoptosis and can therefore function as anti-tumourigenic species. Since, both the Fe and Au are non-toxic metals, FeAu NPs alleviate the concern towards the fate of NPs after the Fe release in cells, tissues and organs. Furthermore, the optical property of FeAu NPs can be utilized to monitor disease progression through optical imaging. The ROS production can also induce cellular senescence and apoptosis and can therefore function as anti-tumourigenic species.

4.2 Methods:

4.2.1 Synthesis of FeAu alloy NPs:

Gold precursor ($Au(O_2CCH_3)_3$ was mixed with solvents Oleic acid, Oleylamine and Tetralin in a Ar atmosphere. The solution was heated at 40C for 30 min. Then, Iron Pentacarbonyl was injected. The temeperature was increased to 200 C and kept at that temperature for 1 hour.

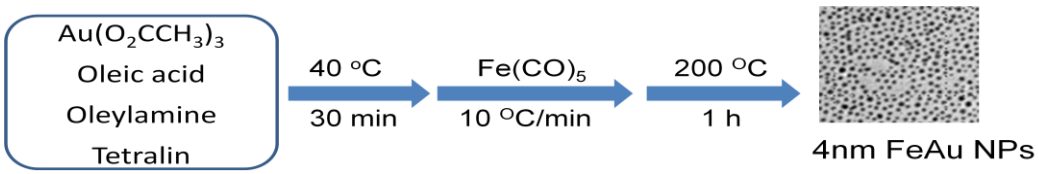

Coating NPs with Phospholipid:

As-synthesized NPs (10 mg) was dissolved in 2 mL of chloroform, 40 mg of DSPE-PEG(2000)carboxylic acid lipid (1 mL of chloroform solution) (MW 2847.779, Avanti Polar Lipids Inc.) was added and shaken for 1 hour. The solvent was removed through rotavaporation. DI water added to disperse the NPs. The NPs were further purified by a 30k or100k dialysis tubing (Spectrum Laboratories,Inc.), and the final product, FeAu-COOH, was filtered through a 0.22 μm Millex@GP filter (Millipore Corp.) to remove small amounts of aggregates. The final NP concentration was determined with ICP-AES.

4.2.2 FeAu functionalization

As-synthesized NPs (10 mg) was dissolved in 8 ml of dichloromethane (DCM). 10 mg of DMSA was dissolved in 1 mL of DMSO solution separately. The two solutions were mixed and shaken for 1 hr. 10ml of hexane was used to precipitate the NPs, centrifuged at 2000 rpm/min. Supernatant was removed and the NPs were dried. 3ml of DI water was added to disperse the NPs. The NPs were further purified by a 30k dialysis tubing

(Spectrum Laboratories,Inc.), for 24 hr. The final product, FeAu-DMSA, was filtered through a 0.22 μm Millex@GP filter (MilliporeCorp.). The final NP concentration was determined with ICP-AES.

4.2.3 Fe Release Experiment

1ml of the aqueous solution of the NPs (FePt-COOH or FeAu-DMSA) containing 1 mg of Fe were dispersed in dialysis tubing (10,000 MWCO, Spectrum Laboratories, Inc.) that was further immersed into a 100 mL PBS (pH) 7.4 or 4.8) bath at 37 ºC. A portion (4 mL) of the PBS solution was sampled, and the concentration of Fe or Pt was analyzed with ICP-AES. The initial and the final ratio between Fe and Au was also calculated as an internal standard.

4.2.4 Au-DMSA synthesis and functionalization

Au NPs were synthesized using 0.2g of $HAuCl_4$ as Au precursor and 10ml Oleylamine as surfactand and 10ml Tetralin as solvent. $HAuCl_4$ was reduced by 90mg TBAB (tetrabutylammonium bromide) at 4 ºC for 2 hours. The reaction was allowed to warm up to RT and recipitated using 25ml hexane. Centrifuged at 2000rpm for 3min and the supernatant were discarded. Then purified using PD-10 column.

As synthesized 8 nm Au NPs in hexane was evaporated and weighed 10mg. The Au NPs were dissolved in 2ml Chloroform. In a separate vial, Dimercapto succinic acid (DMSA) (Sigma Aldrich) was weighed 15mg with 0. 1mg TCEP (*tris*(2-carboxyethyl)phosphine) and 1mg Sodium Bicarbonate and dissolved in 0.5ml dimethyl sulfoxide (DMSO). Less DMSO is good for the reaction as higher amount causes aggregation of NPs due to insolubility. Under nitrogen atmosphere, reactants were shaken at RT for 6-12 hours.

After, 12 hr, NPs were precipitated in hexane, and then dissolved in DI water. NPs without TCEP and $NaHCO_3$ didn't dissolve in water. Proving that, small sodium bicarbonate is necessary to remove proton from thiol.

4.2.5 MTS Assay to measure cell viability

Colorimetric [3-(4,5-dimethylthiazol-2-yl)-5-(3-carboxymethoxyphenyl)-2-(4-sulfophenyl)-2H-tetrazolium, inner salt; MTS, Promega Corp.) assays were performed to assess the mitochondrial activity of living cells treated as the following. The cytotoxicity assay was performed in

96-wells microtiter plates (Fisher Inc.) with a seeding density of 40,000 cells per well. A549 cells were incubated for 24 h at 37 ºC in order to allow stabilization before the addition of the test substance. The cells were washed 3X and incubated with the Au-DMSA NPs and FeAu NPs at different concentration for 24 h at 37 ºC in 5% CO_2. The cells were washed 3X and 20µl/well of MTS reagent was added and incubated for 1 hour. The absorbance at 490nm was recorded using Fluorescence Plate Reader (TECAN).

4.2.6 Characterization of ROS Formation.

The manuals protocol OxiSelect™ Intracellular ROS Assay Kit (Green Fluorescence), Cell Biolabs, were followed to generate DCF control, H_2O_2 positive control, cell control and Au and FeAu as control. Briefly, A549 cells were plated at 40,000 cells per well into 96-well plates and incubated at 37 °C in 5% CO_2 and high humidity for 24 h. Cells were treated with DCFH-DA (10 μM in HBSS, 0.5% DMSO(v/v)) and were incubated at 37 °C in 5% CO_2 and high humidity for 30 min. The cells were washed twice with PBS (200 μL) to remove DCFH-DA. The cells were then kept in Hanks'Balanced Salt Solution (HBSS), and Au and FeAu NPs dissolved in PBS at different concentration were added to

the cells. The fluorescence spectrum was recorded via excitation at 480 nm and emission at 538 nm on a Fluorescence Plate Reader (TECAN). Each point was taken on triplicates. The control cells were used as background to subtract the ROS content due to natural formation of ROS.

4.3 Results and Discussion:

Dimercapto succinic acid (DMSA) was added in excess with 0. 1mg TCEP (*tris*(2-carboxyethyl)phosphine) and 2mg Sodium Bicarbonate with 0.5ml dimethyl sulfoxide (DMSO). TCEP will break disulfide bonds formed in DMSA. Less DMSO is good for the reaction as higher amount causes aggregation of NPs due to insolubility. Under nitrogen atmosphere, reactants were shaken at RT for 12 hours.

After, 12 hr, NPs were precipitated in hexane, and then dissolved in DI water. NPs without TCEP and sodium bicarbonate, didn't dissolve in water. Proving that, small sodium bicarbonate is necessary to remove proton from thiol.

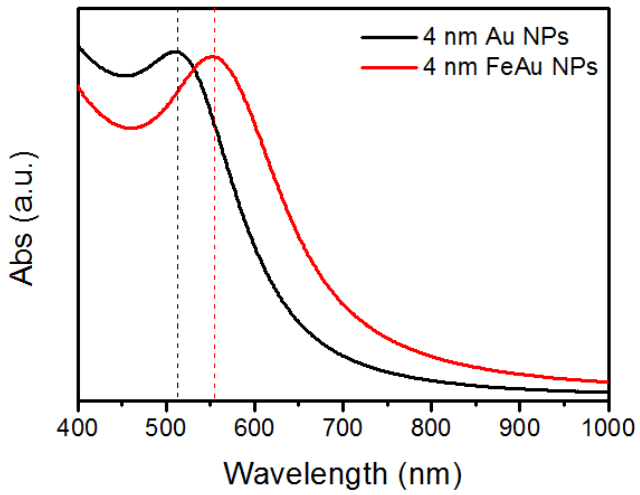

Figure 51: Optical Property of FeAu NPs. As-synthesized 4 nm Au in hexane showing peak at 512 nm and 4 nm FeAu alloy in hexane is red-shifted to 552 nm

The FeAu alloy NPs possesses optical property with absorbance peak at 552nm. This property of FeAu alloy can be further used in different bio applications. The FeAu alloy NPs are characteristically similar to that of bcc-FePt so we tested whether these NPs would also be therapeutic. The preliminary test of Fe release from FeAu-DSPE-PEG_{2000}-COOH construct formed by ligand addition did not show any Fe release. We believed that the alloy surface was too crowded by ligands and prevented the Fe to release.

The surface functionalization of FeAu NPs was carried out by ligand exchange using dimercaptosuccinic acid (DMSA) which binds to Au surface on thiol side, while the hydrophilic carboxylic group is exposed on the outside as shown in schematic below Figure 52. The carboxylic group provides stability to the nanoparticles and can be further modified to attach the functional groups such as small targeting ligands, drugs, peptides.

4.3.1 FeAu alloy NPs

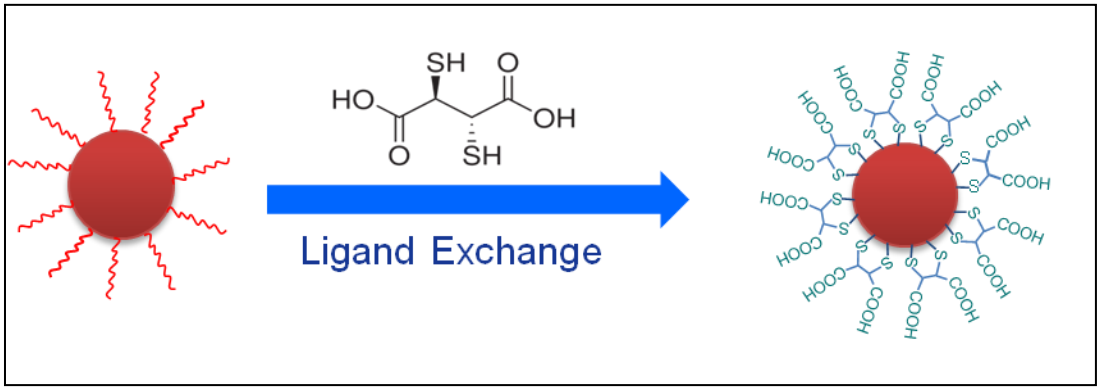

Figure 52: Schematic illustration of the surface functionalization of the as-synthesized FeAu alloy using DMSA to make them water soluble.

4.3.2 Stability of FeAu NPs:

FeAu NPs functionalized with Dimercaptosuccinic acid (DMSA) were purified using 30,000 MWCO dialysis tubing and then PD-10 desalting column to remove extra ligands and finally 0.22um sterile filter was used to remove any aggregates and sterilize for cellular experiments. First, FeAu-DMSA nanoparticle stability was examined carefully as it is very important to be stable in biological medium for the therapeutic application.

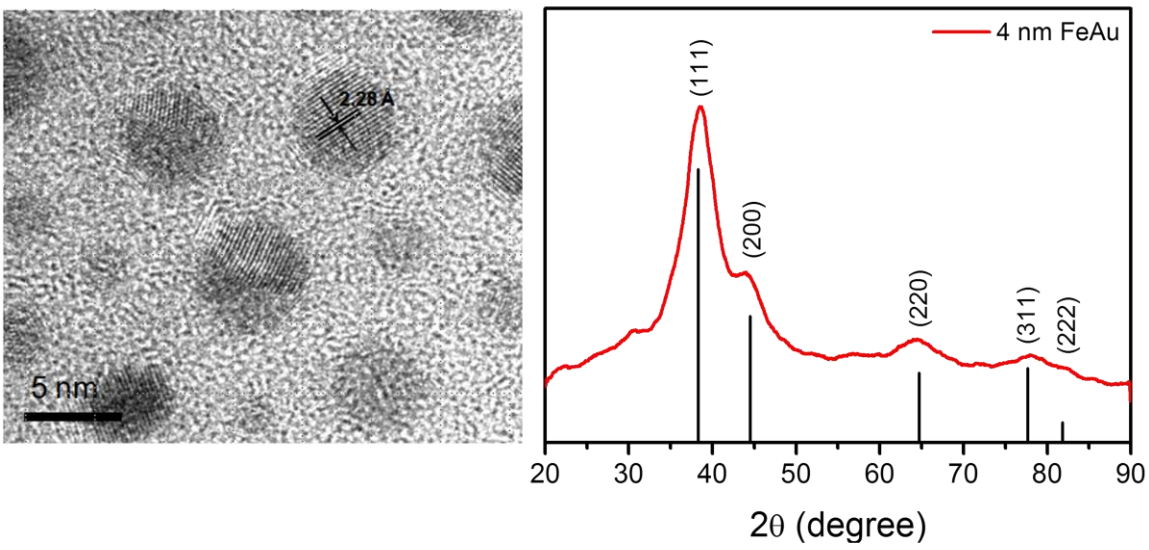

Figure 53: FeAu alloy characterization using HRTEM, FeAu NPs lattice spacing of (111) 2.28 Å, and XRD pattern of FeAu alloys

FeAu alloys were characterized by the lattice spacing of 2.28 Å, compared to Au lattice spacing of (111) 2.35 Å further indicate the alloying of Fe into Au, XRD pattern of FeAu alloys are right shifted than that of Au NPs.

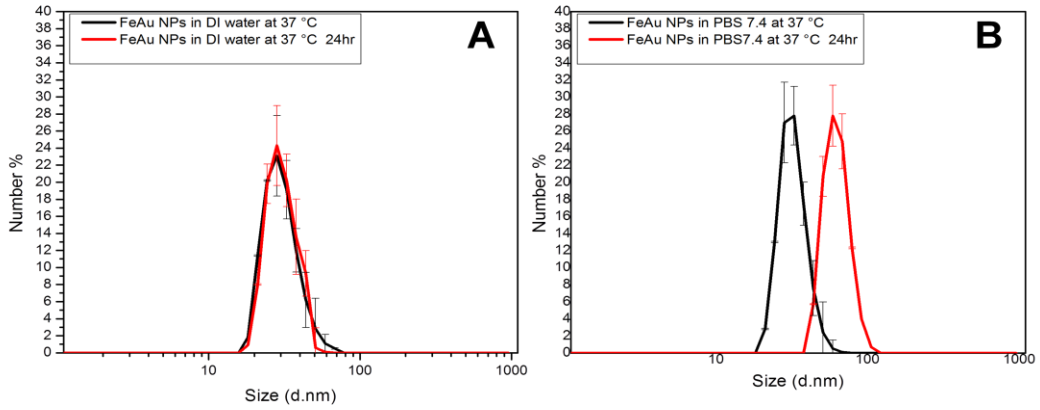

Figure 54: Stability of FeAu alloy NPs in A) DI water B) PBS 7.4 at 37 ºC. 0.08 mg/ml of Fe was incubated with 1ml of the medium

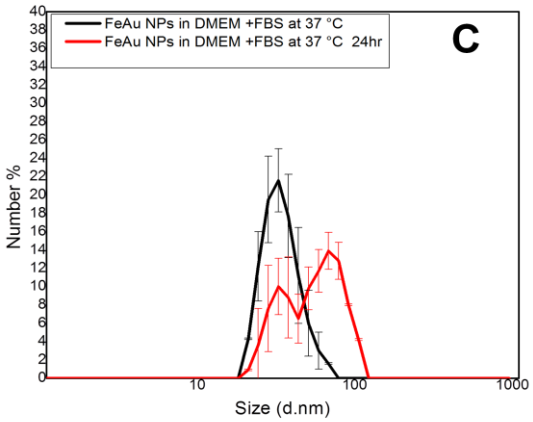

Figure 55: Stability of FeAu alloy NPs in C) DMEM with 10% FBS at 37 ºC for 24 hr. 0.08 mg/ml of Fe was incubated with 1ml of the medium

Zeta Potential (mV)	Size (d.nm)
-43.7	24.363±5

Measured at 25°C in PBS 8.0

According to the DLS Figure 54 A and B, FeAu NPs are stable in DI water and PBS 1X pH 7.4 for 24h at 37°C. It is also observed that FeAu NPs stored at 4°C are stable for a long time as well. However, we observe slight increase in hydrodynamic sizes with FeAu NPs in DMEM+10%FBS Figure 55C. The increase might be due to the serum which can be attach to the nanoparticles.

4.3.3 Stability of Au NPs:

The Au Nps stabilized by DMSA are stable in water for several days at 37 ºC. The NPs were left at 37 ºC water bath and gently shaken before measuring DLS with the same sample. Au nanoparticles have been shown to be quite stable using DMSA ligand and used in photoluminesce and other optical properties [76]. In Figure 56, DLS of Au-DMSA show nanoparticle stability at RT, no change in hydrodynamic size is observed. These particles can be refrigerated and used for a longer time.

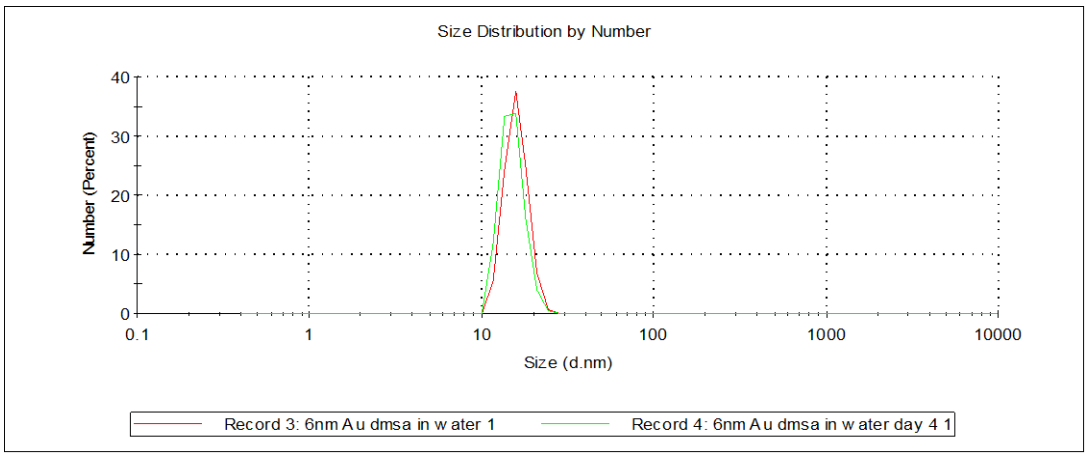

Figure 56: Stability of Au-DMSA NPs in DI water kept at RT for 4 days.

4.3.4 Fe release from the FeAu alloy nanoparticles

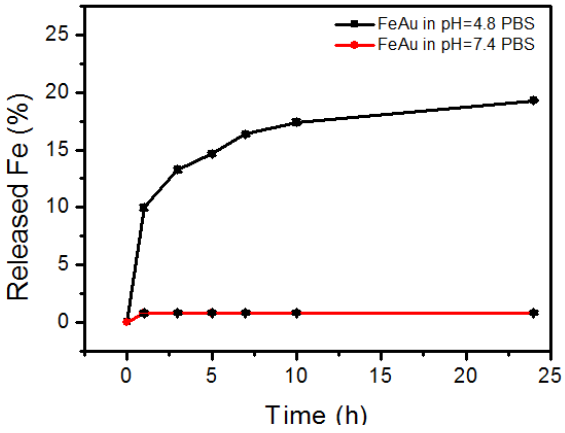

Figure 57: Fe Release from FeAu-DMSA NPs at low pH 4.8 and pH 7.4 at different time interval

The Fe released was measured by ICP-AES at different time interval. The result was consistent with the initial and final ratio of FeAu and also the released Fe measured in the PBS solution. At lower pH 4.5 there is higher release of Fe. In a further time study, it was found that the 44% Fe was released at 37°C.

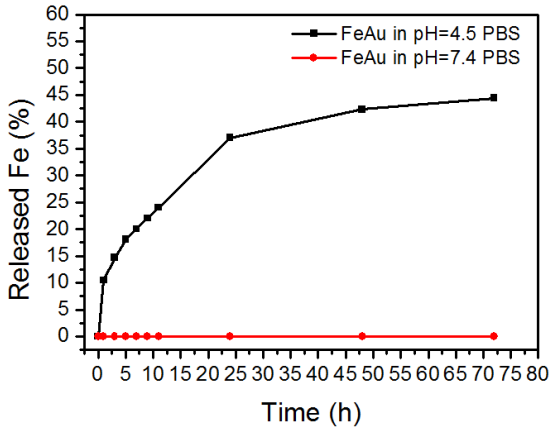

Figure 58 Fe Release from FeAu-DMSA NPs at low pH 4.5 and pH 7.4 at different time interval upto 74 hrs.

4.4 MTS Assay to measure cell viability:

MTS (3-(4,5-dimethylthiazol-2-yl)-5-(3-carboxymethoxyphenyl)-2-(4-sulfophenyl)-2H-tetrazolium), in the presence of cellular reductase, phenazine methosulfate (PMS), produces a formazan product that has an absorbance maximum at 490-500 nm in phosphate-buffered saline as shown below in figure 58. This reduction is presumably accomplished by NADPH or NADH produced by dehydrogenase enzymes in metabolically active cells. Thus, the quantity of formazan product is directly proportional to the number of living cells in culture measured at 490nm absorbance.

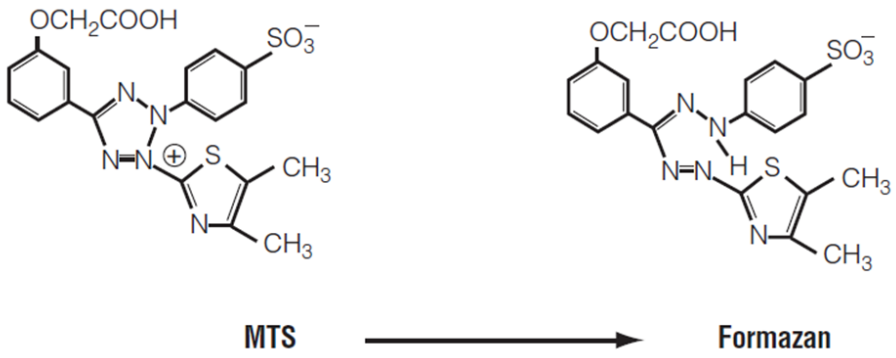

Figure 59: Structures of MTS tetrazolium and its formazan product which absorbs light at 490nm and thus be quantified

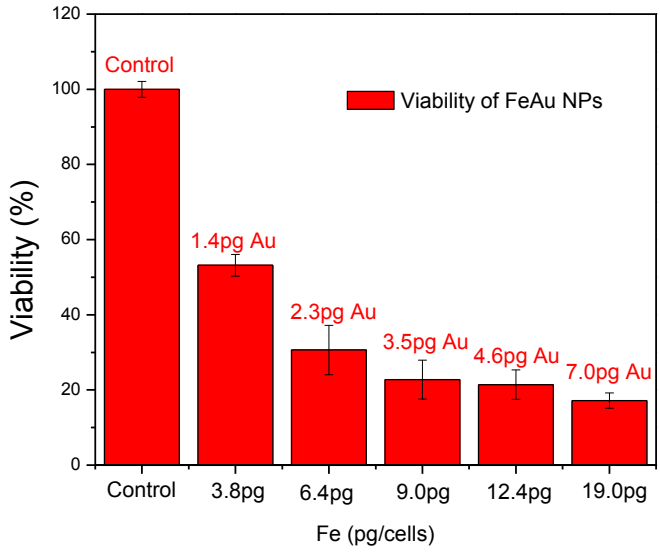

Figure 60: Viability of FeAu NPs: MTS cellular viability A549 lung cancer cell lines incubated with FeAu-DMSA NPs at different Fe concentrations at 37°C for 24 h. FeAu alloy show cytotoxicity at 3.8pg/cell

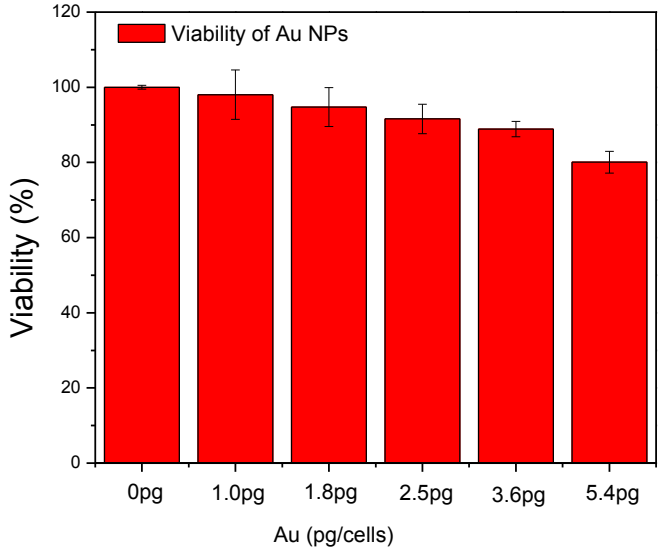

Figure 61: MTS cellular viability A549 lung cancer cell lines incubated with Au-DMSA NPs at different iron concentrations at 37ºC for 24 h. Au-DMSA show some cytotoxicity at the highest concentration of 5.4pg/cell.

The MTS assays were performed on A549, lung carcinoma cells plated at 40,000 cells/well. For a positive control, Au-DMSA NPs are used as control for Fe release. The cells were treated with similar Gold concentration. The FeAu show 50% cytotoxicity at 3.8 pg/cell Fe (1.4pg/cell Au) and the cytotoxicity is increased with increasing concentration. Almost 80% cells are dead at 19.0 pg/cell Fe (7.0 pg Au) concentration.

Compared to the FePt NPs which have IC_{50} of 1.25 ug Fe/ml [73], FeAu alloy NPs have IC_{50} of 3.8 pg/ml. This value show extreme potential of therapeutic ability of our FeAu alloy NPs.

4.4.1 ROS Assay: ROS Formation.

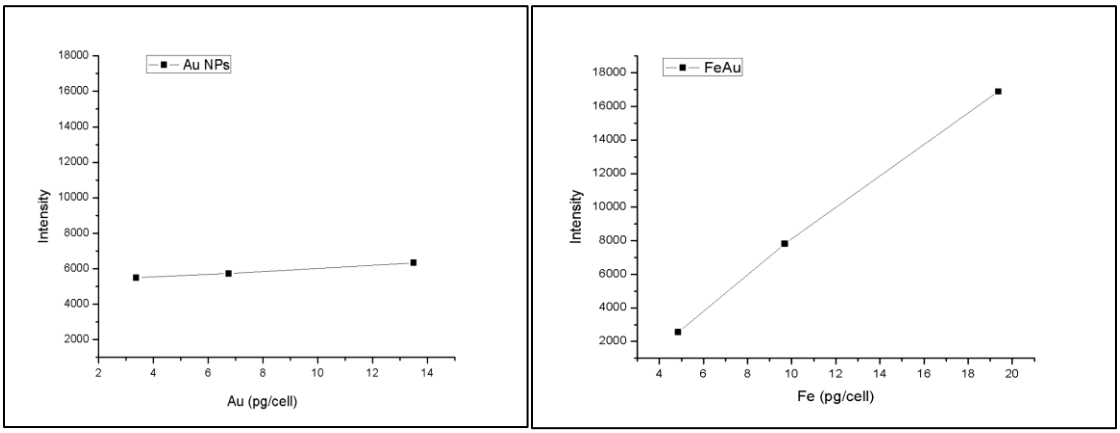

Figure 62: Fluorescence Intensity from DCFH-DA labeled A549 cells with Au NPs as control (left) and FeAu NPs at (5, 10 and 20 pg/cell concentration). The ROS intensity increased significantly with the increase in FeAu NP concentration.

The intensity data was normalized against background cell control and nanoparticle control. Owner's manuals guidelines were followed to generate H_2O_2 positive control, cell control and nanoparticle control. Briefly, A549 cells plated at 20,000 cells per well were treated with DCFH-DA then Au and FeAu NPs were added. Each point was taken on triplicates.

The cells were treated with NPs for 24 hr. As we compare the MTS assay the concentration of cells that are needed to kill the cells is at 3.8pg/cells. The intensity is increased till 2.0pg/cell and after that the intensity is lowered. The cells died and were washed away during the washing process so the fluorescent compound washed away with it. The decrease in intensity is a result of cell toxicity over 24 hr period of time. From the MTS assay we see that 50% of cells are dead at the concentration of 3.8pg/cells.

4.5 Conclusion:

Au and Ag nanostructures have attracted much interest in biomedicine due to their unique properties, including large optical field enhancements resulting in the strong scattering and absorption of light. The enhancement in the optical and photothermal properties of noble metal nanoparticles arises from resonant oscillation of their free electrons in the presence of light, also known as localized surface plasmon resonance (LSPR). The plasmon resonance can either radiate light (Mie scattering), a process that finds great utility in optical and imaging fields, or be rapidly converted to heat (absorption); the latter mechanism of dissipation has opened up applications in several new areas commonly known as photothermal therapy[77, 78].

FeAu NPs are highly desirable due to their optical property similar to Au NPs which can be used in optical imaging. In this study, we have showed the therapeutic property of FeAu alloy NPs. FeAu NPs released Fe at low pH and 37ºC environment but are inert and stable at normal physiological conditions. The H_2O_2 decomposition and ROS formation were toxic to A439 lung carcinoma cells. Au NPs were used as a control which didn't show toxicity. The toxicity caused by Fe release was further proved by the STA-342-ROS assay, which captures the ROS formed in the Fenton reaction. These NPs show great potential to be used as therapeutics. These NPs can be further modified with targeting ligands to target specific cancer tissues. An external magnet can be used to guide and accumulate NPs in the desired area. Furthermore, the optical property of FeAu NPs can be used to perform optical imaging to guide cancer therapy and monitor the progress in real-time.

Chapter 5 Magnetic Nanoparticles Applications in Detection

5.1 Introduction:

Superparamagnetic iron oxide nanoparticles (SPIONs) have been great diagnostic tool in the field of biomedicine. SPIONs are also found to be sensitive for magnetoresistive (MR) sensor based detection as they reach magnetic saturation in the presence of external magnetic field. Magnetoresistive (MR) based sensors principle is to attach magnetic nanoparticles to the analyte molecules and then use the MR sensor to detect the stray field caused by NPs for detection. There are two types of MR sensor studied; GMR and TMR. GMR is the giant magnetoresistance. Two ferromagnetic (FM) layers are separated by a nonmagnetic (NM) layer. The conduction of electron depends on the relative magnetization of the FM layers. This gives rise to the change of magnetoresistance (MR) called MR ratio. In this study, we are using Magnetic Tunnel Junction (MTJ) which works on Tunneling magnetoresistance (TMR) effect. In TMR, two ferromagnetic (FM) layers are separated by a thin insulating layer. When the insulating layer is very thin <1nm, electrons can tunnel through. Tunneling current depends on the magnetization direction of the FM layers. When the magnetization is parallel, more electrons tunnel through whereas less electron tunnel through when the magnetization direction is anti-parallel.

Magnetic NPs create a fringe field, which is strong enough to influence the magnetization direction of the top FM layer of a TMR sensor. This creates change in the number of electrons tunnel through which is turns causes change in current and subsequently to resistance which can then be monitored. The change in resistance is directly related to the magnetization value of the NPs, the magnetic field applied to the NPs, and the

distance between the NP and the FM layer. For a typical MR sensor, magnetic field is around 50-100 Oe with a current of few tens of μA up to 1 mA. To achieve ultra-high sensitivity, ideal NP probes should be superparamagnetic NPs with high magnetic moment and large susceptibility so that they have no effect on the sensor without an external field but can be magnetized in a small magnetic field. Additionally, the NPs should be uniform in shape, size and properties so that the modification with biomolecule can be controlled and the limit of detection of biomolecule can be quantified properly.

DNA labeled 8nm, 16nm Fe_3O_4 NPs have already been successfully detected by MgO-based MTJs with a DNA detection limit as low as 2.5μm [79, 80]. MIONs with high magnetization are preferred to the bulk magnetic labels, as the size matches in range with bio-markers such as protein, antigen, lectins or virus. For the optimal detection, MIONs should be uniform in size and shape, be able to easily magnetize with high saturation moment and have biological surface functionalization that is selective to the biological probe [81-83].

Using, MTJ chip various substrates such as antigens, receptors or metals can be detected at the same time, a single chip can be modified with different receptors. Gaster et.al. showed several antigen detection using a single sensor. Lung cancer biomarker (interleukin-6) was successfully detected using GMR sensor and FeCo nanoparticles. Method based on enzyme-linked immunosorbent assay (ELISA), antibody sandwich method, was found to be 13 times more sensitive than the Il-6 ELISA assay. In the figure

below, the same amount of capture antibody and detection antibody-modified magnetic nanoparticles were applied to each sensors with varied numbers of IL-6 molecules.

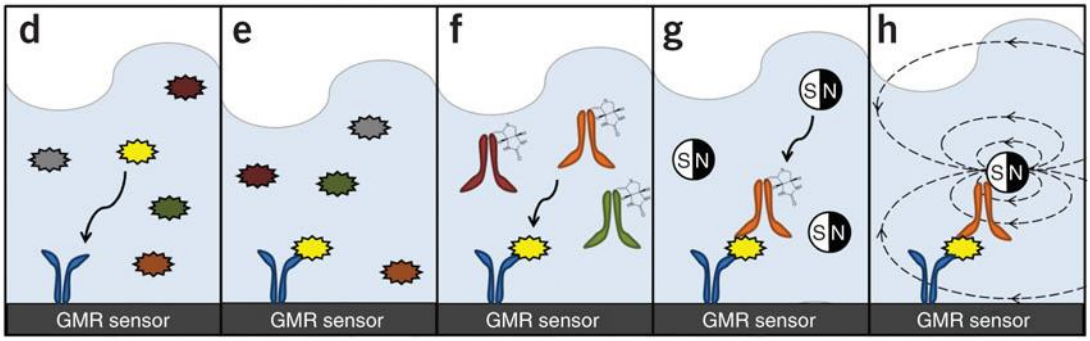

Figure 63: Schematic illustration of ELISA based GMR sensor using Magnetic Nanoparticles. Reprinted with permission from Ref [84]

Matrix Protein Assay

Different antibodies to a representative tumor markers such as lactoferrin, survivin, carcinoembryonic antigen (CEA), vascular endothelial growth factor (VEGF), epithelial cell adhesion molecule (EpCAM), granulocyte colony–stimulating factor (G-CSF), tumor necrosis factor-α (TNF-α) and eotaxin were functionalized on a magnetosensor, making up 40 sensors per reaction well. Secondary antibodies were functionalized with biotin. Whereas the commercially available 10nm Fe_2O_3 in dextran was labeled with streptavidin. Then, the signals generated by magnetic NPs binding to the secondary antibody were studied in different conditions, in PBS (pH 7.4), mouse serum, lysis buffer (pH 8.0), human urine (pH 5.15), human saliva and human serum. Harsh conditions and different pH had no effect on background signal. They demonstrated lower limit of detection around 1–5 pM (10-12) which are over 1,000 times more sensitive than ELISA [85].

Commercially available bio-sensors lack the ability to detect range of analytes in different medium of sample (serum, urine, saliva) because of their differences in pH. The current bio-sensor system is more complicated by problems such as photobleaching and fluorescence quenching [84]. Curently, MTJ sensor with 1 picoTesla are under active research whereas GMR sensor with 1 nanoTesla are commercially available [86]. Thus MR sensor provides a high sensitive, low-cost, portable detection system without the limits of commercially available bio-sensors.

Our research focuses on the synthesis of SPIONs with high magnetic moment, high susceptibility and stability in biological applications. We functionalized SPIONs with ss-DNA with target specificity for lower detection limits and better sensitivity. Using the ss-DNA as an analyte, we designed a chip-based magnetoresistive (MR) sensor with the intent to detect low amounts of magnetic nanoparticles with the ability to discern molecular increments in concentration. High quality MIONs are used in conjunction with a sensitive MR sensor and have potential for molecular level detection.

Magnetic iron oxide nanoparticles are synthesized in several different ways with products ranging with different shapes and sizes and different magnetic moments. For the detection using sensor system, it is required that an individual nanoparticle has a higher magnetic moment [82, 87]. I synthesized bigger FeO nanoparticles which could then in turn be oxidized to Fe_3O_4. At first, DNA hybridization is accomplished to optimize the chemistry and surface functionalization then we applied MTJ to detect Mercury (Hg^{2+}) ion.

5.2 Methods and Characterization:

5.2.1 Synthesis and characterization of FeO Nanoparticles:

All the solvents and compounds were purchased from Sigma Aldrich and used as received. Briefly, 1.4 gram of $Fe(acac)_3$ was dissolved in 10 ml Oleylamine, 10 ml Oleic acid and 5 ml Octadecene in a four-necked flask. The mixture was then slowly heated to 120 °C and degassed for 2 h under Nitrogen gas to remove any moisture. Then, the temperature was heated to 220°C and kept at that 220°C for 30 min, 45 min, 1 hr depending on the size of desired NP. Followed by another increase in temperature to 300°C at 2°C/min or 1.5°C/min depending on the desired size and kept at 300°C for 30, 45 and 1 hr. The nanoparticles were cooled down to room temperature and then precipitated using 60ml ethanol. After centrifugation at 8000 rpm for 8 min, the product was redispersed in hexane in the presence of an extra drop of oleylamine washed with ethanol twice. The resultant product was dispersed in hexane and kept under N2.

5.2.2 Characterization:

Nanoparticles shape and size were characterized by transmission electron microscopy (TEM). TEM images are collected on a Philips EM 420 (120 kV) or a Philips FEI CM 20 (200 kV). HRTEM images are obtained with JEOL 2010 (200 kV). To prepare a sample for TEM analysis, one drop of diluted NPs in hexane is dried on a Formvar/carbon coated copper grid (Ted Pella, Inc., 01754-F). X-ray Diffraction (XRD) was used to characterize the FeO peaks and Fe_3O_4 peaks after oxidation in air. The XRD analysis were performed in a Bruker AXS D8-Advanced diffractometer with Cu Kα radiation (λ = 1.5418 Å).

5.2.3 Ligand Exchange: Modification of NPs with Dopamine-PEG 2000-COOH :

Briefly, 60 mg polyethylene glycol diacid (MW=2,000) was dissolved in 2 ml chloroform. 4 mg of 1-ethyl-3-(3-dimethylaminopropyl) carbodiimide hydrochloride (EDC) and 2 mg of N-Hydroxysuccinimide (NHS) were added into the solution and stirred for 30 min. Then, 4 mg of dopamine was added and the mixture wasstirred for 2 h. Finally, 10 mg dried NPs in 1 ml chloroform was added into the mixture.After shaking 24 h, the product was precipitated by 10 ml hexane and dispersed in DI water. Particles were dialysed in 100K dialysis tubing for 24 h with change in water twice. DLS was used to characterize the hydrodynamic size of the modified nanoparticles. Fe concentration was measured using ICP-AES analysis.

5.2.4 Iron Oxide Nanoparticle modification with complementary ss-DNA

Dop-PEG_{2000}-COOH (Sigma Aldrich) was activated using EDC/NHS chemistry for 30 min and purified through PD-10 desalting column. Then, complementary ss-DNA (personalized base pairs 22bp from IDT-technologies) was added in MES or PBS buffer for 24 hr and shaken gently at RT. These DNA-modified nanoparticles were dialyzed in 100 MWCO dialysis tubing, which ensures unbound DNA to be removed. These modified nanoparticles were saved in PBS buffer at 4°C. UV-vis was used to characterize the DNA concentration and Fe concentration was measured using ICP-AES analysis.

5.2.5 Chip modification

MgO and AlOx based MTJ chips were obtained from University of Delaware. A chip was cut into pieces carefully into 1mm*1mm. Chip was washed with acetone and ethanol three times each to remove dirt. Then, 3ml of toluene, 1% trimethylamine and 10ul

silicate was added and incubated at 65°C for 24h for passivation. Carefully, chip was washed with toluene first and then ethanol to avoid damage to the MTJ chip surface area. Then, the gold surface of an chip was modified using 20mM Lipoic acid in ethanol for 24 hr. Chip was washed with ethanol for three times and then washed with DI water. Followed by an immersion into EDC/NHS solution for Lipoic acid activation for 30 min shaken gently avoiding any damage to fragile chips. Amine terminated ss-DNA (IDT technologies) 100ug/ml was added in MES or PBS buffer for 12 h and shaken gently at RT. Finally, the chip was washed with DI water three times and saved in pre-hybridization buffer at 4°C.

5.2.6 DNA Hybridization and SEM characterization

The MTJ chip was transferred from pre-hybridization buffer to hybridization buffer (Q-sense) and DNA-modified nanoparticles were added. The solution was warmed to 70°C slightly above the hybridization temperature and cooled down to RT. Later, the chip was washed 10X times with DI water. The chips were dried under vacuum or air to remove all moisture. The chips were attached to the SEM block using carbon tape. SEM images and quantitative elemental analyses of (Energy Dispersive X-ray Spectroscopy) EDS are obtained using a LEO 1560 SEM equipped with spatially resolved EDS.

5.3 Synthesis of FeO:

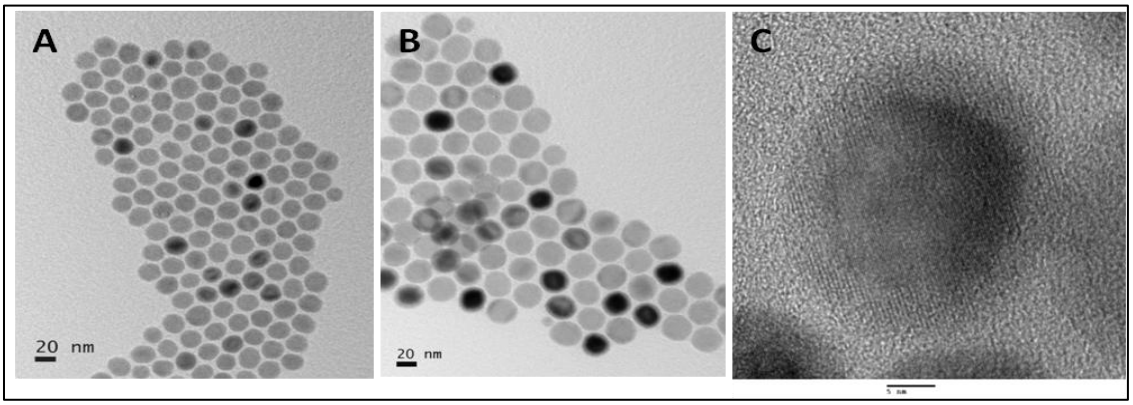

Figure 64: TEM of as-synthesized A) 20nm FeO NPs B) 35nm FeO NPs and C) HRTEM 20nm FeO NPs showing FeO/Fe_3O_4 core shell

The rate at which temperature was increased from 220 degrees to 300 degrees affected the nanoparticle shape and size. It was found that 1.5ºC/min produced bigger 30nm nanoparticles whereas 2.0ºC/min gave rise to smaller 20nm FeO nanoparticles.

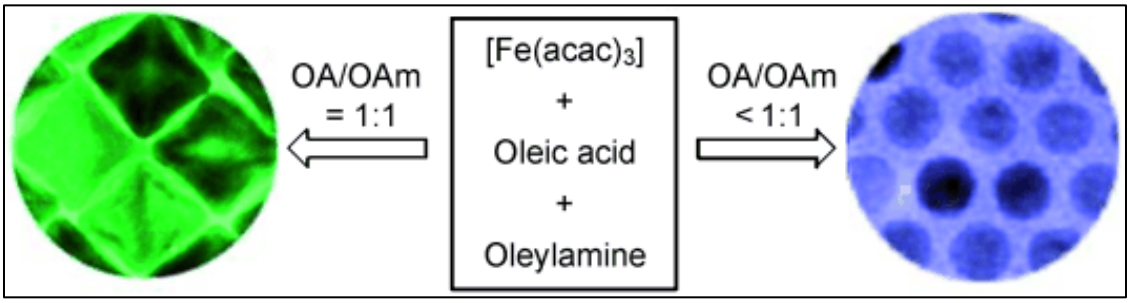

Figure 65: Schematic illustration of FeO synthesis showing the effect of surfactant ratio on the shape of nanoparticle. The 1:1 volume ratio of OA:OAm regulates growth in [100] direction over the [111] direction, a process leading to the formation of the truncated octahedron. Whereas, the excess of OAm regulates growth in all direction which led to form spherical shaped nanoparticles. Reprinted with permission from Ref. [88]

Modification of Synthesis:

FeO synthesis was slightly modified adding Octadecene as the solution, which changed the growth direction, forming hexagonal NPs. These NPs size could be controlled via increase in rate of temperature.

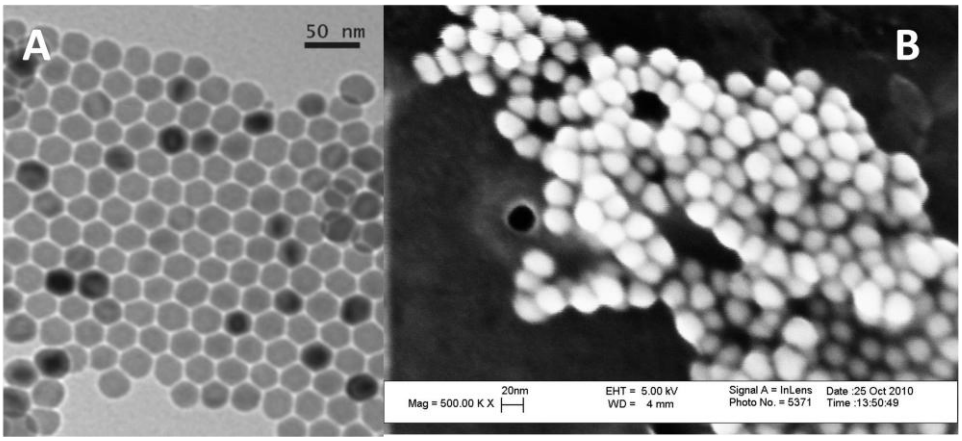

Figure 66: A) TEM and B) SEM of 20nm Hexagonal FeO Nanoparticles synthesized from extra Octadecene solvent.

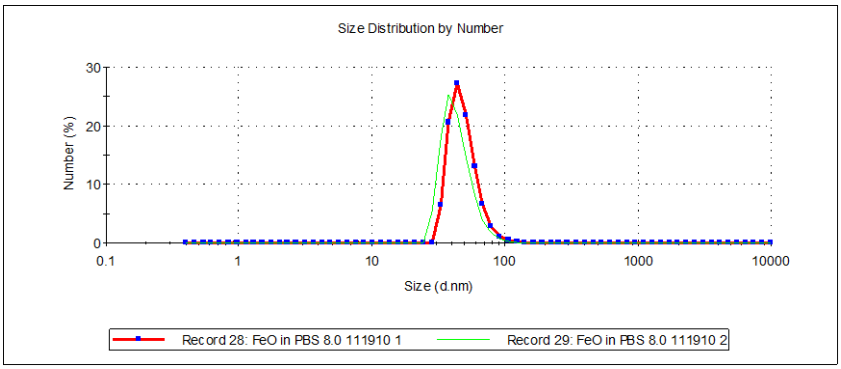

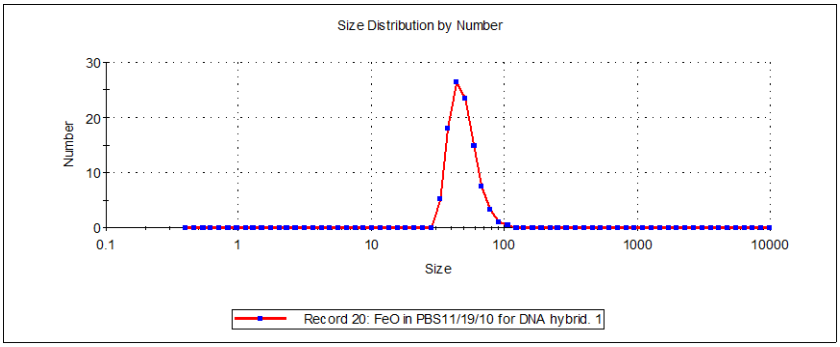

Figure 67: DLS measurement of FeO 25nm, PBS 8.0 for 72 days. FeO-Dop-PEG-COOH are highly stable.

FeO-Dop-PEG-COOH are highly stable due to their less magnetic moment and their high crystallinity.

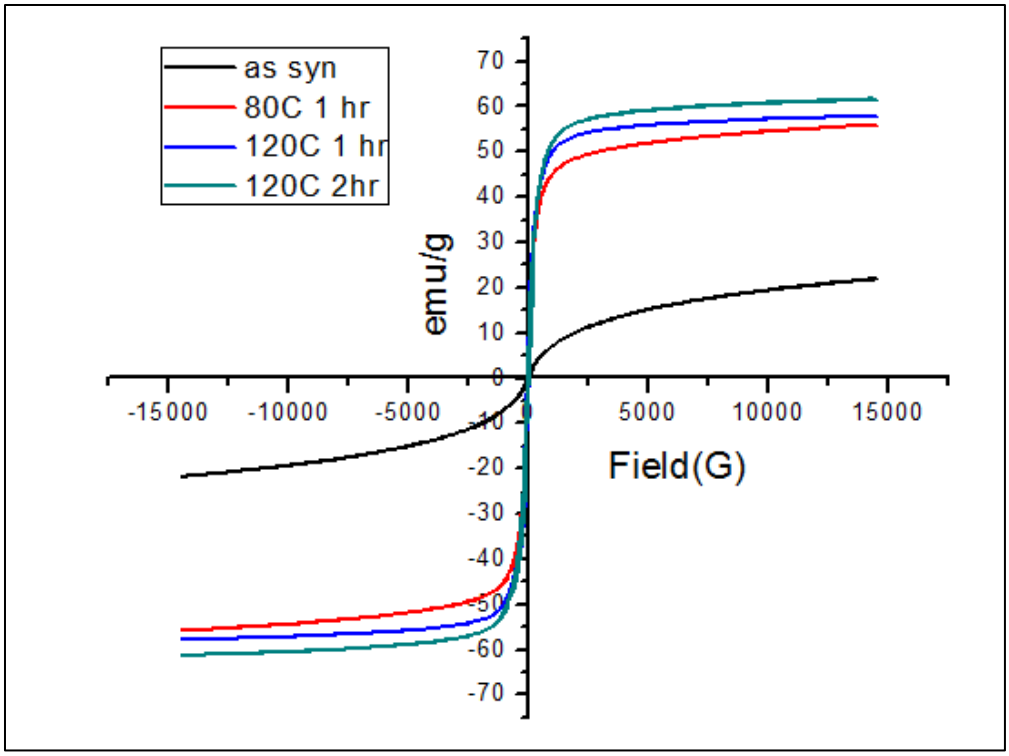

Figure 68: Hysteresis loops of FeO NPs oxidized. The FeO NPs have lower moment 20emu/g, however once oxidized the moment increases significantly reaching 60emu/g.

FeO NPs were synthesized using previously reported method with slight modification in the recipe (2). Octadecene solvent was added to the mixture to increase solubility of precursor, and thus changing the ratio between oleic acid and oleylamine, which might be the reason why the shape of the particles are spherical rather than the reported truncated octahedral. Figure 1 shows the TEM, SEM images with particles being 25-28 nm in size. When annealed in air for 2hr at 100°C, FeO nanoparticles are oxidized to Fe_3O_4. Hydrophobic FeO and Fe_3O_4 nanoparticles were functionalized with Dop-PEG_{3000}-COOH to make them water soluble[89][88]. FeO nanoparticles were stable for 72 days,

figure 69 whereas Fe_3O_4 nanoparticles were stable in DI water and PBS for 2 weeks, size measured using DLS. Fe_3O_4 have high magnetization so they aggregate after 2-3 weeks.

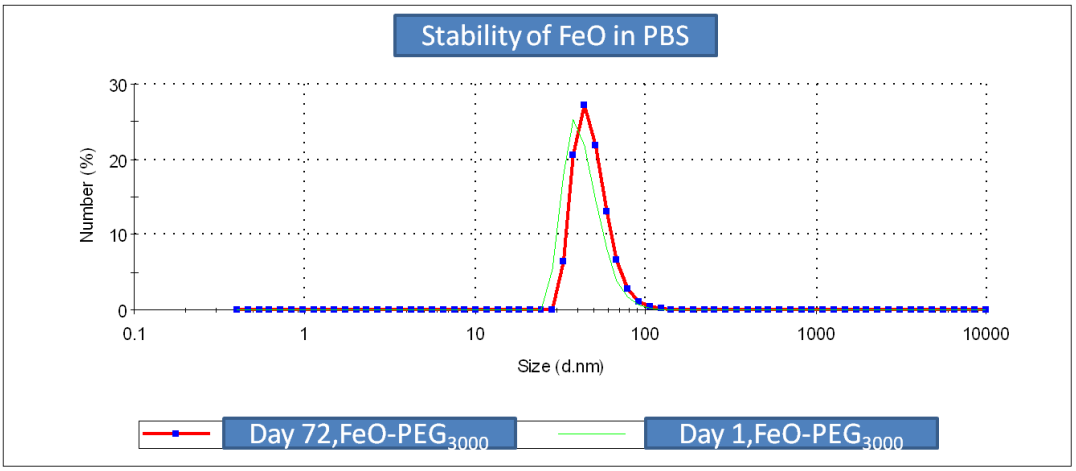

Figure 69: DLS measurement of 25nm FeO NPs in PBS 8.0

Depending on the rate at which temperature is increased from 220°C to 300°C, different size of FeO NPs are obtained. Similarly, the size of the NPs could be controlled by reaction time at 220°C from 30 min, 45 min to an hour giving different sizes of NPs ranging from 20nm to 40 nm.

We were able to modify the reaction conditions to obtain a better control on morphology and size of FeO NPs. These spherical NPs were stable in hexane, water and PBS buffer.

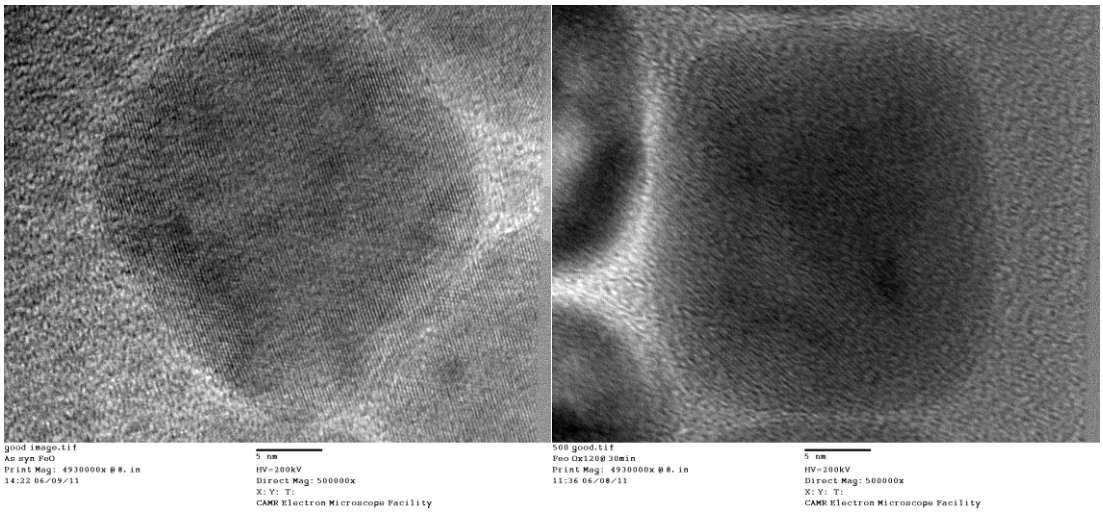

Figure 70: HRTEM of FeO NPs, As synthesized FeO and FeO oxidized for 2h at 120 C

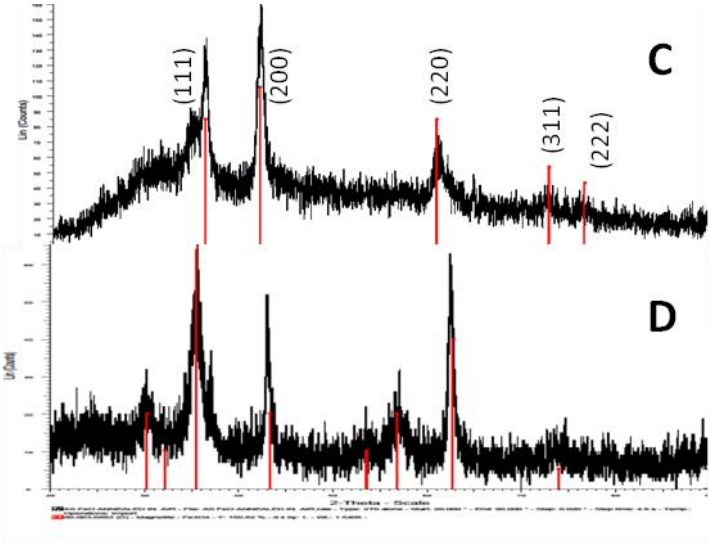

Figure 71: XRD of as –synthesized FeO and oxidized FeO showing peaks characteristics of FeO and Fe_3O_4 respectively

FeO can be oxidized in a controlled environment to get a core-shell FeO/Fe_3O_4 structure. At 120C for 2 hr in air, FeO is completely oxidized to Fe_3O_4 particles as observed by the

lattice fringes and XRD patterns. The (311), (222) and (220) peaks have disappeared from FeO structures and new characteristics peaks of Fe_3O_4 are formed.

5.4 Detection using MTJ chip

Iron oxide particles were synthesized using previously reported method with slight modification in the recipe [88]. Octadecene solvent was added to the mixture to increase solubility of precursor which might be the reason why the shape of the particles were spherical rather than the reported truncated octahedral. Figure 66 characterized by TEM and SEM being 25-28 nm in size. The XRD pattern matches with truncated octahedral FeO values as reported on literature, Figure 71. When annealed in air for 2hr at 100°C, FeO nanoparticles are oxidized to Fe_3O_4. Hydrophobic FeO and Fe_3O_4 nanoparticles were functionalized with Dop-PEG_{2000}-COOH to make them water soluble [89]. FeO nanoparticles were stable for 72 days as shown in Figure 69: DLS measurement of 25nm FeO NPs in PBS 8.0 whereas Fe_3O_4 nanoparticles were stable in DI water and PBS for 2 weeks measured using DLS. Fe_3O_4 have high magnetization so they aggregate after 2-3 weeks.

In collaboration with University of Delaware, we worked on DNA hybridization to detect MIONs. DNA hybridization using ssDNA is used as a model to increase the sensitivity of magnetoresistance (MR). The silica surface of chip was passivated using Silicate/Triethylamine so that ssDNA would not bind to silica surface. Au surface of chip was modified with Lipoic acid, two thiol groups makes strong binding to gold surface. EDC/NHS chemistry was used to couple amine terminated ssDNA. The Fe_3O_4-Dop-PEG_{2000}-COOH and ssDNA were coupled using EDC/NHS chemistry. Scanning Electron

Microscopy (SEM) and Energy-dispersive X-ray spectroscopy (EDX) were performed to detect MIONs.

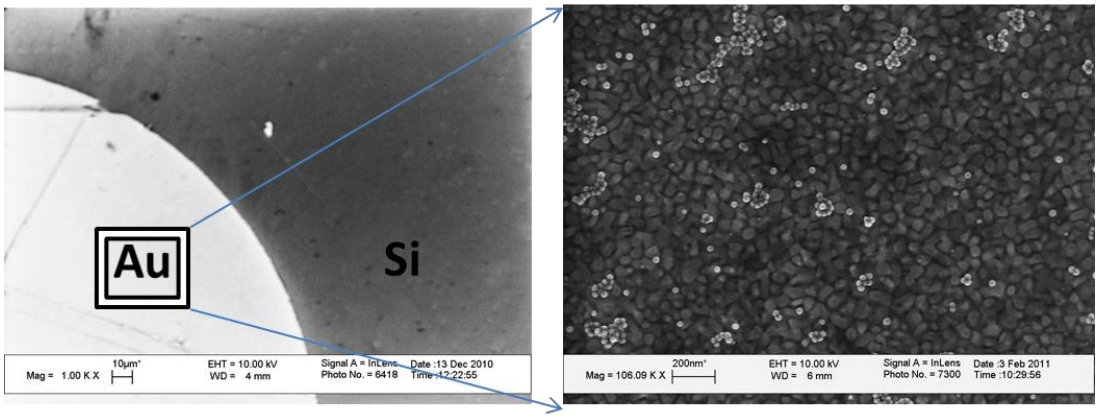

Figure 72 Au/Si Chip, DNA hybridization of ss-DNA to show FeO nanoparticles (white dots) in Au surface shown on right

We have used dummy chip wafer to replicate the Au/Si chemistry and have been able to specifically bind ss-DNA onto gold surface. However, careful consideration must be taken for non-specific binding and particle aggregation for Fe_3O_4 that can cause false positive during the detection. MIONs are seen in SEM of Au surface in figure 3.

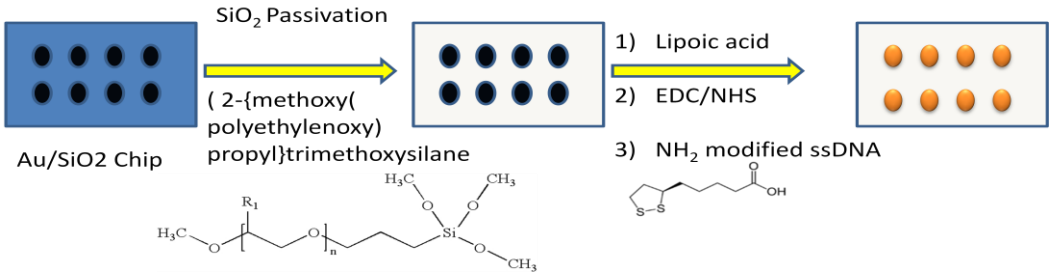

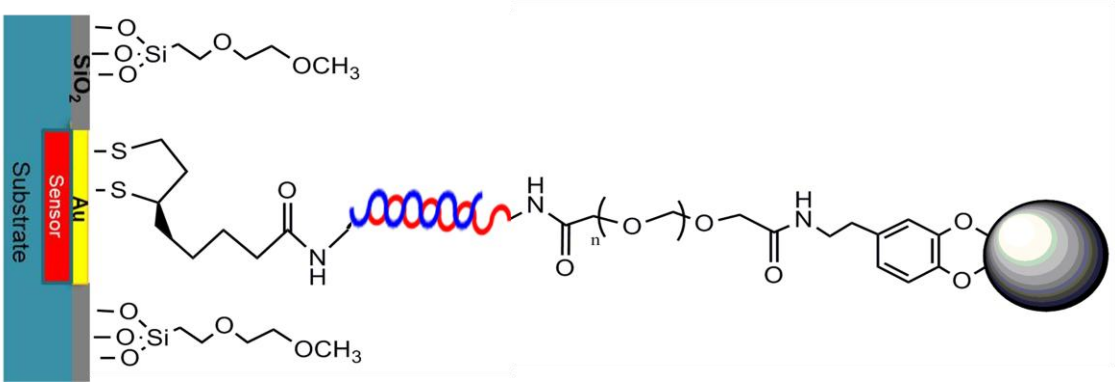

Figure 73: Schematic illustration of MTJ chip surface modification with complementary ss-DNA and it's binding to NP-Dop-PEG-ssDNA: Top view and side view

5.4.1 Specific binding :Au and SiO_2

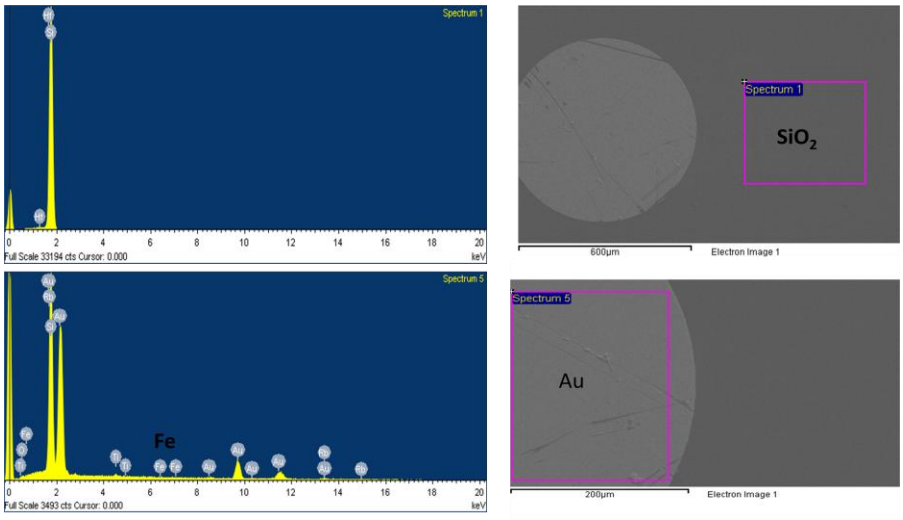

Figure 74 (A): Energy- dispersive X-ray spectroscopy of MTJ chip treated with FeO-DNA. Specific binding of NPs only in Au surface of MTJ region

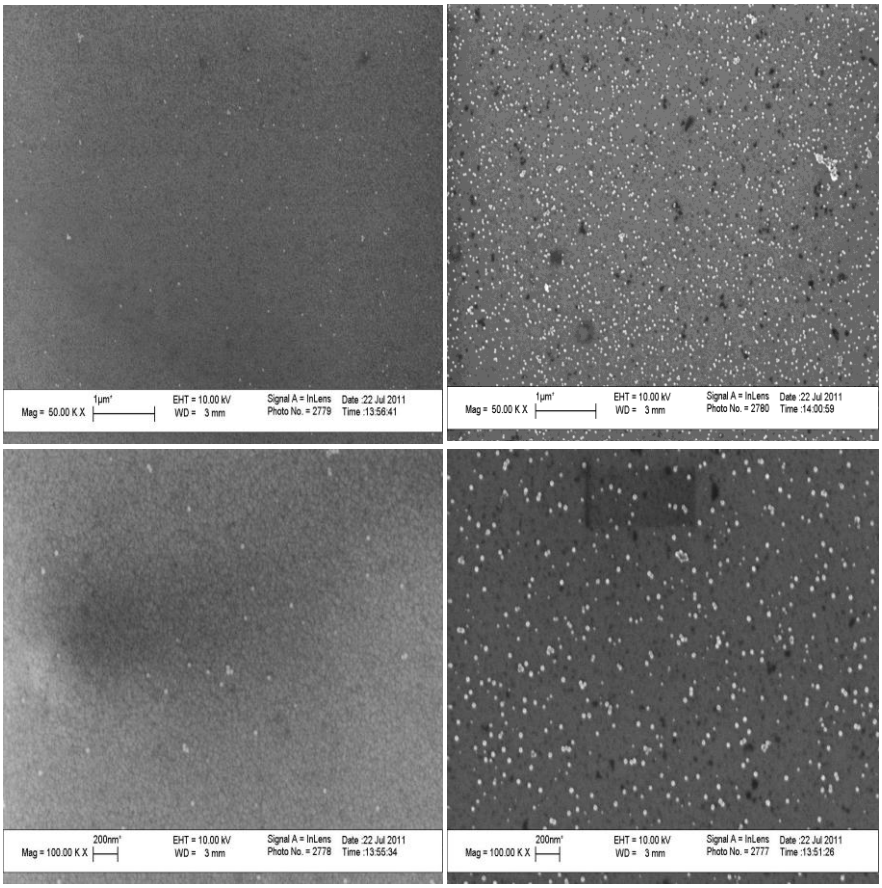

Figure 74 (B): SEM measurement after NPs attached on the AlOx junctions: FeO NPs visible in Gold and Al junctions.

AlOx based MTJ functionalization with DNA. The selective binding in Au part of MTJ reduces the noise caused by unspecific binding of NPs. SEM of Selective binding in different chips with changed protocol using lipoic acid to modify the Au surface first.

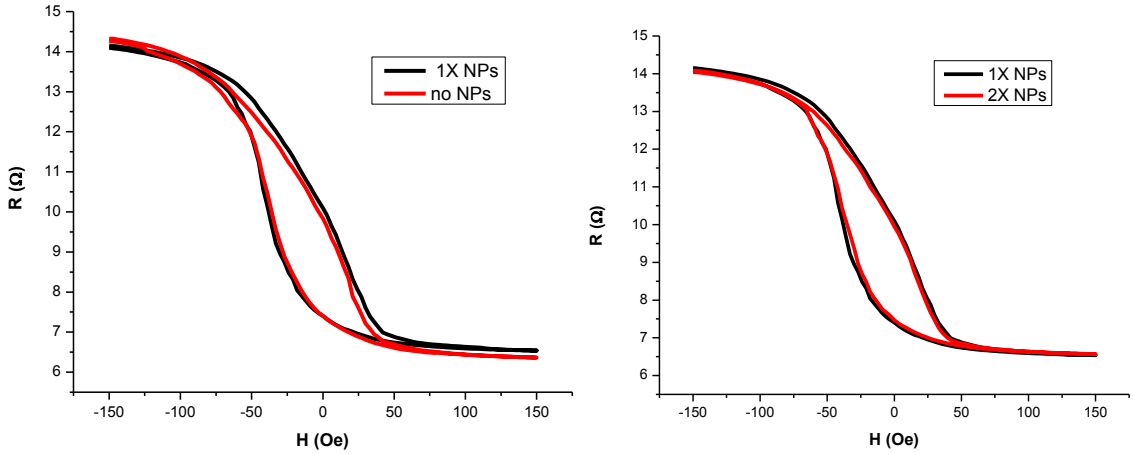

R-H loop of MgO based MTJ before and after DNA with 2X amount of NPs for Hybridization

R-H loop with recycled chip

These MTJ chips can be re-used by removing the previously used NPs via sonication at hgh temperature by dehybridization. However, the 1st reading can be taken as a baseline for the 2nd set of NP detection. This is very important feature for a chip based system as they can be re-used time and time again.

5.5 NP detection via change in resistance

Resistance is shifted to the right due to the presence of magnetic NPs on the chip. After vigorous washing, we see NPs on MTJ surface. Below, there is change in resistance but it is not uniform throughout all the field. Before NP attachment R-H curves were measured as a control. After NP functionalization R-H curves were measured on a same MTJ, so as to reduce the noise.

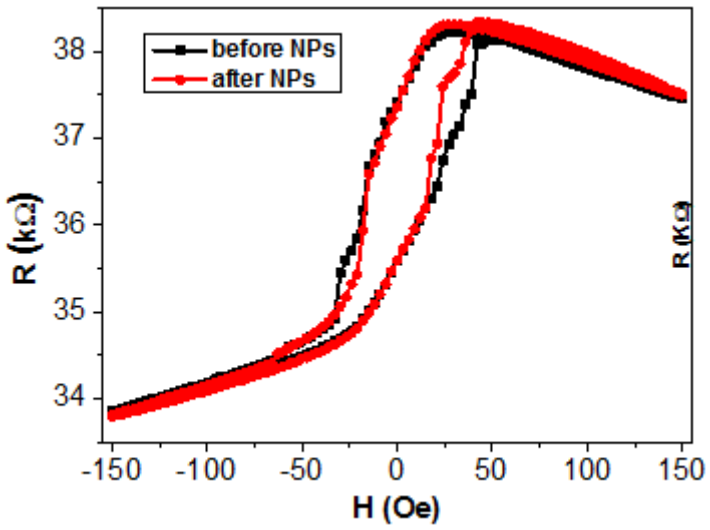

Figure 75: R-H curves of AlOx junctions before and after NPs. Slight shift in resistance to the right due to the presence of nanoparticles.

The transfer curves of NPs show the change in resistance and the shift of curve to the right. These small change in resistance is significant enough to detect the DNA analyte. Change in resistance depends on the magnetic field, with higher magnetic field applied we will be able to see larger ΔR. The resistance change can be further improved by applying higher external magnetic field.

5.6 Mercury Detection:

Superparamagnetic iron oxide nanoparticles (SPIONs) have been great diagnostic tool in the field of biomedicine. SPIONs are also found to be sensitive for magnetoresistive (MR) sensor based detection. Our research focuses on the synthesis of SPIONs with high magnetic moment, high susceptibility and stability in biological applications. We functionalize SPIONs with biomolecules that are target specific for lower detection limits with better sensitivity.

Despite several methods to detect mercuric (II) ion, there is a need to detect mercury in low levels efficiently. Mercury has been widely used in various fields such as medicine, cosmetics as well as gold and silver mining while it is also known as a widespread pollutant with conspicuous toxicity. As a neurotoxin, it can bring neurological problems such as cognitive and motion disorder, vision and hearing loss, sensation and memory damage [90]. It also can severely impact human heart, kidney, stomach, intestines and even cause death [91].

Mercury is a widespread pollutant with conspicuous toxicity that exists in a variety of forms. Hg^{2+} is most stable form of mercury that is water soluble, caustic and carcinogenic. Aquatic systems are constantly screened for Hg^{2+} for the safety of aquatically derived food supplies as EPA in drinking water : Maximum Contaminant Level (MCL) = 0.002 milligrams per Liter (mg/L) or 2 parts per billion (ppb). Several mercury detection methods based on organic flurophores, chromophores, cyclic voltammetry, proteins and colorimetric methods have been developed. However, these methods suffer from shortcomings like interference of other metal ions, poor solubility in aqueous solution and weak sensitivity[92].

Giant magnetoresistive (GMR) sensor provides a high sensitive, low-cost, portable detection system. We will devise a detection system based on iron oxide nanoparticles, DNA and sensor for higher sensitivity and no interference from other metals.

Mercury Detection using MR sensor:

Hg^{2+} ion can specifically bind to a mismatch pair of thymine bases in DNA and the binding is thermodynamically stable [93, 94].Using the thymine base mismatch property of DNA, we designed a chip-based magnetoresistive (MR) sensor with the intent to detect low amounts of mercury with the ability to discern molecular increments in concentration. High quality SPIONs are used in conjunction with a sensitive MR sensor and have potential for molecular level detection.

Magnetoresistive (MR) sensor provides a highly sensitive, low-cost, portable detection system. MR sensor is based on the property of a material to change the value of its electrical resistance when an external magnetic field is applied to it. In the presence of an external magnetic field, SPIONs reach magnetic saturation which creates a magnetic fringe which alters the magnetic field of FM layer in the sensor causing change in resistance (ΔR). DNA labeled 8nm, 16nm SPIONs have already been successfully detected by MgO-based MTJs with a DNA detection limit as low as 2.5μm [89, 95].

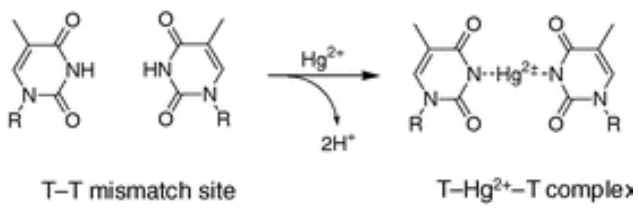

Mercury binding to thymine base pair mismatch

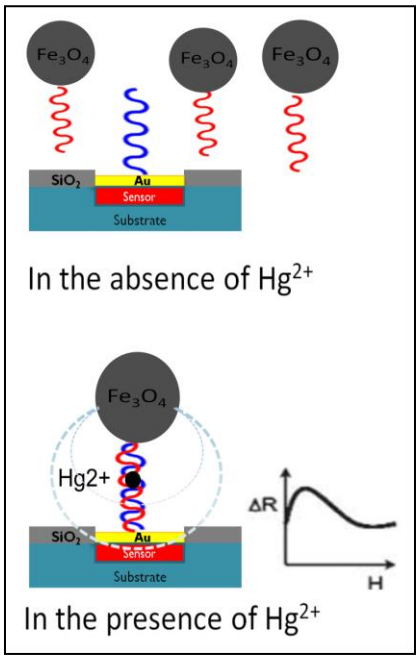

Figure 76: Schematic illustration of change in resistance due to the binding of Hg2+ causes MIONs to be closer to the sensor creating a fringe field which can be detected by the ΔR.

5.7 Design:

In the absence of Hg^{2+} : DNA hybridization will not occur. Any unspecific binding will be removed by heating at temperature higher than DNA dehybridization. DNA modified SPIONs will be washed away. There will be little to no change in MR signal in an MTJ chip.

In the presence of Hg^{2+} : DNA hybridization will occur due to strong binding of T-Hg^{2+}-T. Nanoparticles will not be washed, change in MR signal due to the fringe created by the SPIONs. Change in resistance will be directly related to the number of nanoparticles which depends on the concentration of Hg^{2+} .

On one hand, an alkylthiol-modified oligonucleotide (5'-HS-C_{10}-A_6TA_6-3') can be immobilized on Au chip surface through the formation of strong Au-S bond. On the other hand, dopamine terminated heterobifunctional PEG modified Fe_3O_4 (Figure 76) can react will NH_2-C_{10}-T_6TT_6-3' through EDAC/NHS reaction without interference of oligonucleotide sequence. When there is no Hg^{2+}, oligonucleotide NH2-C_{10}-T_6TT_6-3' modified nanoparticle probe was linked to 5'-HS-C_{10}-A_6TA_6-3' modified chip through forming a low melting temperature duplex with a single T-T unbinding. With Hg^{2+} in solution, the analyte Hg^{2+} can selectively bind to the T-T sites to form a T-T mismatched duplex which has a 10° higher melting temperature than T-T non-binding one[96]. By choosing a right experiment temperature, we can eliminate non-specific binding of nanoparticle probe to sensor surface without presence of Hg^{2+}.

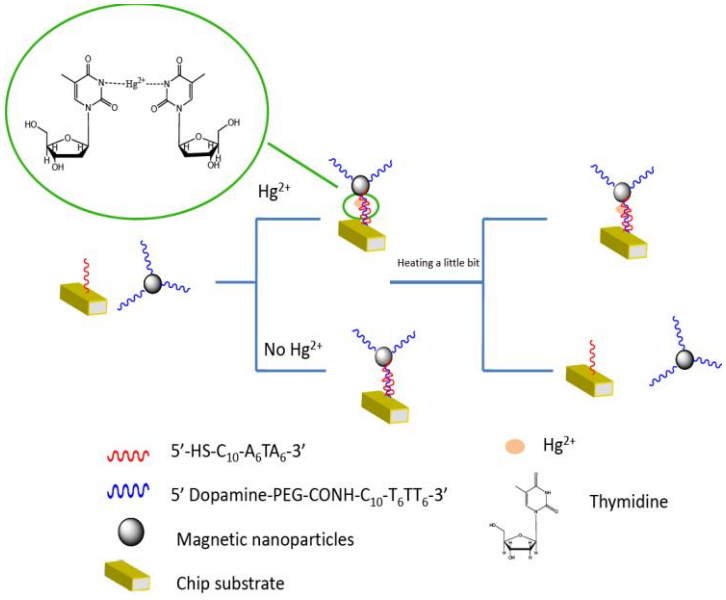

Figure 77: Schematic illustration of design of sensor surface

5.8 Results:

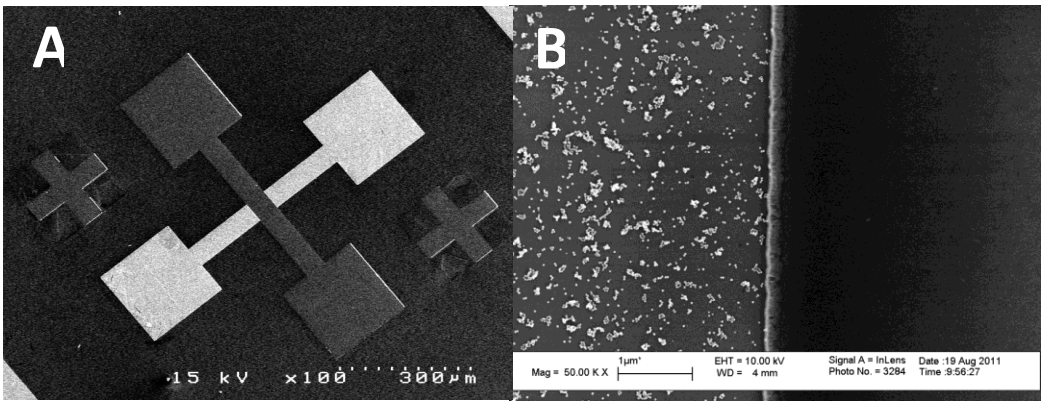

Figure 69: A) Chip surface showing Au and SiO_2 surface, B) Selective binding of MIONs to Au surface

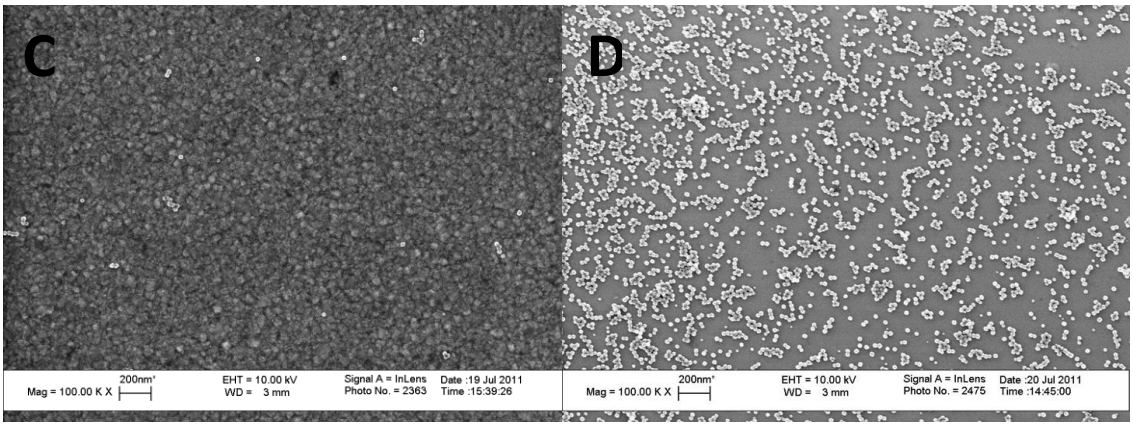

Figure 69: C) In the absence of Hg^{2+}, very few NPs are visible D) In the presence of 6.67uM Hg^{2+}

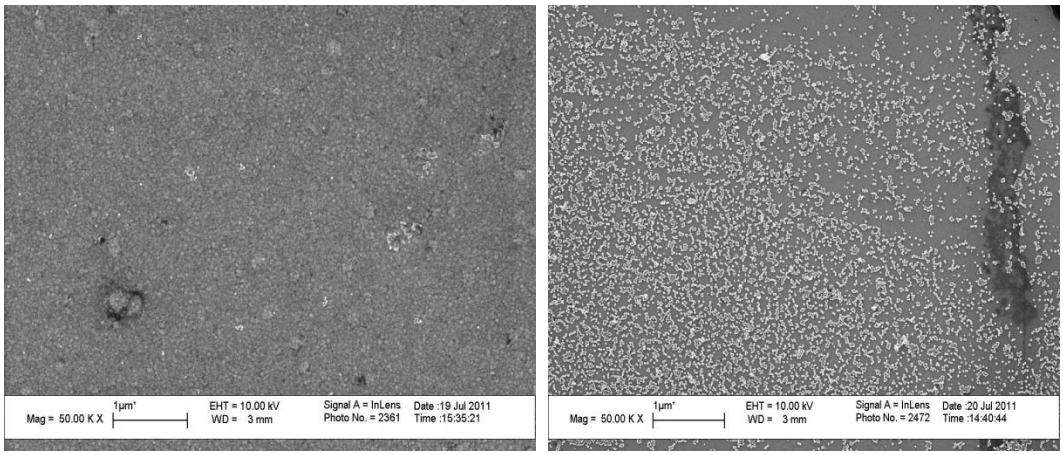

Figure 69: E) In the absence of Hg^{2+}, very few NPs are visible F) In the presence of 6.67uM Hg^{2+} lower magnification showing larger area surface.

SiO_2 surface of chip were passivated to reduce unspecific binding. SEM shows the selective binding of DNA and hence NPs on the gold surface. Energy- dispersive X-ray spectroscopy (EDX) confirmed wih no Fe peaks in the silica region, figure 74A. SEM images show that the DNA hybridization did not occur and NPs are washed away in the absence of Hg^{2+}. Some NPs visible in the absence are subtracted as noise in the MTJ measurement.

Detail experiments with heavy metals interference such as lead, cadmium, copper, etc and detection limit for mercury will be done via MR measurements. Design of the chips is underway so that we can reuse and measure different concentrations without the interference of external environmental factors.

Thymine residue of DNA itself could bend due to Hg^{2+} binding on the same oligonucleotide, causing the bend and thus restricting the FeO NPs to bind. Which could potentially cause problems in correctly identifying the mercury concentration thus we

modified the DNA sequence so that the oligonucleotides itself would not bind to mercury.

The DNA are hybridized first so that the chances of T-T binding on the same oligonucleotide is low. Then, the heat is increased above the melting temperature, so that the dehybridiation occurs. T-Hg2+-T binding is stronger so it will still be bound, when A-T bonds are broken.

5.8.1 Modified DNA sequence:

Oligonucleotide 5AmMC6/CCC CCC CCC CTA AAA ATA AAA AA-3' was modified to FeO Nanoparticles

5AmMC6/CCC CCC CCC CTT TTT TTT TTT TT- 3'' was modified on Au surface of MTJ chips

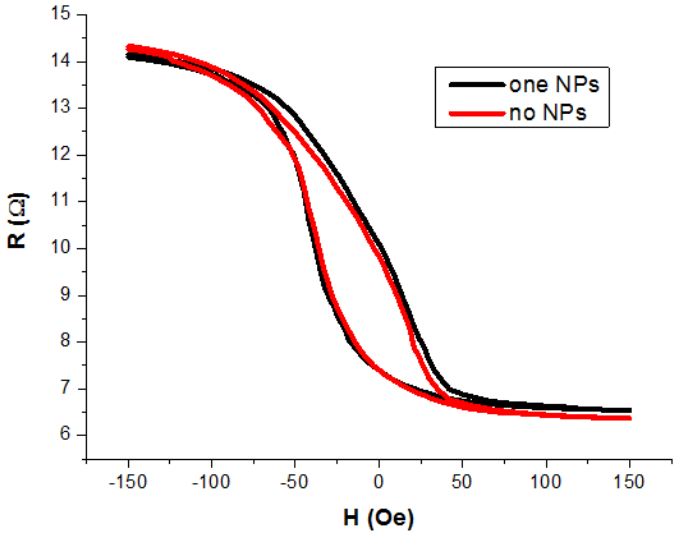

Figure 78: R-H curves of AlOx junctions before and after NPs attachment on MgO based MTJ

Nano-particles: $\mathbf{M}_{NP} = \beta\mathbf{H}$

$\Delta R = 0.2\ \Omega$

MR= 2.85%

The resistance is changed due to the presence of NPs in the MTJ sensor. Since, the magnetic moment of FeO NPs is 25emu/g at 10,000 Oe, and the external magnetic field applied is only 150 Oe, the maximum potential of FeO are not utilized. With, higher external magnetic field and Fe_3O_4 NPs with 80 emu/g it is possible to get a higher % in change in resistance.

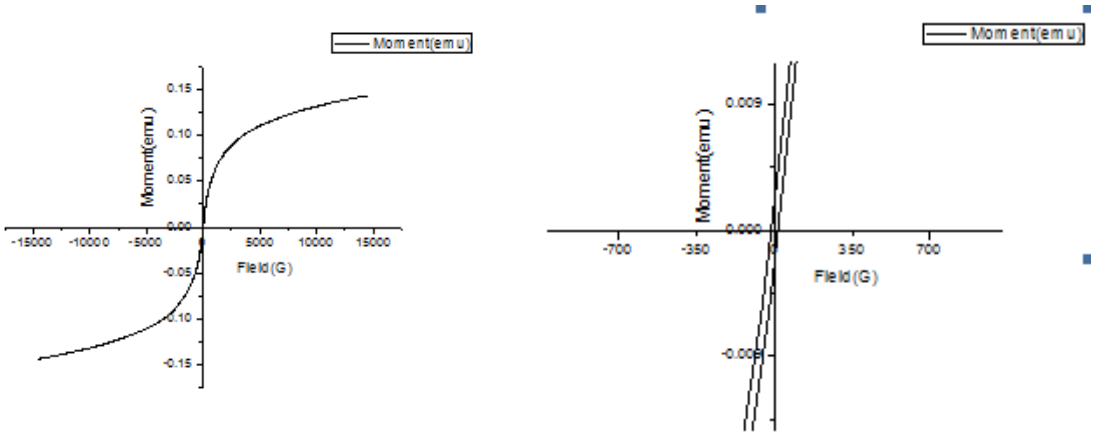

Increase in external magnetic field applied to the sensor can increase the higher % change. Value at 96.9261 G =0.01619 emu

Here, we show that the mercury ion can be detected using the MR sensor. The T-Hg^{2+}-T based DNA in conjuction with FeO NPs are able to be detected in SEM and MgO based MTJ sensor.

5.9 Diagnostics using Electrochemistry:

A quantitative detection method to detect lower levels of hydrogen peroxide (H_2O_2) in biological solutions is of broad interest in biology and biomedicine. H_2O_2 is produced by all cell oxidases and are diffused easily to the other organelles. If not regulated properly, excess H_2O_2 can lead to cell damage, ageing and cancer [97, 98].

Varieties of tumors are linked to overproduction of H_2O_2 due to the decreased level of catalse enzyme. One catalase enzyme can convert ~6 million molecules of hydrogen peroxide to water and oxygen each minute. Real time detection of H_2O_2 from live cells can provide an effective way to understand cellular functions, pathology and distinguish between the tumorigenic and non-tumorigenic cells.

These NP based detection limit is much lower compared to the HRP based colorimetric assay available on the market. Horseradish peroxide **(**HRP) is a protein-based enzyme found in horseradish and is extensively used as catalyst to facilitate the reduction of H_2O_2 [99]. However, these enzyme-based biosensors are difficult to apply in a real sensor device due to enzyme denaturation, complicated immobilization processes and limited stabilities [100, 101]. Electrochemical detection of H_2O_2 proves to be an effective method due to their high sensitivity, selectivity and low cost [102, 103]. Recent study demonstrated dumbbell-like PtPd-Fe_3O_4 NPs ability to detect and sense H_2O_2. Dumbbell-like Pt_xPd_{100-x}-Fe_3O_4 NPs were synthesized by controlled nucleation and growth of Fe over Pt_xPd_{100-x} NPs followed by air oxidation. These NPs show the Pt, Pd composition dependent catalysis for H_2O_2 reduction. Among different dumbbell NPs tested, $Pt_{48}Pd_{52}$-Fe_3O_4 NPs were the most active with a detection limit reaching 5 nM [104].

Nanoparticles of metal and metal oxide, for example Pt-based NPs and Mn oxides have been reported to show great potential for H_2O_2 detection due to a large surface-volume ratio and easily accessible active sites [105-107]. Most of the explored NPs with a low detection limit of H_2O_2 in nM region are Pt-based NPs. However, Pt-based nano-biosensor is far from optimized due to the scarcity and poor bio-compatibility of Pt which is undesirable in real-time H_2O_2 monitoring.

Herein, we synthesized MnAu based catalyst for the reduction of H_2O_2. The synthesis and electrochemical work was done by Huiyuan Zhu.

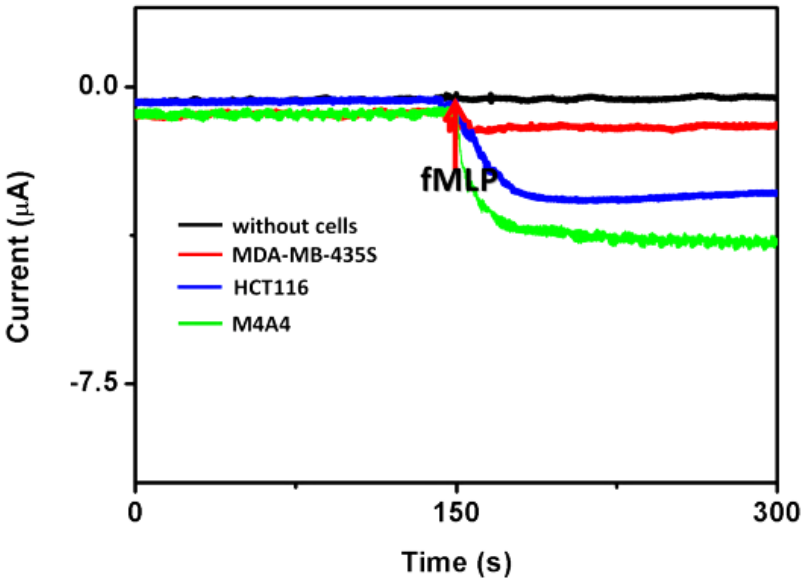

Figure 79: Amperometric response of $Mn_{56}Au_{44}$ modified electrode for the detection of H_2O_2 releasing from MAD-MB-435S cells (red line), HCT116 cells (blue line), M4A4 cells (green line) and blank without cells (black line).

MnAu NPs, with very high sensitivity even at low H_2O_2 concentration range, can be used to monitor the H_2O_2 change in the living cells. The real-time tracking of H_2O_2 in living cells was studied by adding N-formylmethionyl-leucyl-phenylalanine (fMLP) for H_2O_2 releasing from the cells [104, 108].[16,21] Upon the addition of 8 μM fMLP, a gradual

current response is observed at $Mn_{56}Au_{44}$ NP electrode and reaches a current plateau in presence of MDA-MB-435 (human breast melanoma cells), HCT116 (human colorectal carcinoma cells) and M4A4 cells (human epithelial cells) respectively. For the control experiment without cells, no current response is recorded upon injection of fMLP, suggesting the current change is due to H_2O_2 releasing from living cells (**Figure 80**). Furthermore, we can distinguish these cells by the current response. The current change for non-tumorigenic cells (MDA-MB-435S) is 0.3 μA and corresponds to 12 pM/cell; however, the tumorigenic cells reach a current change of 2.5 μA and 25 pM/cell for HCT116, and 3.3 μA and 33 pM/cell for M4A4, respectively (**Figure 80**). This is consistent to the fact that tumorigenic cells tends to generate more H_2O_2 due to the accelerated metabolism. This study proves that our $Mn_{56}Au_{44}$ NP electrode presents a sensitive probe for extracellular H_2O_2 detection.

5.10 References:

1. Jun, Y.W., J.S. Choi, and J. Cheon, *Heterostructured magnetic nanoparticles: their versatility and high performance capabilities.* Chem Commun (Camb), 2007(12): p. 1203-14.
2. Siedlecka, E.M. and P. Stepnowski, *The effect of alkyl chain length on the degradation of alkylimidazolium- and pyridinium-type ionic liquids in a Fenton-like system.* Environ Sci Pollut Res Int, 2009. **16**(4): p. 453-8.
3. Kamaly, N., et al., *Targeted polymeric therapeutic nanoparticles: design, development and clinical translation.* Chemical Society Reviews, 2012. **41**(7): p. 2971-3010.
4. Farokhzad, O.C. and R. Langer, *Impact of nanotechnology on drug delivery.* ACS nano, 2009. **3**(1): p. 16-20.
5. Olivier, J.-C., et al., *Synthesis of pegylated immunonanoparticles.* Pharmaceutical research, 2002. **19**(8): p. 1137-1143.
6. Tadić, M., et al., *Highly crystalline superparamagnetic iron oxide nanoparticles (SPION) in a silica matrix.* Journal of Alloys and Compounds, 2012. **525**: p. 28-33.
7. Moghimi, S.M., A.C. Hunter, and J.C. Murray, *Long-circulating and target-specific nanoparticles: theory to practice.* Pharmacological reviews, 2001. **53**(2): p. 283-318.
8. Vankoningsloo, S., et al., *Cytotoxicity of multi-walled carbon nanotubes in three skin cellular models: effects of sonication, dispersive agents and corneous layer of reconstructed epidermis.* Nanotoxicology, 2010. **4**(1): p. 84-97.
9. Veiseh, O., J.W. Gunn, and M. Zhang, *Design and fabrication of magnetic nanoparticles for targeted drug delivery and imaging.* Advanced Drug Delivery Reviews, 2010. **62**(3): p. 284-304.
10. Qiang, Y., et al., *Iron/iron oxide core-shell nanoclusters for biomedical applications.* Journal of Nanoparticle Research, 2006. **8**(3-4): p. 489-496.
11. Longmire, M., P.L. Choyke, and H. Kobayashi, *Clearance properties of nano-sized particles and molecules as imaging agents: considerations and caveats.* 2008.
12. Zhang, L., et al., *Imaging and cell targeting characteristics of magnetic nanoparticles modified by a functionalizable zwitterionic polymer with adhesive 3, 4-dihydroxyphenyl-l-alanine linkages.* Biomaterials, 2010. **31**(25): p. 6582-6588.
13. Ochekpe, N.A., P.O. Olorunfemi, and N.C. Ngwuluka, *Nanotechnology and drug delivery part 2: nanostructures for drug delivery.* Tropical Journal of Pharmaceutical Research, 2009. **8**(3).
14. Manmode, A.S., D.M. Sakarkar, and N.M. Mahajan, *Nanoparticles-tremendous therapeutic potential: a review.* International Journal of PharmTech Research, 2009. **1**(4): p. 1020-1027.
15. Hu, Y., et al., *Effect of PEG conformation and particle size on the cellular uptake efficiency of nanoparticles with the HepG2 cells.* Journal of Controlled Release, 2007. **118**(1): p. 7-17.
16. Xiao, K., et al., *The effect of surface charge on< i> in vivo</i> biodistribution of PEG-oligocholic acid based micellar nanoparticles.* Biomaterials, 2011. **32**(13): p. 3435-3446.
17. Shapiro, E.M., S. Skrtic, and A.P. Koretsky, *Sizing it up: Cellular MRI using micron ‐ sized iron oxide particles.* Magnetic Resonance in Medicine, 2005. **53**(2): p. 329-338.

18. Levy, M., et al., *Long term in vivo biotransformation of iron oxide nanoparticles.* Biomaterials, 2011. **32**(16): p. 3988-3999.
19. RADISKY, D. and J. KAPLAN, *Iron in cytosolic ferritin can be recycled through lysosomal degradation in human fibroblasts.* Biochem. J, 1998. **336**: p. 201-205.
20. Song, Y., et al., *Synthesis of Well‐Dispersed Aqueous‐Phase Magnetite Nanoparticles and Their Metabolism as an MRI Contrast Agent for the Reticuloendothelial System.* European Journal of Inorganic Chemistry, 2011. **2011**(22): p. 3303-3313.
21. Xu, C., et al., *Au-Fe3O4 dumbbell nanoparticles as dual-functional probes.* Angew Chem Int Ed Engl, 2008. **47**(1): p. 173-6.
22. De Jaeghere, F., et al., *Formulation and lyoprotection of poly (lactic acid-co-ethylene oxide) nanoparticles: influence on physical stability and in vitro cell uptake.* Pharmaceutical research, 1999. **16**(6): p. 859-866.
23. Jain, T.K., et al., *Magnetic nanoparticles with dual functional properties: drug delivery and magnetic resonance imaging.* Biomaterials, 2008. **29**(29): p. 4012-4021.
24. Mikhaylov, G., et al., *Ferri-liposomes as an MRI-visible drug-delivery system for targeting tumours and their microenvironment.* Nat Nano, 2011. **6**(9): p. 594-602.
25. Ross, J.F., P.K. Chaudhuri, and M. Ratnam, *Differential regulation of folate receptor isoforms in normal and malignant tissues in vivo and in established cell lines. Physiologic and clinical implications.* Cancer, 1994. **73**(9): p. 2432-43.
26. Schladt, T.D., et al., *Synthesis and bio-functionalization of magnetic nanoparticles for medical diagnosis and treatment.* Dalton Transactions, 2011. **40**(24): p. 6315-6343.
27. Olson, E.S., et al., *Activatable cell penetrating peptides linked to nanoparticles as dual probes for in vivo fluorescence and MR imaging of proteases.* Proc Natl Acad Sci U S A, 2010. **107**(9): p. 4311-6.
28. Lee, E.S., Z. Gao, and Y.H. Bae, *Recent progress in tumor pH targeting nanotechnology.* J Control Release, 2008. **132**(3): p. 164-70.
29. Xu, C. and S. Sun, *Superparamagnetic nanoparticles as targeted probes for diagnostic and therapeutic applications.* Dalton Transactions, 2009(29): p. 5583-5591.
30. Ho, D.N., et al., *Penetration of endothelial cell coated multicellular tumor spheroids by iron oxide nanoparticles.* 2012.
31. Wang, Y.-X.J., S.M. Hussain, and G.P. Krestin, *Superparamagnetic iron oxide contrast agents: physicochemical characteristics and applications in MR imaging.* European radiology, 2001. **11**(11): p. 2319-2331.
32. Lee, J.-H., et al., *Artificially engineered magnetic nanoparticles for ultra-sensitive molecular imaging.* nature medicine, 2007. **13**(1): p. 95-99.
33. He, X., et al., *pH-sensitive drug-delivery systems for tumor targeting.* Ther Deliv, 2013. **4**(12): p. 1499-510.
34. Budker, V., et al., *pH-sensitive, cationic liposomes: a new synthetic virus-like vector.* Nat Biotechnol, 1996. **14**(6): p. 760-4.
35. Chen, D., et al., *In vivo evaluation of novel pH-sensitive mPEG-Hz-Chol conjugate in liposomes: pharmacokinetics, tissue distribution, efficacy assessment.* Artif Cells Blood Substit Immobil Biotechnol, 2010. **38**(3): p. 136-42.
36. Han, L., et al., *Acid Active Receptor-Specific Peptide Ligand for In Vivo Tumor-Targeted Delivery.* Small, 2013.
37. Zhang, S., K. Wu, and A.D. Sherry, *A Novel pH-Sensitive MRI Contrast Agent.* Angew Chem Int Ed Engl, 1999. **38**(21): p. 3192-3194.
38. Andreev, O.A., et al., *Mechanism and uses of a membrane peptide that targets tumors and other acidic tissues in vivo.* Proc Natl Acad Sci U S A, 2007. **104**(19): p. 7893-8.

39. Yao, L., et al., *pHLIP(R)-mediated delivery of PEGylated liposomes to cancer cells.* J Control Release, 2013. **167**(3): p. 228-237.
40. Yao, L., et al., *pHLIP peptide targets nanogold particles to tumors.* Proc Natl Acad Sci U S A, 2013. **110**(2): p. 465-70.
41. Wijesinghe, D., et al., *pH dependent transfer of nano-pores into membrane of cancer cells to induce apoptosis.* Sci Rep, 2013. **3**: p. 3560.
42. Moshnikova, A., et al., *Antiproliferative effect of pHLIP-amanitin.* Biochemistry, 2013. **52**(7): p. 1171-8.
43. Daumar, P., et al., *Efficient (18)F-Labeling of Large 37-Amino-Acid pHLIP Peptide Analogues and Their Biological Evaluation.* Bioconjug Chem, 2012. **23**(8): p. 1557-66.
44. Reshetnyak, Y.K., et al., *Measuring tumor aggressiveness and targeting metastatic lesions with fluorescent pHLIP.* Mol Imaging Biol, 2011. **13**(6): p. 1146-56.
45. Vavere, A.L., et al., *A novel technology for the imaging of acidic prostate tumors by positron emission tomography.* Cancer Res, 2009. **69**(10): p. 4510-6.
46. Macholl, S., et al., *In vivo pH imaging with (99m)Tc-pHLIP.* Mol Imaging Biol, 2012. **14**(6): p. 725-34.
47. Derksen, J.T., J.D. Baldeschwieler, and G.L. Scherphof, *In vivo stability of ester- and ether-linked phospholipid-containing liposomes as measured by perturbed angular correlation spectroscopy.* Proc Natl Acad Sci U S A, 1988. **85**(24): p. 9768-72.
48. Petros, R.A. and J.M. DeSimone, *Strategies in the design of nanoparticles for therapeutic applications.* Nat Rev Drug Discov, 2010. **9**(8): p. 615-27.
49. Pradhan, P., et al., *Preparation and characterization of manganese ferrite-based magnetic liposomes for hyperthermia treatment of cancer.* Journal of Magnetism and Magnetic Materials, 2007. **311**(1): p. 208-215.
50. Zhang, J., et al., *Design of nanoparticles as drug carriers for cancer therapy.* Cancer Genomics-Proteomics, 2006. **3**(3-4): p. 147-157.
51. Hamley, I.W., *Nanotechnology with Soft Materials.* Angewandte Chemie International Edition, 2003. **42**(15): p. 1692-1712.
52. Li, S.-D. and L. Huang, *Stealth nanoparticles: high density but sheddable PEG is a key for tumor targeting.* Journal of controlled release: official journal of the Controlled Release Society, 2010. **145**(3): p. 178.
53. Huang, G., et al., *Superparamagnetic iron oxide nanoparticles: amplifying ROS stress to improve anticancer drug efficacy.* Theranostics, 2013. **3**(2): p. 116-26.
54. Liu, G., et al., *Applications and Potential Toxicity of Magnetic Iron Oxide Nanoparticles.* Small, 2013. **9**(9-10): p. 1533-1545.
55. Zhang, S., et al., *Halide ion-mediated growth of single crystalline Fe nanoparticles.* Nanoscale, 2014.
56. Lacroix, L.-M., et al., *Stable single-crystalline body centered cubic Fe nanoparticles.* Nano Letters, 2011. **11**(4): p. 1641-1645.
57. Xie, J., S. Lee, and X. Chen, *Nanoparticle-based theranostic agents.* Adv Drug Deliv Rev. **62**(11): p. 1064-79.
58. Xie, J., et al., *Surface-engineered magnetic nanoparticle platforms for cancer imaging and therapy.* Acc Chem Res. **44**(10): p. 883-92.
59. Akhter, S., et al., *Gold nanoparticles in theranostic oncology: current state-of-the-art.* Expert Opin Drug Deliv. **9**(10): p. 1225-43.
60. Xie, J., S. Lee, and X.Y. Chen, *Nanoparticle-based theranostic agents.* Advanced Drug Delivery Reviews, 2010. **62**(11): p. 1064-1079.

61. C. Wang, H.D., S. Sun, *Dumbbell-like Pt-Fe3O4 Nanoparticles and Their Enhanced Catalysis for Oxygen*

Reduction Reaction. Nano Letter, 2009. **9**: p. 1493.
62. Groom, M.L.a.A., *pH environmental of red cells in the spleen* American Journal of Physiology, 1976. **231**: p. 1672.
63. Xiaoqiang Yang, J.J.G., Srikanth Pilla, Douglas A Steeber, Shaoqin Gong and Xintao Shuai, *Multifunctional polymeric vesicles for targeted drug delivery and imaging.* Biofabrication, 2010. **2**: p. 025004.
64. Pagani, A., et al., *Low hepcidin accounts for the proinflammatory status associated with iron deficiency.* Blood, 2011. **118**(3): p. 736-746.
65. Xu, C., B. Wang, and S. Sun, *Dumbbell-like Au-Fe(3)O(4) Nanoparticles for Target-Specific Platin Delivery.* J Am Chem Soc, 2009. **131**(12): p. 4216-7.
66. Howe, L.R. and P.H. Brown, *Targeting the HER/EGFR/ErbB family to prevent breast cancer.* Cancer Prev Res (Phila). **4**(8): p. 1149-57.
67. Deu, E., et al., *Ferrous iron-dependent drug delivery enables controlled and selective release of therapeutic agents in vivo.* Proceedings of the National Academy of Sciences, 2013. **110**(45): p. 18244-18249.
68. Kievit, F.M., et al., *Doxorubicin loaded iron oxide nanoparticles overcome multidrug resistance in cancer in vitro.* Journal of Controlled Release, 2011. **152**(1): p. 76-83.
69. Geng, Y., et al., *Three to Tango: MUC1 as a ligand for both E-selectin and ICAM-1 in the breast cancer metastatic cascade.* Frontiers in Oncology, 2012. **2**.
70. Al-Jamal, W.T. and K. Kostarelos, *Liposomes: from a clinically established drug delivery system to a nanoparticle platform for theranostic nanomedicine.* Accounts of Chemical Research, 2011. **44**(10): p. 1094-1104.
71. Xie, J., S. Lee, and X. Chen, *Nanoparticle-based theranostic agents.* Advanced Drug Delivery Reviews, 2010. **62**(11): p. 1064-1079.
72. Maenosono, S. and S. Saita, *Theoretical assessment of FePt nanoparticles as heating elements for magnetic hyperthermia.* Magnetics, IEEE Transactions on, 2006. **42**(6): p. 1638-1642.
73. Xu, C., et al., *FePt nanoparticles as an Fe reservoir for controlled Fe release and tumor inhibition.* Journal of the American Chemical Society, 2009. **131**(42): p. 15346-15351.
74. Valko, M., et al., *Free radicals, metals and antioxidants in oxidative stress-induced cancer.* Chemico-Biological Interactions, 2006. **160**(1): p. 1-40.
75. Chiang, I.C. and D.H. Chen, *Synthesis of Monodisperse FeAu Nanoparticles with Tunable Magnetic and Optical Properties.* Advanced Functional Materials, 2007. **17**(8): p. 1311-1316.
76. Negishi, Y. and T. Tsukuda, *Visible photoluminescence from nearly monodispersed Au12 clusters protected by meso-2,3-dimercaptosuccinic acid.* Chemical Physics Letters, 2004. **383**(1–2): p. 161-165.
77. Jain, P.K., et al., *Noble metals on the nanoscale: optical and photothermal properties and some applications in imaging, sensing, biology, and medicine.* Accounts of Chemical Research, 2008. **41**(12): p. 1578-1586.
78. Jain, P.K., et al., *Calculated absorption and scattering properties of gold nanoparticles of different size, shape, and composition: applications in biological imaging and biomedicine.* The Journal of Physical Chemistry B, 2006. **110**(14): p. 7238-7248.
79. Shen, W.F.S., B. D.; Carter, M. J.; Xie, J.; Xu, C. J.; Sun, S. H.; Xiao, G, J. Appl. Phys. 2008, 103,

07A306-, 2008. **103**: p. 07A306.
80. Shen Weifeng Shen, et al., *Quantitative detection of DNA labeled with magnetic nanoparticles*

using arrays of MgO-based magnetic tunnel junction sensors. APPLIED PHYSICS LETTERS, 2008

93: p. 033903.
81. Prins, M.M.a.M., *Magnetic biochips: a new option for sensitive diagnostics.* Journal of Magnetism and Magnetic Materials, 2005. **293**: p. 702.
82. Hall, D.A., et al. *Portable biomarker detection with magnetic nanotags*. in *Circuits and Systems (ISCAS), Proceedings of 2010 IEEE International Symposium on*. 2010. IEEE.
83. Jing, Y., et al. *High-magnetic-moment nanoparticles for biomedicine*. in *Engineering in Medicine and Biology Society, 2009. EMBC 2009. Annual International Conference of the IEEE*. 2009. IEEE.
84. Gaster, R.S., et al., *Matrix-insensitive protein assays push the limits of biosensors in medicine.* nature medicine, 2009. **15**(11): p. 1327-1332.
85. Gaster, R.S., et al., *Quantification of protein interactions and solution transport using high-density GMR sensor arrays.* Nature nanotechnology, 2011. **6**(5): p. 314-320.
86. Sun, X., et al., *Novel application of magnetoresistive sensors for high-voltage transmission-line monitoring.* Magnetics, IEEE Transactions on, 2011. **47**(10): p. 2608-2611.
87. Sun, X., et al., *Magnetic nanoparticles for magnetoresistance-based biodetection.* NanoBioscience, IEEE Transactions on, 2012. **11**(1): p. 46-53.
88. Y. Hou, Z.X., S. Sun, *Controlled synthesis and chemical conversions of FeO nanoparticles.* Angew. Chem. Int. Ed, 2007. **46**: p. 6329.
89. S. Peng, C.W., J. Xie, S. Sun, J. Am. Chem. Soc., 2006. **128**: p. 10676.
90. Baughman, T.A., *Elemental mercury spills.* Environmental health perspectives, 2006. **114**(2): p. 147.
91. Bidstrup, P.L., *Toxicity of Mercury and its Compounds.* Toxicity of Mercury and its Compounds., 1964.
92. Clevenger, W., B. Smith, and J. Winefordner, *Trace determination of mercury: a review.* Critical reviews in analytical Chemistry, 1997. **27**(1): p. 1-26.
93. Lee, J.S., M.S. Han, and C.A. Mirkin, *Colorimetric detection of mercuric ion (Hg2+) in aqueous media using DNA-functionalized gold nanoparticles.* Angewandte Chemie-International Edition, 2007. **46**(22): p. 4093-4096.
94. Lee, J.S. and C.A. Mirkin, *Chip-based scanometric detection of mercuric ion using DNA-functionalized gold nanoparticles.* Analytical Chemistry, 2008. **80**(17): p. 6805-6808.
95. Desvaux, C., et al., *Multimillimetre-large superlattices of air-stable iron-cobalt nanoparticles.* Nature Materials, 2005. **4**(10): p. 750-753.
96. Lee, J.S.M., C. A. , Anal. Chem., 2008. **80**: p. 6805.
97. Zhang, W., et al., *Protein kinase D specifically mediates apoptosis signal-regulating kinase 1-JNK signaling induced by H2O2 but not tumor necrosis factor.* Journal of Biological Chemistry, 2005. **280**(19): p. 19036-19044.
98. DiMauro, S. and E.A. Schon, *Mitochondrial disorders in the nervous system.* Annu. Rev. Neurosci., 2008. **31**: p. 91-123.
99. Guo, C., et al., *Room temperature ionic liquid doped DNA network immobilized horseradish peroxidase biosensor for amperometric determination of hydrogen peroxide.* Analytical and bioanalytical chemistry, 2007. **389**(2): p. 527-532.

100. Yin, J., et al., *A hydrogen peroxide electrochemical sensor based on silver nanoparticles decorated silicon nanowire arrays.* Electrochimica Acta, 2011. **56**(11): p. 3884-3889.
101. Meng, F., et al., *Nanoporous gold as non-enzymatic sensor for hydrogen peroxide.* Electrochimica Acta, 2011. **56**(12): p. 4657-4662.
102. Chen, W., et al., *Recent advances in electrochemical sensing for hydrogen peroxide: a review.* Analyst, 2012. **137**(1): p. 49-58.
103. Kimmel, D.W., et al., *Electrochemical sensors and biosensors.* Analytical Chemistry, 2011. **84**(2): p. 685-707.
104. Sun, X., et al., *Dumbbell-like PtPd–Fe3O4 nanoparticles for enhanced electrochemical detection of H2O2.* Nano Letters, 2012. **12**(9): p. 4859-4863.
105. Lin, Y., et al., *Platinum/carbon nanotube nanocomposite synthesized in supercritical fluid as electrocatalysts for low-temperature fuel cells.* The Journal of Physical Chemistry B, 2005. **109**(30): p. 14410-14415.
106. Ansari, A.A., et al., *Nanostructured metal oxides based enzymatic electrochemical biosensors.* 2010.
107. Chen, Z., et al., *Optical detection of choline and acetylcholine based on H< sub> 2</sub> O< sub> 2</sub>-sensitive quantum dots.* Biosensors and Bioelectronics, 2011. **28**(1): p. 50-55.
108. Bai, Y.-H., et al., *Relationship between nanostructure and electrochemical/biosensing properties of MnO2 nanomaterials for H2O2/choline.* The Journal of Physical Chemistry C, 2008. **112**(48): p. 18984-18990.